Department of Nanophysics, Istituto Italiano di Tecnologia, Genova, Italy

DIFI, Università degli studi di Genova, Genova, Italy

A thesis submitted for the degree of

Doctor of Philosophy

NANOSCALE INVESTIGATION OF NUCLEAR STRUCTURES BY TIME-RESOLVED MICROSCOPY

Simone Pelicci

Ph.D. supervisors:

Dr. Luca Lanzanò

Prof. Alberto Diaspro

Ph.D. course in Physics

XXXII Cycle

…to my grandparents Piero and Silvia,

my guides…

Acknowledgements

I would like to thank all the people who have contributed to the realization of this thesis and supported me during my work.

Firstly, I would like to thank a lot Alberto, who gave me the opportunity to be part of his research team, making me aware of the intriguing world of advanced microscopy. It seems to me a day has passed since you told me to come into your office to talk to me about my new Ph.D. student adventure … and what an adventure! Thank you for this precious opportunity, which has been worth a three-year experience that I will always carry with me.

A special thanks goes to Luca, my mentor and friend, who has followed me step by step during these three years. There are no words to describe how crucial he was to me. I will remember with a smile the countless hours spent together in the laboratory and at your desk. I'm gonna miss coming to your office just to ask you for coffee. Thank you for everything you've taught me and for preparing me best for my future.

I would like to thank friends and colleagues with whom I have shared joys and sorrows on this long journey. Thanks for the moments of moral support and for the laughter. I will always carry with me unforgettable moments spent together.

Moreover, I would like to thank my girlfriend Giorgia. Thanks to her and her continuous support, I was able to overcome the most difficult moments. She has always been by my side in every situation and I am sure that with her close to me no goal will be impossible to reach.

Finally, I would like to thank my family. In particular, my father Giuliano, my mother Simonetta and my sister Elena, who have always supported me and have always believed in me. Thanks for the valuable advice.

Contents

Chapter 3

Chapter 4

Abstract

The eukaryotic cell nucleus is composed by heterogeneous biological structures, such as the nuclear envelope (NE) and chromatin. At a morphological level, chromatin organization and its interactions with nuclear structures, such as nuclear lamina (NL) and nuclear pore complex (NPC), are suggested to play an essential role in the regulation of gene activity, which involves the packaging of the genome into transcriptionally active and inactive sites, bound to healthy cell proliferation and maintenance. However, the processes governing the relation between nuclear structures and gene regulation are still unclear. For this reason, the advanced microscopy methods represent a powerful tool for imaging nuclear structures at the nanometer level, which is essential to understand the effect of nuclear interactions on genome function. The nanometer information may be achieved either through the advanced imaging techniques in combination with fluorescence spectroscopy or with the help of super-resolution methods, increasing the spatial resolution of the conventional optical microscopy. In this thesis, I implemented a double strategy based on a novel FLIM-FRET assay and super resolution SPLIT-STED method for the investigation of the chromatin organization and nuclear envelope components (lamins and NPC) at the nanoscale, in combination with the phasor analysis. The phasor approach can be applied to several fluorescence microscopy techniques abled to provide an image with an additional information in a third channel. Phasor plot is a graphical representation, which decodes the fluorescence dynamics encoded in the image, revealing a powerful tool for the data analysis in time-resolved imaging.

The **Chapter 1** of the thesis is characterized by an **Introduction,** which provides an overview on the chromatin organization at the nanoscale and the description of the several advanced fluorescence microscopy techniques used for its investigation. They are broadly divided into two main categories: the advanced imaging techniques, such as Fluorescence Correlation Spectroscopy (FCS), single particle tracking (SPT) and Fluorescence Recovery After Photobleaching (FRAP), Forster Resonance Energy Transfer (FRET) and

Fluorescence Lifetime Imaging Microscopy (FLIM) and the super-resolution techniques, which include Stimulated Emission Depletion (STED), Structured Illumination Microscopy (SIM) and single molecule localization microscopy (SMLM). Following, **Chapter 2** focus on the capabilities of the phasor approach in time-resolved microscopy, as a powerful tool for the analysis of the experimental data. After a description of the principles of time-domain and frequency-domain measurements, in this section are explained the rules of the phasor analysis and its applications in different fluorescence microscopy techniques. In **Chapter 3**, I present a FRET assay, based on the staining of the nuclei with two DNA-binding dyes (e.g. Hoechst 33342 and Syto Green 13) by using frequency-domain detection of FLIM and the phasor analysis in live interphase nuclei. I show that the FRET level strongly depends on the relative concentration of the two fluorophores. I describe a method to correct the values of FRET efficiency and demonstrate that, with this correction, the FLIM-FRET assay can be used to quantify variations of nanoscale chromatin compaction in live cells. In **Chapter 4**, the phasor analysis is employed to the improvement of the resolving power of the super-resolution STED microscopy. I describe a novel method to investigate nuclear structures at the nanometer level, known as SPLIT (Separation of Photons by Lifetime Tuning), developed by my group in last years. By using the phasor approach, the SPLIT technique decodes the variations of spectroscopic parameters of fluorophores, such as lifetime and fluorescence intensity, due to the effect of the modulated depletion power of the STED technique, increasing the resolving power. In this chapter, I develop the concept of the SPLIT method modulating the excitation pattern during the image acquisition to overcome its limitation linked to the photobleaching effect and the signal-to-noise ratio.

Chapter 1

1. Introduction

1.1 An open question: chromatin nanoscale organization

Chromatin nanoscale architecture in eukaryotic nucleus is organized in different higher-order structures, from the nucleosome to the chromosome territories. The nucleosome can be considered the smallest organization unit of chromatin. Structurally, the nucleosome is composed by the core histone proteins H2A, H2B, H3 and H4 with ~145–147 base-pair long DNA wrapped around the histone octamer complex, whereas histone H1 is directly involved in the modulation of chromatin compaction. The H1 histone interacts with a short DNA segment, termed DNA linker, which connects the single nucleosomes into a nucleosomal array. This nucleosomal array is generally defined as the "bead-on-a-string" organization and corresponds to the primary structure of chromatin. The nucleosome structure and dynamics may be affected by the post-translational modifications (PMTs), such as acetylation, methylation, phosphorylation, ubiquitylation and sumoylation. PMTs are enzymatic modification of histone amino acids side chains with an important function in chromatin remodeling and regulation of many genomic processes. Chromatin modification is affected also by other protein families,

implicated in the variations of the components of the nucleosome such as architectural chromatin proteins (ACPs) and ATP-dependent chromatin remodelers [1][2][3].

The single nucleosomal arrays are folded into three-dimensional (3D) chromatin structures, characterized by different degree of compaction. The first step towards the formation of 3D chromatin configuration is the folding of an individual array (the primary structure) into secondary chromatin structures such as the fiber of 30nm [4][3]. Subsequent intermolecular interactions between secondary chromatin structures produce large-scale configurations, corresponding to tertiary structures, in which DNA is more compacted into metaphase nuclear chromosomes. During interphase, chromosomes are organized as chromosome territories, defined as the nuclear space occupied by the DNA of a given chromosome [5][6]. Out of mitotic process, chromatin can be generally divided in two categories, depending on different compaction states: heterochromatin and euchromatin. Heterochromatin was first defined as the condensed chromatin representing gene-poor stretches of the genome, while euchromatin has been described as decompacted chromatin, which includes gene-rich regions. Heterochromatin can be further separated in constitutive and facultative heterochromatin. Constitutive heterochromatin contains hypoacetylated nucleosomes enriched in histone H3 methylated at lysine 9 (meH3K9). MeH3K9 is bound by the heterochromatin protein 1 (HP1), which is a typical component of heterochromatin. HP1 contributes to the propagation and maintenance of heterochromatin and it recruits a variety of binding nuclear proteins, interacting with other nuclear structures [7][8][9][10]. Whereas methylation of H3K9 is typically found at constitutive heterochromatin, methylation of H3K27 is often associated with facultative heterochromatin. Facultative heterochromatin corresponds to transcriptionally silent chromatin regions, which decondense and allow transcription within temporal (e.g. developmental states or specific cell-cycle stages) and spatial (e.g. nuclear localization changes from the center to the periphery or vice versa) windows [11]. In mammalian nuclei, the heterochromatin regions include the nuclear periphery (with exclusion of the areas occupied by

nuclear pores) and the nucleolar peripheries [12][13]. It is well known that the gene expression is dependent on morphologically modulation of chromatin architecture, which regulates many cellular processes such as replication, transcription and DNA damage repair (DDR) of many genomic sequences along the double-helix of DNA. Many studies have correlated transcriptional activity or repression of a genomic sequence with different chromatin regions. Transcriptionally silent chromatin in differentiated mammalian cells clusters are generally positioned around the nucleolus and the nuclear periphery, whereas transcriptionally active chromatin is found in an internal nuclear location [14]. Epigenetic modifications in euchromatin and heterochromatin can be associated with active transcription or gene silencing. During the promoting of active transcription, the chromatin remodeling corresponds to a transient unwrapping of the end DNA from histone octamers, forming the DNA loop, or moving nucleosomes to different translational positions, all of which change the accessibility of histone DNA to transcription factors (TFs) [15]. During the replication process, chromatin participates dynamically by removing nucleosomes ahead of advancing replication fork and be recruited behind it, allowing the progress of the formation of the native dsDNA filament [16][17]. Besides, as showed in many works, DNA damage repair (DDR) processes and chromatin modulation are tightly linked, affecting the genome stability. Broadly, the DDR repair machinery must be able to: (i) find DNA damage in different chromatin structures; (ii) reorganize the nucleosome-DNA template for facilitate entrance to the damage sites; (iii) reorganize the local chromatin architecture to provide access to the repair machinery; (iv) restore the local chromatin organization after repair of single and double strand breaks. Maintaining the integrity of genetic information is critical for both normal cellular functions and for suppressing mutagenic events that can lead to pathological diseases, as cancer.

In summary, defects in how chromatin is globally organized are relevant for physiological and pathological processes. In last decades, improvements in the methods for visualization of chromatin structure at the nanoscale have

been fundamental to better understand the link between chromatin modulation and genome expression [18][19][20].

Electron microscopy (EM) was the first technique in the imaging research field available to achieve nanoscale information concerning the spatial organization of nucleosomes. EM may image chromatin down to the level of single nucleosome (11 nm) and map the 3D chromatin structure. During last decades, one of the main models of secondary chromatin structure, the 30-nm chromatin fiber, has remained controversial. In recent years, EM and cryogenic electron microscopy (cryo-EM) were applied to produce the structure of 30-nm chromatin fibers from *in vitro* reconstituted nucleosome arrays containing the linker histone H1 and with different nucleosome repeat lengths, to define fiber dimensions [21][22]. Recently, Ou et al. overcame the limitation of conventional EM stains, such as osmium tetroxide, uranium acetate and lead salts and developed a DNA-labeling method, called ChromEM. It was reported a new approach which utilizes ChromEM, together with multi-axis transmission electron microscopy (TEM) tomography, for chromatin 3D organization with a nominal resolution of 1.6 nm. Ou et al. demonstrated that chromatin is a disordered 5 to 24 nm in diameter polymer chain, rather than the classically considered hierarchically folded assembly [23]. However, despite the achievement of a very high resolution, these methods are invasive, lack molecular specificity and are not applicable in living cells. The main reason is the sample preparation procedure. The conventional EM-sample preparation is to fix and dehydrate the sample, embed it in a plastic medium, cut sections thin enough to allow transmission of the electron beam, and then stain or coat the material with heavy metals or metal salts, as described above. These preparative treatments are disruptive for most biological samples, introduce uncertainties concerning the degree to which the final images reflect the original hydrated structures. Notably, cryo-EM is applied to frozen-hydrated samples for their preservation [24][25].

Optical microscopy can overcome most of these limitations. It allows non-invasive visualization of cellular structures, such as chromatin, in 3D and in live cells. The use of fluorescent molecules to label biological targets provides

high contrast and high specificity. Unfortunately, the Abbe's diffraction law limits the investigation of biological targets smaller than 200nm, restricting the resolution capability of the conventional confocal microscope [26]. However, the recent advent of super-resolution fluorescence microscopy (SRM) techniques has extended the ultimate resolving power of optical microscopy beyond the diffraction limit, facilitating access to the organization of chromatin at the nanoscale, achieving a spatial resolution smaller than 50nm [27]. The SRM techniques include stimulated emission depletion (STED) microscopy [28], structured illumination microscopy (SIM) [29], and localization microscopy, such as photo-activated localization microscopy (PALM) [30] and stochastic optical reconstruction microscopy (STORM) [31][32]. Moreover, thanks to the molecular specificity of fluorescence microscopy, it is possible to obtain information about nanoscale chromatin organization without the help of super-resolution. A winning strategy is based on the combination of imaging with fluorescence spectroscopy techniques, thanks to which it is possible to obtain information at the nanoscale bypassing the diffraction limit. Many works were published in last years that showed important results about the chromatin nanoscale organization by using advanced fluorescence microscopy techniques such as fluorescence recovery after photobleaching (FRAP), fluorescence correlation spectroscopy (FCS) and fluorescence lifetime imaging (FLIM) microscopy [33][34][35][36].

1.2 Advanced fluorescence microscopy techniques

The development of advanced fluorescence microscopy techniques has been important to the study of chromatin organization and dynamics. The combination of fluorescence imaging with fluorescence spectroscopy allowed the indirect exploration of chromatin architecture around a fluorescence target probe. In general, the variations of the spectroscopy properties of a specific fluorophore can provide information about the surrounding microenvironment. For instance, the impact that the chromatin landscape

has to the mobility of molecules, may be explored by measuring the molecular diffusion of a fluorescent probe through methods as Fluorescence Correlation Spectroscopy (FCS), single particle tracking (SPT) and Fluorescence Recovery After Photobleaching (FRAP). Similarly, the chromatin architecture can be studied by measuring the variation of spectroscopy parameters, such as fluorescence intensity and fluorescence lifetime of a fluorophore, through Forster Resonance Energy Transfer (FRET) and Fluorescence Lifetime Imaging Microscopy (FLIM).

1.2.1 Fluorescence Correlation Spectroscopy (FCS)

Fluorescence Correlation Spectroscopy (FCS) was introduced in the early 1970s to quantify the local mobility of drug intercalation into double-stranded DNA. In FCS, the measured parameter is the fluctuation of the fluorescence intensity, which looks like noise and occurs from chemical, biological, and physical effects on the fluorophore of interest. These fluctuations, during the correlation measurement in the observed volume, reveal information about the environment in which a fluorophore resides. The FCS analysis is traditionally performed using correlation functions. In a fluctuation record, there are two aspects to consider. One is the temporal spectrum of the fluctuation, which is obtained using the autocorrelation function (ACF) approach, and the other is the analysis of the amplitude spectrum, which is obtained using the photon-counting histogram approach or fluctuation intensity distribution analysis. The intensity fluctuation at time t is calculated as $\delta F(t) = F(t) - \langle F(t) \rangle$ where F(t) is the fluorescence intensity at time t and $\langle F(t) \rangle$ represents the average value of the fluorescence intensity. The intensity fluctuation parameter $\delta F(t)$ is used to calculate an autocorrelation curve, which is defined as:

$$G(\tau) = \frac{\langle \delta F(t) \cdot \delta F(t+\tau) \rangle}{\langle F(t) \rangle^2} = \frac{\langle F(t) \cdot F(t+\tau) \rangle}{\langle F(t) \rangle^2} - 1 \qquad (1.1)$$

The resultant autocorrelation signal, G(τ), quantifies the self-similarity of the fluorescence signal at different time lags. The ACF is used to extract the characteristic relaxation times associated to the system under study. For instance, when diffusion of a fluorescent probe is observed by FCS in a confocal setup, the characteristic relaxation time is due to fluorophore diffusing in and out of the focal volume. By fitting the curve with different mathematical models, it is possible to obtain the diffusion time (τD), the number of molecules in the confocal excitation volume (<N>), the diffusion coefficient (D), or molecular brightness (η). Moreover, the correlation functions can reveal if the fluorescence fluctuations, in the observation volume, depend on a sum of multiple independent processes (such as diffusion, blinking or binding) [37][38][39][40].

In last years, FCS technique has been used extensively to study the impact of chromatin organization on molecular diffusion [37]. For instance, Di Bona et al. quantified diffusion of monomeric GFP in hetero- versus eu-chromatin. They found that GFP mobility is dependent on the different density chromatin regions, showing that it is reduced in heterochromatin, especially in perinucleolar heterochromatin. Bancaud et al. also showed that the mobility of eGFP oligomers was found to be modulated by euchromatin versus heterochromatin, demonstrating that chromatin-interacting proteins remain transiently trapped in heterochromatin due to crowding induced enhanced affinity. Moreover, FCS has been used to detect and characterize DNA-binding dynamics of biological target such as transcription factors (TFs) within nuclear compartment. Important studies investigated the diffusion of many transcription factors such as Oct4 during the mammalian development or the impact of STAT3 oligomerization on nuclear transport and DNA-binding dynamics [41][42].

1.2.2 Single particle tracking (SPT)

In last years, Single-particle tracking (SPT) was a powerful tool in fluorescence microscopy to investigate a wide range of cellular processes, as the dynamics of the molecules in the nucleus, labeled with fluorescence

probes. SPT, together with novel optical implementation, provides super-spatiotemporal resolution of single molecule dynamic events. Generally, the image analysis methods can be divided into spatial and temporal aspects. The spatial aspect is represented by the particle detection, in which fluorescence spots are identified and their coordinates estimated in every frame of the stack images, whereas the temporal aspect is given by the particle linking, in which the molecular motions are recorded during a time-lapse acquisition and the molecular positions are determined in consecutive frames. The two steps are commonly performed only once, but may also be applied iteratively. In fluorescence microscopy, an arbitrary particle appears in the detector as a diffraction pattern, known as the Airy disk, with a shape of concentric rings having decaying intensity. The diffraction pattern of single particle is often referred to as a point spread function (PSF) and its profile can be analyzed by fitting the 2D Gaussian function. By fitting a 2D Gaussian to the observed intensity profile of a particle, the centroid of individual particles may be determined with a localization precision usually 10-20x smaller than the width of the PSF. The spatial localization accuracy and precision to identify the centroid positions of fluorescence particle depends on the signal-to-noise (SNR) ratio, determined by the brightness of the utilized probe and specific instrument parameters. The single molecule-SNR is given by:

$$SNR = \frac{I_0}{\sqrt{\sigma_{bkg}^2 + \sigma_{I_0}^2}} \tag{1.2}$$

where I_0 corresponds to the intensity signal on the peak of the PSF, $\sigma_{I_0}^2$ is the variance of peak-intensity signal above the background and σ_{bkg}^2 is the variance of the background [43]. By time-lapse acquisition of stack images, the centroid positions of each single particle can be recorded to generate trajectories that describe the motion of each individual particle as a function of time. Different algorithms have been developed for the tracking of particle dynamics under different experimental conditions, although the most widely used quantity is the mean-square-displacement (MSD) as a function of the time delay. The MSD describes the average of the square distance between

the (x,y) start position of a single particle and its end position for all time delays of a certain duration within one trajectory [44][45][46][47]. In last years, many works showed the efficiency of SPT techniques in the study of the nuclear particles and chromatin mobility in live cells [48]. SPT studies have described the motion of these labeled chromatin regions as Brownian motion and that chromatin does indeed undergo significant diffusion, as Brownian motion within the nucleus, which is consistent with a highly defined nuclear architecture [49]. For instance Chubb et al, showed that loci at nucleoli or at the nuclear periphery are significantly less mobile than other loci, suggesting an important role in maintaining the 3D organization of chromatin [50].

1.2.3 Fluorescence Recovery after Photobleaching (FRAP)

FRAP is a technique developed to study protein mobility in living cells by measuring the rate of fluorescence recovery at a previously bleached site. Briefly, an intense laser light is used to flash a region of the sample, containing molecules labelled to fluorescent probes. Fluorescent molecules are irreversibly photobleached in a small area of the cell by high intensity illumination with a focused laser beam. After the bleaching, diffusion of the surrounding non-bleached fluorescent molecules into the bleached area leads to the recovery of fluorescence, recorded at low laser power. In a FRAP experiment, two parameters may be extrapolated: the mobile fraction of fluorescent molecules and the mobility rate, quantified by the diffusion time τ_D. The mobile fraction M may be determined by comparing the fluorescence intensity in the bleached region after the full recovery (I_∞) with the initial (pre-bleach) fluorescence intensity (I_i) and the post-bleached intensity signal (I_0) as defined by the equation:

$$M = \frac{I_\infty - I_0}{I_i - I_0} \tag{1.3}$$

The mobility rate is expressed by the diffusion coefficient *D*, described by the Stoke-Einstein equation, which is related to the diffusion time τ_D, as described by the two-dimensional diffusion equation:

$$\tau_D = \frac{w^2\gamma}{4D} \tag{1.4}$$

where w^2 is defined as the radius of the focused laser beam in a circular bleached area and γ is a correction factor for the amount of bleaching. However, FRAP technique present potential limitations to biological studies due to the following reasons. The bleaching of a small area of interest affects a limited number of fluorophores and decrease the SNR. Additionally, FRAP may include the possibility of an incomplete fluorescence recovery due to obstruction of diffusion [51][52][53]. Further problem are associated to the possibility of the crosslink of the fluorophores and local increase of temperature, modifying the *D* value. Finally, as well known, the photobleaching may lead to a significant photodamage of the biological samples. Nevertheless, FRAP has been shown to be a good approach to study nuclear protein and chromatin mobility as mRNA mobility, DNA-interacting molecules and chromatin structure [54][55].

1.2.4 Förster Resonance Energy Transfer (FRET)

Molecular interactions between biological proteins have a key role in the regulation of physiological and pathological processes of living cells. In last decades, the spectroscopy phenomenon of Förster Resonance Energy Transfer (FRET) turned out a powerful tool for biomedical research, allowed the biological investigation of protein interactions at the nanometer level. The technology advancement in optical microscopy and the progress in novel fluorophores have generated important biological results in the field of FRET microscopy. A wide variety of FRET approaches have been applied, each with its own advantages and limitations. FRET provides a spatial nanoscale information about the dynamics and the distribution of proteins in a biological system without the help of super-resolution microscopy methods.

Fluorescence Resonance Energy Transfer (FRET) is a non-radiative energy transfer, which occurs from a fluorophore in the excited state, the donor molecule (D), to an acceptor molecule (A) in the ground state. The term "resonance energy transfer" refers to the fact that energy transfer occurs by means of intermolecular dipole-dipole coupling, in which vibronic transitions in the donor have practically the same energy as the corresponding transitions in the acceptor ('resonant' coupling), not involving emission and reabsorption of photons. Three physical conditions must be satisfied for the occurrence of FRET. First, the spectral overlap between the donor emission spectrum and the acceptor excitation spectrum. Second, the distance between the two fluorophore must be within 10 nanometers. FRET can be consider as a "spectroscopic nanoruler", providing nanoscale information about the proximity of labelled molecules. Third, the dipole moments of the two fluorophore must be in a favorable orientation [56]. The rate of energy transfer depends on these spectroscopy properties, and strongly depends on the sixth power of the distance between the donor and acceptor molecules:

$$k_T(r) = \frac{1}{\tau_D}\left(\frac{R_0}{r}\right)^6 \qquad (1.5)$$

where τ_D is the decay time of the donor in the absence of acceptor, R_0 is the Förster distance, and r is the donor-to-acceptor distance. Hence, the rate of transfer is equal to the decay rate of the donor $(1/\tau_D)$ when $r = R_0$, and the transfer efficiency is 50%. Forster distance is comparable to the size of macromolecules and it is reasonable to assume that energy transfer occurs whenever donors and acceptor are within the Forster distance, as a proximity indicator. R_0 can be measured from the spectral property of the donors and acceptors. It depends on the quantum yield of the donor, the extinction coefficient of the acceptor, the spectral overlap of the donors and acceptors, and the relative orientation of the fluorophores:

$$R_0 = 9.78 \times 10^3 \, [\kappa^2 \, n^{-4} \, Q_D \, J(\lambda)]^{1/6} \text{ (in Å)} \qquad (1.6)$$

where κ^2 is the orientation factor between donor and acceptor; n is the refractive index of the medium; Q_D is the quantum yield of the donor in the absence of the acceptor; $J(\lambda)$ is the degree of spectral overlap between the donor fluorescence and the acceptor excitation spectra.

The efficiency of energy transfer (E) is the fraction of photons absorbed by the donor that is transferred to the acceptor and it is given by the following equation:

$$E_{FRET} = \frac{R_0^6}{R_0^6 + r^6} \tag{1.7}$$

which is the ratio of the transfer rate to the total decay rate of the donor in the presence of acceptor. This equation shows that the transfer efficiency is strongly dependent on D-A distance. For distances less than R_0 ($r < R_0$) the FRET efficiency is close approximately near the value 1, whereas for distances greater than R_0 ($r > R_0$) the efficiency is close to 0. The FRET efficiency may also be affected by an important parameter that describes the dipole orientation of the molecules: the orientation factor k^2. Depending upon the relative orientation of donor and acceptor this factor can range from 0 to 4. When the donor and acceptor transitions dipole are in a parallel orientation $k^2 = 4$, FRET efficiency is measured, whereas in a perpendicular orientation $k^2 = 0$, the energy transfer is prevented. The value of FRET efficiency may be detected by different approaches, but two in particular are generally applied: the intensity-based and the lifetime-based detection of FRET. The intensity based detection is given by the equation:

$$E_{FRET} = 1 - \frac{F_{DA}}{F_D} \tag{1.8}$$

where the FRET efficiency is measured using the fluorescence intensity value of the donor in the absence and in presence of the acceptor. Here, the acceptor works as a quencher for the donor, so the efficiency can be measured as a decrease of the fluorescence intensity of the donor molecule.

At the same time, it is possible quantify FRET by measuring the increase of the acceptor fluorescence emission, caused by the energy transfer rate from the donor molecules. However, the value obtained must be corrected from possible contamination sources, as cross-talk and bleed-through. To avoid the problem, several methods are implemented to measure FRET, such as the "three-cube FRET", in order to extrapolate the real FRET signal by using intensity parameter ($F_{FRET} = F_{total} - F_{bleedthrough} - F_{cross\text{-}talk}$).

The transfer efficiency can also be calculated from the fluorescence lifetime parameter τ. The fluorescence lifetime is defined as the average time that the molecule spends in the excited state before to return to the ground state, in the time order of nanoseconds. In biological studies, the values of fluorescence lifetime vary between 1 and 10 ns and it is equal to the inverse of the sum of the rate constants of all the de-excitation processes of the system, including the rate constant of fluorescence emission k_R and non-radiative decay k_{NR} as described by the equation:

$$\tau = \frac{1}{k_R + k_{NR} + k_T} \tag{1.9}$$

During the FRET process, the constant of energy transfer rate from a donor to an acceptor fluorophore (k_T) increase the constant of the non-radiative decay rate of the system, producing a decrease of the donor lifetime, as clearly show the formula above.

The FRET efficiency is calculated as:

$$E_{FRET} = 1 - \frac{\tau_{DA}}{\tau_D} \tag{1.10}$$

Where τ_{DA} is the lifetime of the donor in the presence of the acceptor, while τ_D corresponds to the donor lifetime without the acceptor molecule. This formula may be translated as the ratio of the energy transfer rate and the total de-excitation processes of the system.

With respect to fluorescence intensity, lifetime of the fluorophore is mostly independent from its concentration, overcoming the limitations bound to the

intensity-based FRET detection methods, such as signal cross-contamination, the probes concentration and variations of fluorescence intensity. The perfect tool for the measurements of the lifetime variations in a biological system is Fluorescence Lifetime Imaging Microscopy (FLIM) technique[57][58][59][60][61][62][63].

In different cases, the detection of FRET can be more complex, due to different potential conditions such as: (i) artifacts caused by orientation and distance issues, (ii) cross-talk, (iii) bleed-through, (iv) ensembles of donor and acceptor molecules, (v) change of fluorescence property upon the binding of labelled molecules, (vi) Homo-FRET.

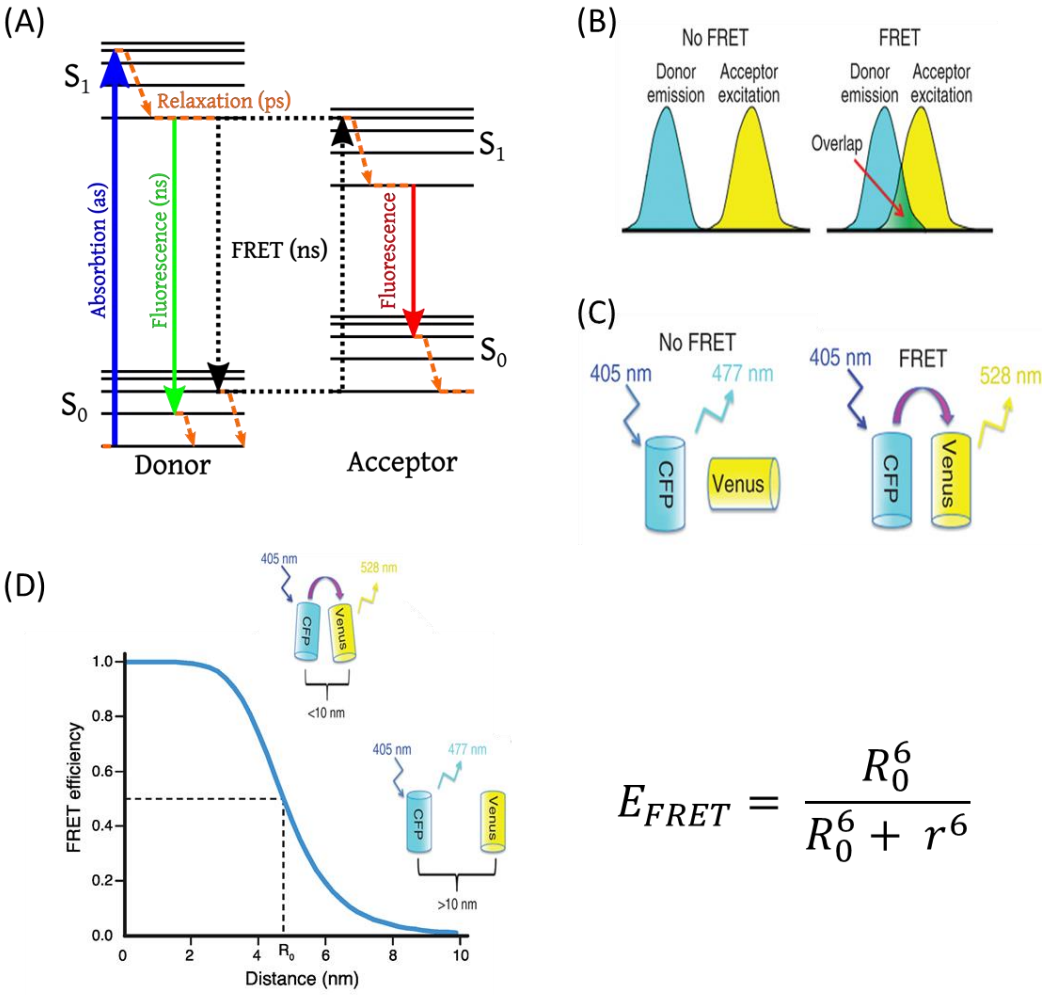

Figure 1.1. FRET principle. (A) Jablonsky diagram of the energy transfer between a donor and an acceptor molecule during the FRET process. FRET occurs if the following conditions

are satisfied: (i) the emission spectrum of the donor fluorophore must overlap with the excitation spectrum of the acceptor fluorophore **(B)**, (ii) if the donor and acceptor fluorophore dipoles have the same spatial orientation **(C)** and (iii) if the donor and acceptor fluorophores are within a distance of 10 nm. The FRET efficiency (E_{FRET}) value is dependent on the proximity of the donor and acceptor fluorophores **(D).**

1.2.5 Fluorescence Lifetime Imaging Microscopy (FLIM)

Fluorescence lifetime imaging microscopy (FLIM) is the perfect combination of lifetime spectroscopy and imaging, providing spatial lifetime maps of fixed and live samples. The fluorescence lifetime is measured at every single pixel of the image, providing a lifetime map image. The lifetime of a fluorophore depends on its molecular environment but not on its concentration, unlike fluorescence intensity that depends on it. Lifetime-based measurements overcome the limitations of intensity-based methods, which are dependent to experimental conditions, such as signal cross-contamination, probes concentration, variations of intensity excitation and exposure time and photobleaching of the fluorophores. Lifetime measurements are not dependent on the intensity signal of the laser source of the microscope and are generally insensitive to moderate levels of photobleaching. Furthermore, the advantage of fluorescence lifetime is its sensitivity to biophysical parameters such as pH, polarity, refractive index of the medium, temperature, ions concentrations, pressure, viscosity quenchers and electric potentials, providing information about the local microenvironment around a probe.

The early methods for fluorescence lifetime imaging were described in the late 1980s, by using a phase method. The nanosecond time resolution was achieved by using a gain-modulated image intensifier as an optical phase-sensitive detector. Lifetime parameter was determined by measuring the phase-sensitive intensity with several detector phase angles and, then, the lifetime image was accomplished with a frequency-modulated image intensifier.

Nowadays, FLIM techniques can be classified into two main methods for the detection and acquisition of the fluorescence time-resolved data: the time-domain and the frequency-domain method. The time-domain method is based on the Time Correlated Single Photon Counting (TCSPC) FLIM, which

is an extension of the classic TCSPC. The sample is scanned by the focused beam of a high-frequency pulsed laser. Data recording is based on detecting single photons of the fluorescence light, and determining the time delay between the emitted photons and the laser excitation pulses. From these parameters, a photon distribution over the spatial coordinates, *x*, *y* and the times of the photons, *t*, after the laser pulses is reconstructed. The result is a three-dimensional data array that represents the pixels of the two-dimensional scan, in which each pixel contains photons in a large number of time channels for consecutive times after the excitation pulses. It also delivers the best lifetime accuracy or photon efficiency, for a given number of photons detected from the sample. Moreover, TCSPC FLIM is perfectly compatible with confocal and multiphoton laser scanning microscopes and it takes advantage of the optical sectioning capability of confocal or multiphoton scanning. The wavelength of the photons is obtained by splitting the fluorescence light spectrally and projecting the spectrum on a photomultiplier (PMT) tube. As a disadvantage, TCSPC FLIM needs a long time for data acquisition.

The alternative method of measuring the decay time is the frequency-domain or phase-modulation method. Time-domain data have intensity values in subsequent time channels. In the frequency-domain, these time-domain data are translated into amplitude and phase values at multiples of the signal repetition frequency. The frequency of the excitation laser source is typically between 10-100 MHz, so its reciprocal frequency is comparable to the reciprocal of the decay time τ (1-10 ns). The frequency-domain method measures the harmonic response of the system. The sample is excited by a sinusoidal modulated source. The emission signal appears as a wave that is demodulated and phase shifted with respect to the excitation source. The phase shift and modulation are used to obtain the lifetime of the fluorophore. For a single exponential decay, the phase (φ) and modulation (M) are used to calculate the phase (τφ) and modulation (τm) lifetimes. Detection of frequency-domain FLIM data is possible by wide-field-excitation and a gain-modulated camera, or by scanning and detecting the fluorescence by gain-modulated point-detectors. The photon efficiency of frequency-domain FLIM

depends on a number of instrumental details. The efficiency increases with the modulation degree in the excitation light source and in the detectors. Problems may occur at extremely low intensities, when the detector, on average, delivers less than one photon within the time interval of the phase calculation[64].

FLIM technique has been used in several applications in biological studies, in particular, due to the sensitivity of lifetime to the molecular microenvironment around the fluorescent probe and to its independence to the probe concentrations. In recent years, a lot of biological information was collected from the lifetime studies on: (i) Fluorescence quenching by various proteins or ions interactions, (ii) lifetime variations due to the binding of a fluorophore to a biological target as DNA, RNA and NADH, (iii) protonation and de-protonation of fluorescence molecules by pH variations, (iv) aggregation of the dyes, (v) local viscosity, which changes the non-radiative decay rate of the fluorophore with high degree of internal flexibility, (vi) identification of nanoparticles in biological tissues.

However, one of the the main applications of the FLIM technique is related to the detection of the FRET process. Combination of FLIM and FRET allows the measurement of lifetime dynamics pixel-by-pixel and thus mapping of its spatial distribution overcoming the limitation of the conventional intensity-based FRET detection. FLIM-FRET techniques are based on the measurement of the fluorescence lifetime of the donor. Molecular interaction between donor and acceptor will result in the quenching of donor fluorescence. This donor fluorescence quenching will result in a decrease of the fluorescence lifetime, due to the energy transfer to the acceptor molecule, which introduces an additional non-radiative process from the excited state to the ground state as described in the previous section. The amount of lifetime reduction is directly correlated with the experimental FRET efficiency E, which is a function of the distance between donor and acceptor [65][66][67][68]

1.3 Super-resolution techniques

1.3.1 The diffraction limit

The resolution in an optical microscope is limited by the diffraction of light by the sample and by the objective lens. The resolution limit is often referred to as the diffraction limit, which restricts the capability of the system to distinguish between two objects separated by a lateral distance less than approximately half the wavelength of light used to image the specimen. The process of diffraction involves the spreading of the emitted light after the interaction with single point-like source of the sample, producing an image of the point source, broadened into a diffraction pattern with a point profile larger than the original point.

In a diffraction-limited optical system, the smallest spot of light that can be focused in a dark background is reproduced as an Airy pattern, a disk surrounded by circular rings. Objects that are smaller than the diffraction limit will produce the typical Airy distribution, described as the Point Spread Function (PSF). PSF is referred to the intensity distribution of the point-like source in the lateral (x,y) and axial (z) dimensions, where in a diffracted-limited optical microscope achieve a resolution of 180-200 nm in the best case. The lateral and the axial distribution of the PSF provides a measurement of the spatial resolution through the Full Width Half Maximum (FWHM). According to the Rayleigh criterion, two point sources observed in the microscope are resolved when the distance between two PSF is larger than the distance between the central spot of the Airy disk and the first dark region surrounding it. The Rayleigh resolution is given by:

$$R_R = 0.61\frac{\lambda}{NA} \qquad (1.11)$$

where λ is the wavelength of light and NA is the numerical aperture of the objective. NA is the product of the refractive index (n) of the immersion medium and the sine of the angular aperture of the lens ($\sin\alpha$). This

description is referred to the lateral resolution of optical microscope as showed by the Ernst Abbe' law in 1873:

$$R_{(x,y)} = \frac{\lambda}{2NA} \tag{1.12}$$

Notably, a similar consideration can be applied to the measurements of axial resolution. To define the axial resolution is common to use the 3D diffraction pattern of a point source, containing both in-focus and out-of-focus information. Whereas the lateral resolution corresponds to the distance between two diffracted-points source, equivalent to the central cross-section of the 3D diffraction pattern, the axial resolution can be defined as the distance of diffraction points along the axial direction. According to Rayleigh criterion the axial resolution of the 3D diffraction pattern is given by:

$$R_z = \frac{2\lambda n}{NA^2} \tag{1.13}$$

where n is the refractive index of the medium. Note that R_z narrows inversely proportionally with the square of the NA, in contrast to the lateral resolution limit [69][70][71].

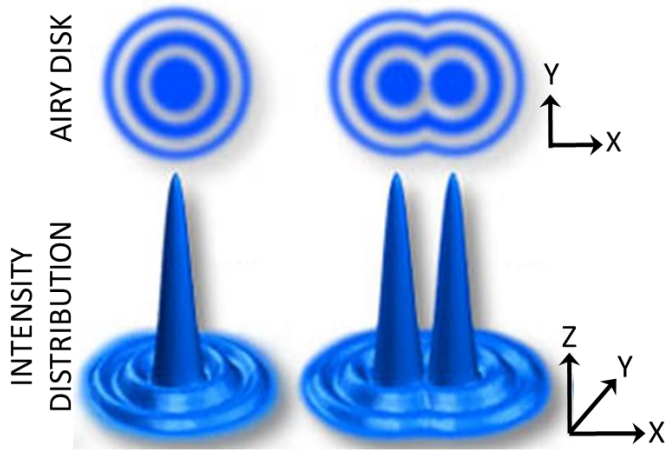

Figure 1.2. The Airy pattern. Illustration of the intensity distribution of the Airy disk in the lateral (**x**,**y**) and axial (**z**) dimensions. It is referred to a PSF and describes the diffraction pattern of a point source of light (such as a single fluorophore).

1.3.2 Beyond the diffraction limit: super-resolution methods

In the past decades, fluorescence microscopy has proven to be essential in modern biomedical research. Fluorescence microscopy represents a non-invasive tool to investigate single biological molecules, cells and tissues, with high specificity due to the use of fluorescent proteins. The large variety of fluorescent probes includes all the colors of the visible spectrum, allowing the investigation of multiple target-molecules by multi-color imaging in fixed and living specimens. Unfortunately, most of the biological processes occurs in the range of a few nanometers and the conventional fluorescence microscopy, as confocal imaging microscopy and wide-field microscopy is not able to adequately resolve the molecular details, due to the diffraction barrier imposed by Abbe's limit. In last years, the birth of super-resolution microscopy enables to overcome the impenetrable resolution barrier to light microscopy. Several techniques have been developed to extend the spatial resolution of conventional microscopy and can be broadly divided into two categories: one based on spatially patterning of excitation light, such as Stimulated Emission Depletion (STED) and Structured Illumination Microscopy (SIM), and the other based on single molecule localization microscopy (SMLM). Most of these methods have been applied to image chromatin and nuclear organization at the nanoscale. Below, I briefly explain the principles of these methods and how each method has been used to visualize nuclear organization.

- Stimulated Emission Depletion (STED)

  STED microscopy was first developed in 1994 by Hell S.W. and co-workers, breaking the diffraction barrier and opening the doors to the visualization of intracellular structures and dynamics beyond the optical resolution limit. As conventional fluorescence microscopy, the STED technique preserved advantages, such as multi-target visualization, high molecular specificity and low invasiveness to biological specimens. The basic principle of STED microscopy is based

on the first excitation of a fluorescent probe from the ground-state to an excited-state within a diffraction-limited volume, and the subsequent de-excitation through a stimulated emission by using a depletion beam.

In particular, in a typical STED microscopy implementation, the sub-diffraction resolution is obtained by overlapping the Gaussian excitation beam of a scanning microscope with a second beam, called the STED beam, which is tuned in a red-shift wavelength to de-excite the fluorophores through stimulated emission. The classical doughnut-shape of the STED beam is generated by inserting a 0–2π vortex phase plate before the objective, which creates a zero-intensity point in the center where the fluorophores are able to emit photons through spontaneous emission. In the overlapping region of the focal plane, the high intensity of the STED beam saturates the stimulated emission process forcing all the peripheral fluorophores to emit at the same wavelength of the STED laser (OFF state)[28]. Therefore, the superimposition of the two beams leads to a super-resolution imaging along the three dimensions, where the FWHM of PSF of focal point decrease with increasing STED beam intensity.

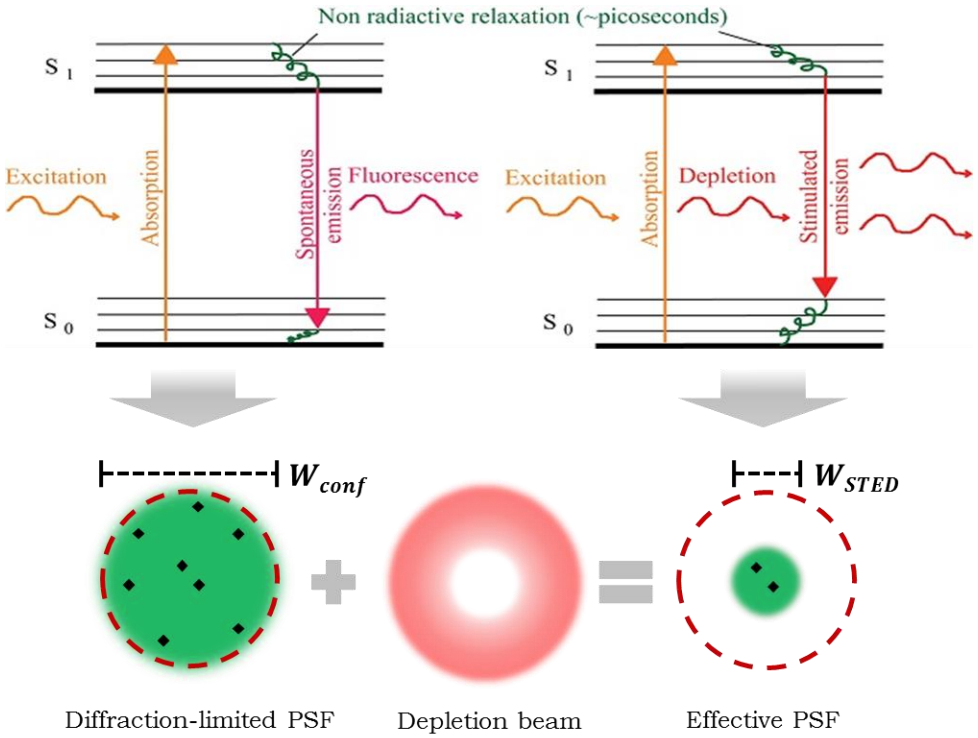

Figure 1.3. STED principle. The STED depletion beam is superimposed to the excitation beam in the focal plane. Through the stimulated emission phenomena, in the overlapping region the fluorophores are forced to emit ate the STED wavelength, leading to a reduction in the width *(ω)* of the PSF.

Under these conditions, the achievable resolution can be expressed as:

$$\Delta r = \frac{\lambda}{2NA\sqrt{1 + I_{STED}/I_S}} \qquad (1.14)$$

Where λ is the wavelength, NA is the numerical aperture of the objective, I_{STED} is the irradiation intensity of the STED-beam and I_s is the saturation intensity at which the stimulated emission has the same rate as the fluorescent pathway.

Theoretically, the resolution of STED microscopy can reach the molecule's size, i.e. the ultimate limit of a fluorescent microscope, but, in practice, it is limited by the signal-to-noise ratio (SNR) to obtain an effective resolution improvement. SNR is dependent by several conditions such as the detection efficiency, the fluorophore's brightness and photostability, and the focal intensity distributions of the lasers. For maximum SNR, the depletion beam and the excitation beam must overlap with nanometer accuracy, and the residual STED intensity in the 'zero'-intensity point must be minimized.

Moreover, a complete quenching of peripheral fluorophores requires much higher intensities in a temporal window of few nanoseconds, which can cause problems such as photobleaching and phototoxicity, making STED microscopy a limited method for live-cell imaging. A useful approach to reduce the effect of photobleaching and phototoxicity makes use of fluorophores with a low-absorption cross-section at the wavelength of the depletion beam, decreasing the probability of exciting the fluorophores with the STED beam. Moreover, the occurrence of fluorescence background, attributed to the early fluorescence detection from the periphery prior to enough STED light

exposure, affects both super-resolution imaging and quantitative analysis.

In last years, many strategies has been implemented to fight against these issues linked to the power level of the STED laser. One of these strategies is the enhancement of the optical resolution by using the temporal information due to the variations of the fluorescence lifetime of the fluorophores under the STED stimulations. For the acquisition of temporal information, the STED setup requires a TCSPC module connected to the detector, with which is possible to record the different time decays of the fluorophores in the focal plane. STED beam causes a decrease of fluorescence lifetime, giving the possibility to spatially distinguish the fluorophores in the inner and outer region of the doughnut-shape. Time-gated Continuous-Wave STED microscopy (gCW-STED) and Separation of Photons by Lifetime Tuning (SPLIT-STED) represents two important methods, which increase the spatial resolution by using a temporal dynamics of fluorophores.

The gCW-STED is a method based on the time-gating detection of fluorescence signal, in which the photons are collected after a time delay T_g from excitation pulse. As explained above, STED beam causes a decrease of the fluorescence lifetime of the molecules with respect the spontaneous emission. By this concept, the time-gating detection is a powerful tool to achieve the spatial resolution by filtering the lifetime decays in the excitation volume. The photons are collected after the interval between the time-delay T_g and the excitation pulse, blocking the early fluorescence produced by both the zero-intensity region and the peripheral overlapping region. By the analysis of fluorescence dynamics, is possible to reject the photons in the periphery, affected by the STED beam, and highlights photons close to the central region, emitted by spontaneous emission. Theoretically increasing the time delay is possible to achieve the best spatial resolution not affecting the STED power. Roughly speaking, gCW-STED can be a powerful tool for biological studies, alleviating the photobleaching and photodamage, as shown by images of

microtubules of fixed COS7 and HeLa cells [72]. In contrast, the discard of photons due to the time delay leads to a loss of intensity signal and the presence of a low signal-to-noise ratio may compromise the temporal analysis [73][74][75].

The SPLIT-STED approach represents the application of the basic concept of the SPLIT method to STED microscopy. SPLIT is based on the separation of photon by lifetime tuning. The excitation volume under the CW-STED excitation is spitted into two concentric areas, by decoding the spatial-temporal information provided by the fluorescence lifetime of the excited fluorophores. The temporal information is encoded in an additional temporal channel, recorded by the TCSPC module connected to the STED setup. STED beam was used to generate a fluorescence lifetime gradient from the center to the periphery. With the SPLIT algorithm, the fraction of the photons corresponding to the central area (longer fluorescence lifetime) are extracted, producing an improvement of the spatial resolution [76].

As a super-resolution method, STED microscopy has been applied to the investigation of chromatin organization at the nanometer scale. In particular, STED imaging focused on the study of the main components of chromatin architecture: the DNA fiber and the DNA-associated proteins. Important results have been achieved in vitro and in vivo DNA imaging. In vitro imaging, the improvement resolution of STED demonstrated the structural conformation of the phage lambda DNA, by using the DNA-intercalating dye YOYO-1. Afterwards, the introduction of novel SiR-DNA probes in substitution to traditional DNA-binding dye, such as DAPI and Hoechst, allowed to estimate the chromatin interaction with the nuclear structures (i.e. NPC) and the visualization of the DNA loops in the mitotic chromosomes in live and fixed cells. These probes present a higher-photostability and a lower-phototoxicity with respect to the dyes excited with UV light. Moreover, STED microscopy provided higher details of chromatin proteins, which modulate the gene expression, such as PCNA and gH2AX, involved in

the replication pathway and in the DNA-damage repair process, respectively. [77][78][79][80].

- Structured Illumination Microscopy (SIM)

Super-resolution structured illumination microscopy (SR-SIM) is a powerful implementation, capable of doubling resolution in both the lateral and axial dimensions and applicable to a large variety of biological samples. Structured-illumination microscopy (SIM) is a concept that combines wide-field imaging and illumination of a sample with a known pattern of excitation light, and achieves a two-fold resolution improvement, illuminating a sample with a series of sinusoidal stripped pattern of high spatial frequency [29]. In the SR-SIM microscope via optical fiber, the laser beam is collimated and linearly polarized, and then a phase grating generates the illumination pattern of the image in the lateral direction. The phase grating diffracts the beam in several orders allowing the illumination of the sample at different angles. It is acquired several images of the sample at different illumination phases in order to obtain through the Fourier transform a high-resolution image. In this method, the sample is illuminated with spatially structured excitation light, with which the normally "hidden" high-resolution information has revealed in the observed image as moiré fringes. To improve the spatial resolution is needed the acquisition of such images to be processed. The basic concept of Structured Illumination Microscopy is based on the "moiré effect". The so-called "moiré fringes pattern" is produced by the superimposition of two different patterns. One pattern represents the unknown sample structure given by the spatial distribution of the fluorophores and the other pattern is the structured excitation light. The moiré pattern is generated by the emission light, which is proportional to the product of the fluorophore concentration and the excitation source. The moiré fringes contain the "hidden" information of the sample, achieving the high-resolution improvement. Mathematically, the diffraction limited-PSF is converted into a reciprocal space through the Fourier transform

in a form of an observable region, which is limited by the Optical Transfer Function (OTF) of the microscope. OTF represents the normalized Fourier transform of the PSF of the optical system. All information inside the OTF is observable, while all information outside not. The observed circular region is defined as OTF support with a radius of d_0, where the high-frequency information residing outside of this area cannot be observed. The conventional microscope acts as a low-pass filter, only detecting information that resides within the observable circular region of radius d_0 around the origin of reciprocal space and allowing the acquisition of frequencies with a magnitude less than or equal to that of d_0.

Structured illumination does not modify this central region, but it moves information into the region from the outside, and thereby makes that information observable. The Fourier transform of the observable region contains three non-zero point: one is at the origin of the normal image of spatial frequencies (the center of circle) and the other two are offset frequency images that are centered on the edge of the original field. These offset images, with a defined radius d_1, contain higher spatial frequencies that are not observed using conventional microscopes. Illuminating the sample with this structured light the resulting image will also contain the moiré fringes corresponding to the product of frequency mixing. This increases the observable region (OTF support), which now contains also the high frequencies that originates in two offset regions. The parts of those offset circles with radius d_1 that fall outside the normally observable region represent new information, which is not accessible in a conventional microscope, increasing the spatial resolution of the system. The obtained resolution limit becomes $2d_0$ because the resolution is stretched from d_0 to $d_1 + d_0$ and the magnitude of d_1 cannot exceed that of d_0. The final super-resolved image is the product of three or more images with different phase illumination, containing twice the spatial resolution of wide-field fluorescence microscope.

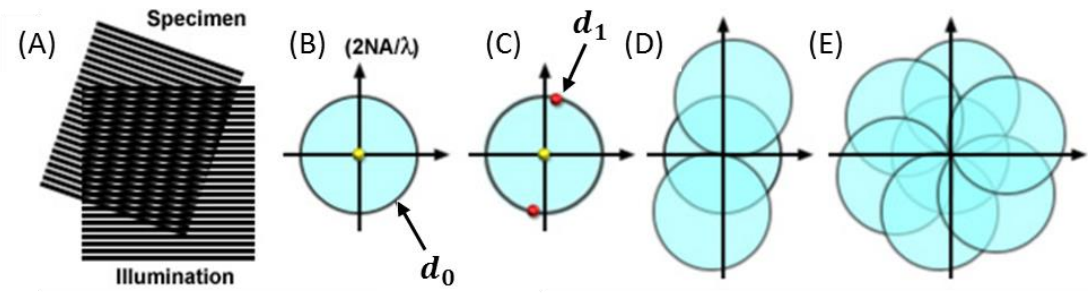

Figure 1.4. SIM principle. (A) The "moiré fringes pattern" is generated by the overlapping of two different patterns of patterned lines. **(B)** The observable circular region of radius d_0 of reciprocal space produced by a conventional microscope (which is analogous to its diffraction pattern) is limited at the edges by the highest spatial frequencies that the objective can transmit (2NA/λ). **(C)** SIM technique, through the Fourier transform, moves information into the region from the outside, with a defined radius d_1, contain higher spatial frequencies. The first order spots occur at the edge of the observable field (shown here as red dots on the d_0 boundary). **(D)** Due to frequency mixing, the observable regions also contain, in addition to the normal image of spatial frequencies (center circle), two new offset frequency images that are centered on the edge of the original field. Finally, in **(E)**, shown is a set of images generated from three phases orientations, yielding a real image that contains twice the spatial resolution of a conventional wide-field microscope (ZEISS microscopy).

Despite the advantages, such as the multi-color imaging, the use of conventional fluorophores and its applicability to live cells, SR-SIM technique presents some practical drawbacks. The lateral resolution achieved by SIM (c.a. 100 nm) is about twice the diffracted-PSF, unlike other super-resolution techniques, such as STORM/PALM and STED, which are able to obtain a resolution less than 50 nm. Moreover, small deviations of the reconstruction parameters, such errors calibration of the system, in grating, mismatch of the refractive index, or low quality of the sample from the correct parameters often lead to artifacts in the final image.

The basic principle of SR-SIM has been extended to other implementations, such as three-dimensional SIM (3D-SIM), total internal reflection fluorescence-SIM (TIRF-SIM) and saturated-SIM (SSIM), with the aim to develop the method and increase both axial (3D-SIM) and lateral resolution (SSIM).

The SIM technique turned out to be a powerful tool for the visualization of nuclear structures inside eukaryotic cells. In recent years, 3D-SIM has been implemented to several studies. Schermelleh et al. provided

multi-color images of chromatin component at high resolution. With 3D-SIM, they simultaneously imaged the higher-order chromatin structure, the localization of nuclear pore complexes (NPC), the nuclear lamina, and the peripheral chromatin in C2C12 cells [81]. Furthermore, Markaki et al. studied the nuclear topography and distribution of RNA transcription and DNA replication in murine mammary tumor C127 interphase nuclei by 3D-SIM. 3D-SIM revealed a network of channels and wider lacunas, known as interchromatin compartment [82]. More recently, Wanner et al. used SR-SIM to analyze the relationship between plant chromosomes and distribution of centromere-associated proteins [83].

- Single-Molecule Localization Microscopy (SMLM)

In fluorescence microscopy, the various cellular structures are labelled with fluorescent dyes. Because of the diffraction limit, the fluorescence emission signal, provided by discrete fluorophores, hides the real cellular structures, composed of discrete molecules. In last twenty years, with the development of the single-molecule detection techniques, it was possible to acquire the signal from a single molecule by using a wide-field fluorescence microscope equipped with a sensitive charge-coupled device (CCD) camera. In a conventional wide-field microscope, the FWHM of a single-molecule profile appears as diffraction limited, in which the PSF width is around 200 nm or more. In a single molecule detection, the peak of the PSF can be used to identify the centroid of the fluorescence signal of the single fluorophore, localizing the position of the molecule. Every single photon is detected by the camera, recording its position with precisely. A single molecule image is obtained of more than one photon (until thousands of photons), and the number of photons acquired is equivalent to number of times to measure the single molecule. The error in determining the molecule position (i.e., the localization precision) scales approximately with the inverse square root of the number of photons detected from the molecule. It can be expressed by:

$$\Delta = \frac{\delta}{\sqrt{N}} \qquad (1.15)$$

where in δ is the width of the diffraction-limited PSF and N is the number of photons detected. Roughly speaking, the more the photons are collected and higher is the localization precision. In a diffraction-limited image can be present thousands of molecules, complicating the single-molecule detection. In this way, is essential to have fluorophores that is possible to control, to get super-resolution image with SMLM method. In this approach, photo-switchable (or photoactivatable) probes are used to control the fluorescence emission in time, so that only a subset of fluorophores is activated at any moment, allowing their localization with high precision. These fluorophores can be converted between a fluorescent ("on") state and a dark ("off") state or states that fluoresce at different wavelength. These fluorescent probes, represented by organic dyes and fluorescent proteins, can be turned in the fluorescence state with a very low activation light and only a random small fraction of fluorophores is activated at any time. This process allows to localize the molecules individually and then turn them off by switching to a reversible dark state or bleaching. The repetition of the acquisition sequence of activation, imaging and deactivation is possible to accumulate the position of many subset of fluorophores to be mapped and reconstruct a super-resolution image. The principle of SMLM has been developed in various implementations, known as Photoactivated Localization Microscopy (PALM), Stochastic Optical Reconstruction Microscopy (STORM), and fluorescence-Photoactivation Localization Microscopy (fPALM). The three-dimensional nature of the biological structures extended the super-resolution single-molecule methods to 3D imaging. The highest axial resolution in 3D (f)PALM/STORM is achieved by using two opposing objectives to determinate the *Z* position, which leads to *Z* localization of single molecules below and above the *XY* focal plane. As all methods, the SMLM is intrinsically connected to some limitations

related to the properties of the probes and to the high density of the molecules (Nyquist criterion) in the sample, which can affects the achievement of super-resolution image.

The various SMLM implementations have been used for the visualization of nuclear organization, shading light to the molecular pattern of the nuclear structures, such as chromatin, at the nanometer level. In 2015, Ricci et al. used STORM technique to visualize the structure of chromatin fiber by imaging the histone protein H2B with a resolution of c.a. 20 nm [84]. In the same year, Prakash et al. applied a novel method based on the photo-conversion of DNA dyes to describe the epigenetic landscape of meiotic chromosomes in mouse oocytes[85]. More recently, Nozaki et al. developed a nuclear imaging method to visualize the higher-order chromatin structures and their dynamic aspects in live HeLa cells, combining super-resolution imaging PALM and single nucleosome tracking with a fused histone H2B with photoactivatable (PA)-mCherry [86].

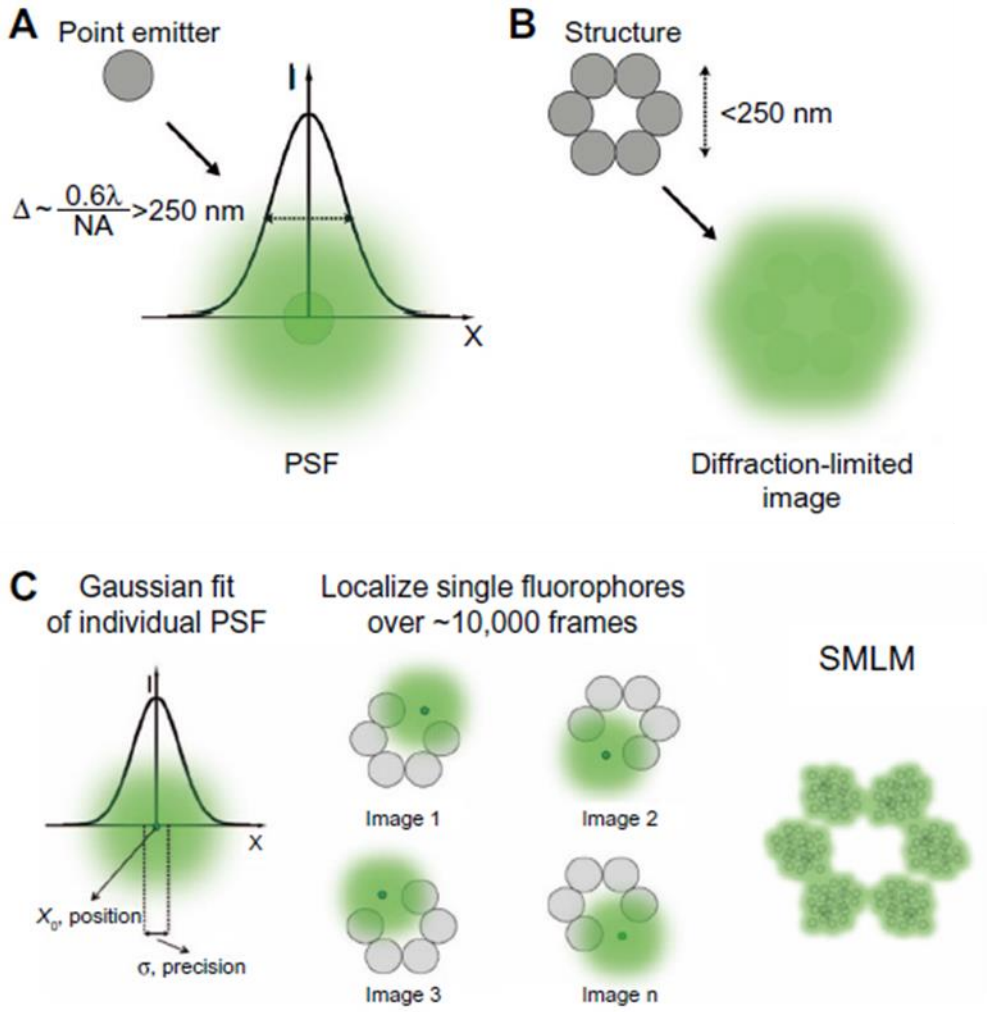

Figure 1.5. SMLM principle. (A) Light emitted by a point source (such as a single fluorophore) is detected by the optical microscope as a PSF of width which depends on the wavelength of emission and the numerical aperture of the objective. **(B)** The diffraction law limits the optical resolution, producing a diffraction limited-PSF. **(C)** In SMLM, the position of individual emitters is obtained by fitting of their intensity profile detected by a charge-coupled device (CCD) camera (left). The acquisition (middle) relies on the low density of emitting fluorophores (<1/250 nm). The single positions are then combined to reconstruct the super-resolved image (right) [87].

Chapter 2

2. The phasor approach in time resolved microscopy

In last decades, time-resolved fluorescence spectroscopy has proven to be a powerful tool for the study of dynamics of biological molecules in the chemical, physical and biological fields, by measuring the kinetic processes in the order of pico-, nano- and micro-second time scale. In particular, the temporal decays of fluorescent molecules are generally measured following two different approaches, based on the "impulse response" or the "harmonic response". The impulse response, also referred as "time domain" method, is based on a short exciting pulse of light, which yields the δ-response of the sample, convoluted by the instrument response. Alternatively, the time decays can be measured by using a modulated light at variable frequency, which gives the harmonic response of the sample, representing the Fourier transform of the δ-pulse response. This method works in frequency domain by determining the phase delay and the relative modulation of the fluorescence emission signal with respect to the frequency of the excitation source. In general, the time domain and frequency domain approaches are related to each other by the Fourier transform, providing equivalent information, but the principles and the instrumentations are different.

2.1 Time Domain VS Frequency Domain

In time domain, the sample is excited by a short pulse of light and the fluorescence response is recorded as a function of time. The δ-pulse response

$I(t)$ of the fluorescent sample is, in the simplest case, a single exponential whose time constant is the excited-state lifetime, but more frequently it is a sum of discrete exponentials, or a more complicated function; sometimes, the system is characterized by a distribution of decay times. If the duration of the pulse is not short with respect to the time constants of the fluorescence decay, the fluorescence response is the convolution product given by:

$$R(t) = E(t) \otimes I(t) \tag{2.1}$$

Where $E(t)$ is the excitation function and $R(t)$ is the response of the sample. In this case, data analysis for the determination of the parameters characterizing the δ-pulse response requires a deconvolution of the fluorescence response.

Conversely, in the frequency domain, the sample is excited by a modulated laser source and the fluorescence emission response has the same frequency but partially demodulated and phase-shifted with respect to the excitation. As shown in the figure, the phase shift φ and the modulation ratio M characterize the harmonic response of the system. The modulation ratio M (m/m_0) is equal to relative values of emission (m) and excitation (m_0) modulations, obtained from the ratio b/a and B/A components, respectively. The phase delay and modulation ratio between the excitation and the emission are related to two independent measurements, which do not need a deconvolution because the data are directly analyzed as a function of the modulation frequency.

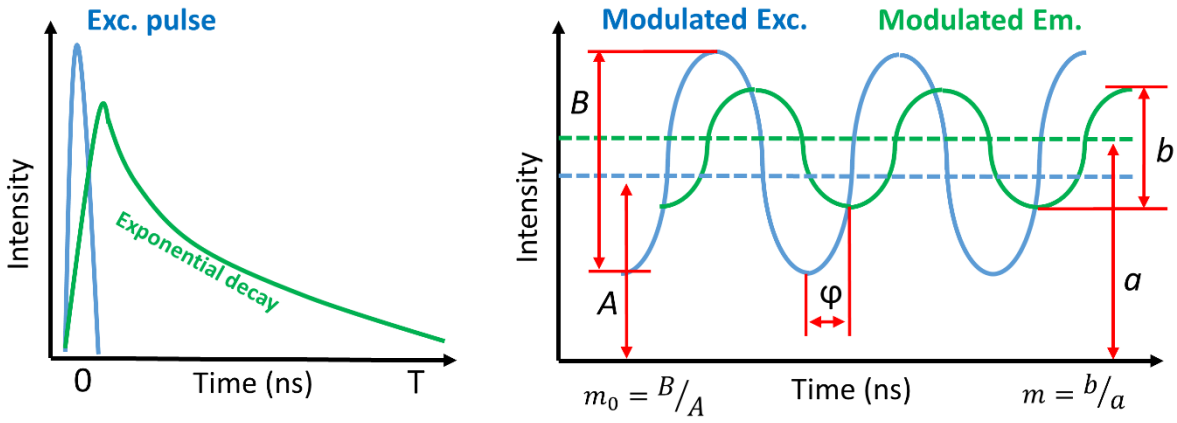

Figure 2.1. Differences between time-domain and frequency-domain methods.

It can be demonstrated that the harmonic response is the Fourier transform of the δ-pulse response [88]. In the time domain, the fluorescence decay can be generally expressed as a sum of multiple exponential decays:

$$I(t) = \sum_{i=1}^{N} a_i e^{-t/\tau_i} \tag{2.2}$$

where a_i are the pre-exponential factors, τ_i is the decay time and t is the time elapsed from the excitation pulse. If the excitation light is sinusoidally modulated, the excitation function E(t) can be written as:

$$E(t) = E_0(1 + m_0 \sin \omega t) \tag{2.3}$$

where E_0 and m_0 are the intensity and modulation of excitation pulses. If we substitute this expression in the (eq.2.1), the result for sinusoidal modulated emission is:

$$\begin{aligned} R(t) &= E(t) \bigotimes I(t) \\ &= \int_{-\infty}^{t} E(t')I(t-t')dt' \\ &= F_0[1 + m_0 \sin(\omega t + \varphi)] \end{aligned} \tag{2.4}$$

where $F(t)$ and F_0, , are the fluorescence intensities at time t and the average of F(t), respectively, φ is the phase delay between the excitation and emission, and ω is the angular modulation frequency, equal to $2\pi f$, where f is the linear modulation frequency. M and φ represent, respectively, the modulation and the phase shift of the fluorescence emission and are related to I(t) by [88]:

$$Msin(\varphi) = \left(\int_0^{\infty} I(t)\sin(\omega t)dt\right) \Big/ \int_0^{\infty} I(t)dt \tag{2.5}$$

The passage from time to frequency domain can be also expressed in the form:

$$Me^{-i\varphi} = \left(\int_0^\infty I(t)e^{ji\omega t}\delta dt\right) \Big/ \int_0^\infty I(t)dt \tag{2.6}$$

This expression shows that the harmonic response, expressed as the modulation M and phase shift φ at the frequency ω, is the Fourier transform of the δ-pulse response.

The frequency domain equations, which relate the phase shift φ and the modulation ratio M to the time domain response $I(t)$ of a time-resolved system are usually expressed via the following relations:

$$\varphi = \tan^{-1}\left(\frac{s}{g}\right) \tag{2.7}$$

$$M = (s^2 + g^2)^{1/2} \tag{2.8}$$

Where the functions s and g are the sine and cosine Fourier transforms of the impulse response:

$$s = \frac{\int_0^\infty I(t)\sin(\omega t)\,dt}{\int_0^\infty I\,(t)\,dt} \tag{2.9}$$

$$g = \frac{\int_0^\infty I(t)\cos(\omega t)\,dt}{\int_0^\infty I\,(t)\,dt} \tag{2.10}$$

These equations provide the mathematical relationship between the impulse (time domain) and harmonic (frequency domain) response methods.

For the single-exponential decay case, the δ-response of the sample is described as:

$$I(t) = ae^{-t/\tau} \tag{2.11}$$

The phase delay and modulation are linked to the fluorescence lifetime (decay time) by:

$$\varphi = \tan^{-1} \omega\tau \tag{2.12}$$

$$M = \frac{1}{(1+\omega^2\tau^2)^{1/2}} \tag{2.13}$$

In the case of a multi-exponential decay, where the fluorescence decay is characterized by a set of N-decaying components, the response of the δ-function excitation and the s and g parameters are given by the following equations:

$$I(t) = \sum_{i=1}^{N} a_i e^{-t/\tau_i} \tag{2.14}$$

$$s = \omega \sum_{i=1}^{N} \frac{f_i \tau_i}{1+\omega^2 {\tau_i}^2} \tag{2.15}$$

$$g = \sum_{i=1}^{N} \frac{f_i}{1+\omega^2 {\tau_i}^2} \tag{2.16}$$

where:

$$f_i = \frac{a_i \tau_i}{\sum_{i=1}^{N} a_i \tau_i} \tag{2.17}$$

Looking at these expressions is clear the relationship between f_i, the fractional intensity of the i-th components and a_i, the pre-exponential term associated with the lifetime (τ) i-th components. If N=1 we obtain the s and g parameters of the single-exponential decay. By the eq.2.12-2.13 is possible

to determine the values of the phase and the modulation, related to the fluorescence lifetime:

$$\tau_\varphi = \frac{1}{\omega}\tan^{-1}\varphi \tag{2.18}$$

$$\tau_M = \frac{1}{\omega}\left(\frac{1}{M^2} - 1\right)^{1/2} \tag{2.19}$$

If the fluorescence decay is a single exponential, τ_φ and τ_M are equal for every modulation frequency. Instead, in the case of multi exponential decay τ_φ and τ_M and their values depend on the modulation frequency [89][90].

2.2 Phasor Plot: a powerful tool for data analysis.

The temporal information obtained by the harmonic (frequency) and pulsed (time) response methods can be analyzed by using the phasor plot. The phasor approach can be applied to several fluorescence microscopy techniques abled to provide an image with a temporal information in an additional channel. In the simplest model the additional information is represented by the fluorescence time decay (lifetime), in which every single pixel of the acquired image contains the spatial coordinates (x, y) and the temporal coordinate (t).

The phasor plot is the graphical representation of the passage from the histogram of the time delays (time domain) to the phasor space (frequency domain), where each decay component is identified by a vector with the two phasor coordinates (g, s), corresponding to the x, y coordinates of the phasor plot.

Time domain and frequency domain methods make use of different equations to transform each time decay component in the g and s coordinates. In time domain, each decay trace can be plotted through the sine and cosine Fourier

transforms of the measured decay data. The $g_{x,y}$ and $s_{x,y}$ coordinates related to the free decay after excitation $I_{x,y}(t)$ at pixel location (x, y), with angular frequency (ω) is given by:

$$s_{x,y}(\omega) = \frac{\int_0^\infty I_{x,y}(t)\sin(\omega t)\,dt}{\int_0^\infty I_{x,y}\,(t)\,dt} \tag{2.20}$$

$$g_{x,y}(\omega) = \frac{\int_0^\infty I_{x,y}(t)\cos(\omega t)\,dt}{\int_0^\infty I_{x,y}\,(t)\,dt} \tag{2.21}$$

Whereas, in frequency domain, each pixel of the image is composed of phase delay $(\varphi_{x,y})$ and modulation ratio $(M_{x,y})$, measured at a given angular frequency (ω). The $g_{x,y}$ and $s_{x,y}$ coordinates in the phasor plot are:

$$s_{x,y}(\omega) = M_{x,y}\sin\left(\varphi_{x,y}\right) \tag{2.22}$$

$$g_{x,y}(\omega) = M_{x,y}\cos\left(\varphi_{x,y}\right) \tag{2.23}$$

In eq.2.15-2.16, if the fractional contribution of the i-th components f_i is equal to 1, we obtain the s and g phasor coordinates of the single-exponential decays:

$$s(\omega) = \frac{\omega\tau}{1+\omega^2\tau^2} \tag{2.24}$$

$$g(\omega) = \frac{1}{1+\omega^2\tau^2} \tag{2.25}$$

These equations are related by the following expression: $(g-0.5)^2 + s^2 = 0.25$. From this relationship, the single-exponential decays lies on the semicircle curve centered in $(g = 0.5, S = 0)$ in the phasor plot. The curve is called the *Universal Semicircle*, which describes the trajectory of the exponential

decays. The longer exponential decays, with an high phase angle are close to the origin of the phasor plot (0,0), whereas the smaller decays, with a small phase angle lies close to the point (1,0) [91][92][93].

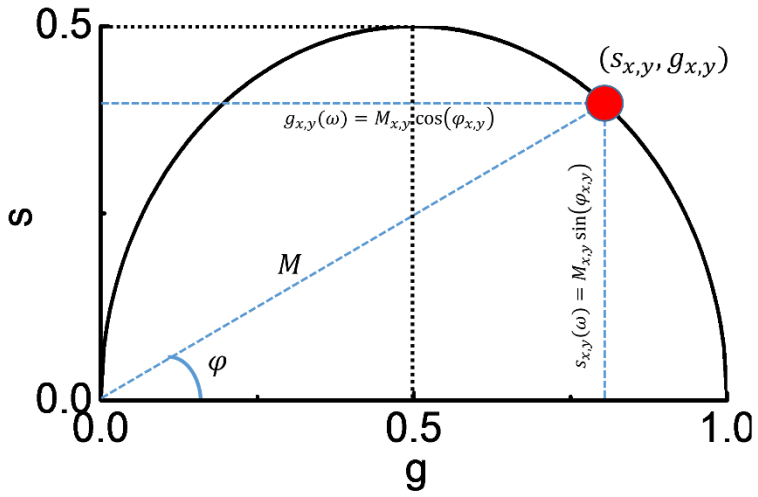

Figure 2.2. Graphical representation of a phasor plot. The single-exponential phasor ($s_{x,y}$,$g_{x,y}$) lies on the universal semicircle. The phasor is characterized by a modulation M (radius of the phasor) and a phase delay φ (angle of the phasor). The phasor coordinates g and s correspond to the x and y coordinates.

The position of the phasor along the semicircle can be adjusted upon the modulation frequency. If we have a population of molecules with the same single-exponential decay, the phasor point shifts depending on value of the modulation frequency. Usually, a population of molecules is composed of n-components, emitting n-exponential decays or is present only one component with more than one exponential decay. In this case, the phasor of this complex population does not lie on the semicircle, but inside. The location of the phasor is a linear combination of the individual phasors of the single-exponential components. For instance, the phasor point of a population composed of two different components lies on the line connecting the two phasors of representing each individual component. The position of the "mixed phasor" along the straight line depends on the contribution of the single fractional components (fractional intensity) f_1 and f_2 to the mixed population. In a more complex case, the mixed phasor is the result of two populations with multi-exponential decay components, in which the phasor decomposition is often not to solve the individual single-exponential decay

components. In the case of many molecular populations, all the possible locations of the mixed phasor are inside the polygon, where the vertices represent the phasors of the individual molecular components (e.g. a triangle for 3 components).

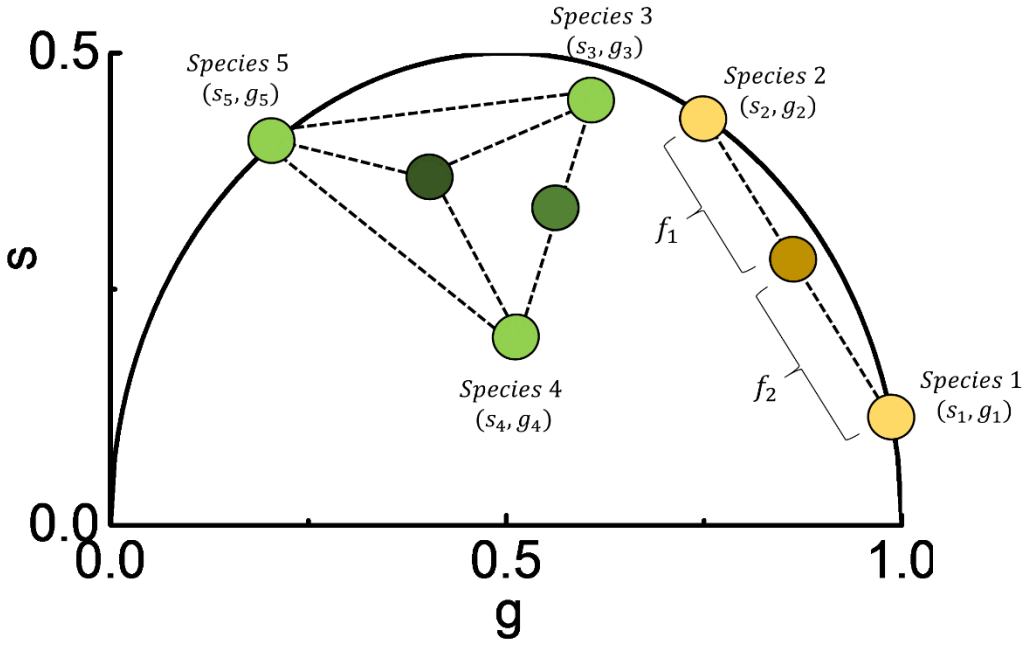

Figure 2.3. N-components phasors in the phasor plot. In the phasor plot are represented the multi-exponential phasors, generated by the combination two and three single-exponential phasors. Shown are the Phasor of a mixture of the two single lifetime species (species 1 and species 2) and the phasor of a mixture of the three single-lifetime species (species 3,4 and 5). These phasors lies on the line joining the phasors of the two components or inside the polygon of the three components.

The single- and multi-exponential decays in the phasor plot are measured with the fundamental frequency, also called First Harmonic frequency. The phasor analysis can be performed with the following higher harmonics, all periodic at the fundamental modulation frequency. For instance, if the fundamental frequency w_0 is 80MHz, the First harmonic frequency ($w = w_0$) will be 80 MHz, the Second harmonic ($w = 2w_0$) 160MHz, the Third harmonic ($w = 3w_0$) 240 MHz and any addition of waves with these frequencies will be periodic at 80MHz. The use of different harmonics change the position of the phasor in the phasor plot, caused by the variations of the value of φ and M, without modify the exponential decay value. This is a powerful property of the phasor approach, which is able to separate phasors that in the First

harmonic overlap. In the First harmonic, two different phasors could have the same position in the phasor plot, even if they are the combination of different individual fractional components. By using higher harmonics, the sensitivity of phasor decomposition increases and the two phasor can be separated, distinguishing the exponential decays of each phasor [94].

1.3 The phasor approach in FLIM microscopy

Fluorescence lifetime imaging microscopy (FLIM) is the classical time-resolved technique in fluorescence microscopy. In a FLIM experiment, the fluorescence lifetime is measured at every single pixel of the image, combining perfectly fluorescence spectroscopy and imaging. The interpretation and data analysis of the multi-exponential lifetimes at each pixel can be a complex computational task. The phasor representation is able to simplify the FLIM data analysis, providing a global view of the fluorescence exponential decays in the frequency domain (FD-FLIM), avoiding some issues of the exponential decay analysis in the Time correlated single photon counting (TCSPC). As explained in the previous section, G and S coordinates of the phasor plot provide information about the phase and the modulation, related to the fluorescence lifetimes τ_φ and τ_M at each pixel of the image. Since every molecular lifetime species has a specific phasor, we can identify molecular populations by their position in the phasor plot. It is known that one of the most common application of FLIM is related to the lifetime based-FRET detection, a spectroscopy phenomenon to measure the nanometer distance between molecules in a cell. Frequency domain-FLIM measures the average lifetime of the donor fluorescence emission in the absence and in the presence of the acceptor in each pixel of an image, assigning the pixels, which produce a quenched lifetime, to the FRET localization. It results necessary to distinguish the phasor generating by multi-exponential lifetime components from the “FRET phasor”. In the multi-exponential case, if there are two molecular species that coexist in the same pixel, all possible weighting of the two species give phasors distributed along a straight line connecting the phasors of each individual single-lifetime species. In other hand, if there are

three or more species, all the possible locations of the multi-exponential phasor are inside the polygon, where the vertices represent the phasors of the individual single-lifetime components. In the FRET case, in which the proximity of the acceptor reduces the donor-lifetime, the resulting phasor cannot lie on the straight line of the two non-interacting species, but follow another trajectory, known as FRET trajectory, corresponding to the quenching of the donor due to the transfer energy from the donor to the acceptor molecule. In the phasor space, you can distinguish a mixture of independent single-lifetime species (a linear trajectory) from lifetime variations due to FRET (a curved trajectory) without resolving the decay at each pixel into the individual single-lifetime components. In the phasor plot, the FRET process also leads to the shift of the acceptor phasor outside the semicircle. In other words, in a FLIM measurements, when a fluorescent component is an excited-state product, e.g. the delay of the emission of the acceptor produced by the energy transfer from the excited-state donor in a FRET process, its phasor moves outside the semicircle to the left, while the donor phasor moves to the right due to quenching.

Ideally, the FRET trajectory ends with the total quenching of the donor molecules, with the final point at zero value. Practically, if the FRET interaction leads to the total quenching of the donors, the FRET trajectory ends with the autofluorescence phasor. Autofluorescence in biological samples arises from biological structures and endogenous proteins as a natural emission of light and has to be distinguished from the light originating from exogenous fluorophores. The FRET phasor corresponds to a mixture of three components: the fraction of quenched donors, the unquenched donors and the autofluorescence signal, that influences the FRET trajectory. If there is a fraction of donors that cannot be quenched, the final point will be along the line joining the donor with the autofluorescence phasor.

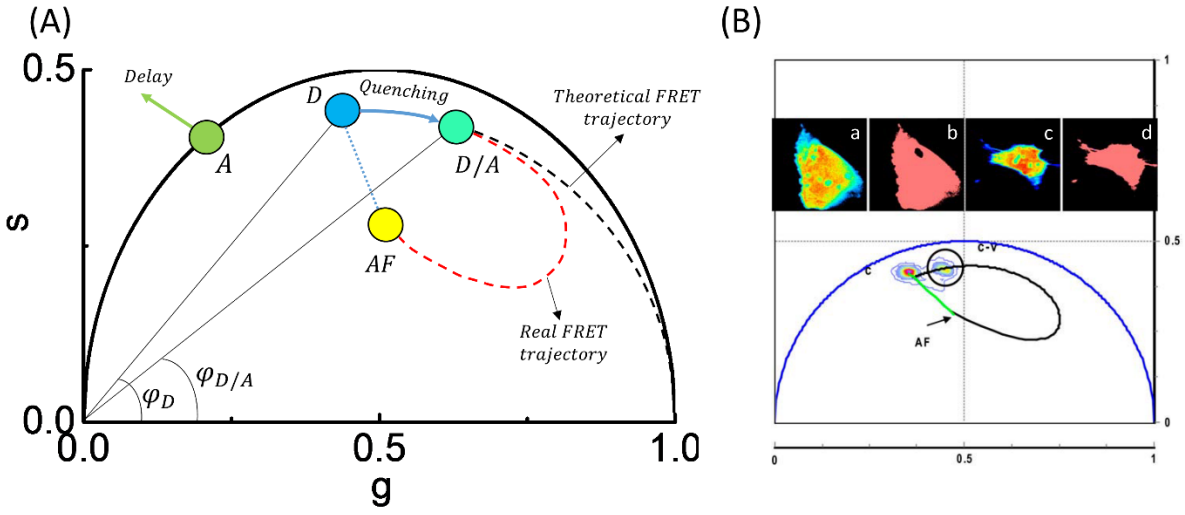

Figure 2.4. FRET measurement with the phasor approach. (A) Graphical representation of the FRET process. FRET leads to a decrease of the donor lifetime and to a shift of the acceptor phasor outside the phasor plot. The donor phasor follows the real FRET trajectory (red dashed line), also defined as the quenching trajectory. The quenching phenomenon due to FRET may be measured as decrease of a value of the phase angle (φ). **(B)** Shown are MEF cells expressing cerulean (c-only) and cerulean-venus (c-v) constructs. Phasor plot showing the clustering of phasors of the c-only and c-v cells. The curved trajectory corresponds to FRET efficiency E (Digman et al, 2008).

The recent development of fluorescent constructs, often used as donor-acceptor pairs, has been used to study FRET interaction. Cerulean-Venus construct is one of the most common artificial FRET-pair, in which Cerulean (c, a blue fluorescent protein variant serving as the donor) is attached to Venus (v, a yellow variant serving as the acceptor) with amino acid linkers of different lengths. MEF cells were transiently transfected with Cerulean (c) and Cerulean-Venus (c-v) constructs. The c-v complex showed FRET due to the proximity of the two proteins and the c-v phasor lay on the curved trajectory. The FRET trajectory also combines the phasor of the unquenched donor (c) and the autofluorescence phasor (AF), which were determined independently using the c-only cell and a non-transfected cell [95].

In recent years, Hodgson et al. developed biosensors for characterizing the dynamics of Rho family GTPases in living cells. In particular, the research group designed the RhoA single-chain biosensor and the Rac1 dual-chain biosensor. The RhoA single-chain biosensor is composed by a fragment of Rhotekin attached to RhoA as part of the same protein chain. Rhotekin binds only to activated RhoA and two different fluorescent proteins undergoing

FRET are in the chain between RhoA and the Rhotekin fragment. The binding of the fragment to activated RhoA alters the distance between the fluorescent protein, affecting FRET interaction. The Rac1 dual-chain biosensor, with respect to RhoA, is characterized by the PAK fragment bound to activated Rac1 as not part of the same protein chain. Here, intermolecular FRET design enhances sensitivity because, unlike the single chain design, FRET occurs only when the two molecules are completely bound. The dual-chain biosensor components can diffuse differently inside the cell and the bleed-through correction is required. Rac1 is known to promote membrane protrusion at the leading edge, while RhoA regulates contractility in the cell body and at adhesions throughout the cell [96]. The phasor approach is used to biosensor FRET detection, demonstrating the localization of RhoA and Rac1 activity, in according to literature. COS7 cells were transfected with both donor (CyPet-Rac1) and acceptor (YPet-PBD) before and after EGF stimulation. The phasor plot clearly showed that, after addition of EGF, the population of donor quenched increases with time and the FLIM images indicate an increase in the number of molecules undergoing FRET in the pixels located toward the cell perimeter and therefore an increase in Rac1 activity. Moreover, COS7 cell were transfected with (RBD-Citrine)-1L-(ECFP-RhoA) before and after LPA stimulation, which activates RhoA promoting the binding with the Rhotekin fragment. Upon activation, the distance and orientation between the ECFP and Citrine is altered such that the FRET efficiency of the biosensor is enhanced. The phasor plot showed a decrease of the donor lifetime due to the increase of the FRET process with time after LPA addition. The FLIM images show an incremental increase in the number of molecules undergoing FRET in the pixels at the leading edge and within the back protrusions of the cell, which agrees to the spatially distribution of RhoA activity upon cell migration, as reported in literature [97][98].

In recent works, the phasor approach was also applied to study the specific protein-protein interaction of sodium-dependent phosphate (Na/P_i) transporters, involved in the renal reabsorption of P_i, with the PDZ protein sodium-hydrogen exchange-regulating factor 1 (NHERF-1) and 3 (NHERF-3 or PDZK1), by using FRET. The phasor plots of the OK cells showed the

FRET interactions of the pairs NaP_i/ PDZK1 and NaP_i/ NHERF-1. In particular, the interaction of two different Na/P_i transporters NaPi-2a and NaPi-2c (donors) with the NHERF family proteins (acceptors) changed depending on different content of Pi. In response to low Pi concentrations, increased fractions of NaP_i-2a and NaP_i-2c are found in a bound state with NHERF-1 and PDZK1, respectively. These results supporting a more important role for PDZK1 in the adaptation to low Pi of NaP_i-2c. The depletion of PDZK1 expression in the knock-out mouse model confirmed the direct interaction between NaP_i-2c and PDZK1, which seems to play an important role in the physiological regulation of NaPi-2c [99]. The following FLIM-FRET studies with the phasor approach in CACO-2_{BBE} cells confirmed interaction of NaPi-2b with NHERF1 [100].

Fluorescence lifetime imaging microscopy (FLIM) can be also considered a label-free method, which uses the endogenous fluorescence biomarkers in biological samples. The combination with the phasor approach can be a powerful strategy for the interpretation of intrinsic fluorescence signal from living cells or tissues. The biological tissues are characterized of intrinsic fluorophores, such as collagen, retinol, retinoic acid, porphyrin, flavins, and free and bound NADH, which can reveal different metabolic states of cells during differentiation, to sense small changes in the redox state of cells, and may identify symmetric and asymmetric divisions and predict cell fate. A recent work exploited the phasor analysis to detect multiple tissue components by cluster analysis of the FLIM images from seminiferous tubules of a mice testis Oct4 GFP transgene, which expressed GFP in undifferentiated germ cells. The phasor location of every molecular species, such as collagen, free and bound NADH, FAD, retinol, retinoic acid, and porphyrin, was determined by their fluorescence lifetime. The phasor plot was primarily utilized as a fingerprint of endogenous fluorophores, as a guide to identify them in mice and, subsequently, in C. elegans germ lines. In mice germ line, the measurements of the relative concentration of GFP with respect to the average autofluorescence showed different states of differentiation of the germ cells within the tissue. In C. elegans germ line, the decrease of FAD concentration and an increase in the ratio of bound/free

NADH reflected a progression from undifferentiated stem cells to early differentiation [101]. Many works applied the phasor approach to FLIM to the study of endogenous fluorescent species in biological samples. For instance, a recent work showed the study of NADH expression in the perigonadal WAT of female mouse and in HeLa cells treated with oleic acid, to detect oxidative stress in biological systems [102]. In an interesting work, the relative amount of bound and free forms of NADH in the cytoplasm and in the nucleus have been analyzed in the phasor plot to follow the differentiation of live myoblast cells. The phasor approach can be an interesting tool for label-free investigation, providing important insight into the signaling pathways and regulatory networks, which are involved in cell differentiation and in cellular metabolic states [103].

The FLIM and phasor plot analysis can be also used to the study of the lifetime variations of the so-called environmental sensitive dyes. These probes are sensitive to the alteration of physical properties, such as pH, pressure, viscosity, ions concentrations, polarity, electric potential and temperature, providing an information about the local environment around the probes.

A recent study on rabbit erythrocytes investigated on the variations of Ca2+ concentrations after the addition of alpha-hemolysin (HlyA), which is an important virulence factor in E. coli extra-intestinal infections. In High concentrations, this toxin cause the lysis of several cells of different species, whereas, at low concentrations, it induces the production of cytokines and apoptosis. It has been reported that many of the subcytolytic effects were triggered by the increase of intracellular calcium. The results showed an average increase in internal Ca^{+2} concentration in the erythrocytes after interaction with HlyA and before hemolysis occurs. The phasor analysis of the calcium concentration of single erythrocytes depends on the fluorescent dye, which show a different lifetime values depending on whether it is free or bound to Ca^{+2}. Ca^{+2} concentrations were monitored before after addition of HlyA for each erythrocyte [94].

Many interesting works used polarity-sensitive dyes that vary their fluorescence properties according to their lipid environments. The

fluorescence properties of the environmental sensitive membrane dyes are, for example, dependent on the their local solvent polarity, which are affected by the local molecular environment and investigate membrane packing and ordered lipid phases in model membranes and living cells. One of the most common fluorophores for imaging lipid domains is Laurdan (6-lauryl-2-dimethylamino-naphthalene), a derivate of Prodan, a polarity-sensitive dye created by Weber and Farris in 1979. Laurdan senses the presence of water in the lipid bilayer of the cellular membrane, providing information about water penetration, a property related to membrane fluidity, which affects Laurdan's fluorescent emission properties [104][105]. When originally used in model membranes, it was shown that Laurdan distinguishes membrane lateral packing in model bilayers according to at least two separate classes: solid-ordered and liquid-disordered. Golfetto et al. utilized the phasor analysis to study the lifetime of each channel, resolving two different trajectories given by polarity variations and several cholesterol contents in NIH3T3 cells. This spectrally resolved approach to FLIM detection of Laurdan demonstrated an increasing dipolar relaxation effect caused by rotating water molecules in the membrane and the polarity of the environment changes the Laurdan lifetime. Based on these observations, Laurdan probe, when combined with spectrally resolved detection and the phasor FLIM approach, can be used as a biosensor for cellular membranes to detect and distinguish membrane fluidity linked to cholesterol content [106].

Another fluorescent-sensitive dye often used to probe membrane order is the styryl di-4-ANEPPDHQ dye, which was designed as a voltage-sensitive dye to monitor electrical activity in biological samples but can also be used to differentiate lipid phases in cell membranes. Owen et al. used the phasor method to distinguish ordered and disordered phase lifetimes and, by a linear combination of liquid ordered and disordered lifetimes, quantified the membrane coverage in live cell membranes stained with membrane order-sensitive dyes (Laurdan or di-4-ANEPPDHQ). From the lifetime changes that were acquired in one spectral channel, it was found that the majority of the plasma membrane is covered by the liquid-order phase [107].

2.4 The spectral phasor

The phasor representation demonstrated to be a powerful tool for the analysis of time-resolved imaging. The phasor approach may be also adopted for the analysis of the fluorescence spectrum in the image. This new global analysis tool is common known as the spectral phasor analysis. Each individual pixel of the image contains the emission spectra information, which is calculated, through Fourier transform, as a sine and cosine transforms, corresponding to the s and g coordinates in the spectral phasor. Every point in the phasor plot corresponds to the emission spectrum registered in each pixel. Each point in this scattered plot can be mapped to the original fluorescence image, providing a segmentation of the image based on the pixel with the same spectral components. The spectral images can be represented as a three dimensional data set (x,y,λ). For each harmonic frequency, the s and g coordinates of the phasor plot are given by the following expression.

$$s_{x,y}(n) = \frac{\sum_\lambda I_{x,y}(\lambda)\sin(2\pi n\lambda/L)}{\sum_\lambda I_{x,y}(\lambda)} \tag{2.26}$$

$$g_{x,y}(n) = \frac{\sum_\lambda I_{x,y}(\lambda)\cos(2\pi n\lambda/L)}{\sum_\lambda I_{x,y}(\lambda)} \tag{2.27}$$

where $I_{x,y}(\lambda)$ is the emission wavelength at a given pixel, n is the order of harmonic frequency and L is the total wavelength range (ca. 400-700 nm). As in the universal semicircle, the location of the phasor depends on the phase and the modulation ratio. The phase, which corresponds to the phasor angle in given by the spectral center of mass. The modulation, which is the distance from the origin (the phasor radius), is inversely proportional to the spectral bandwidth (Fig.2.5). As fluorescence lifetime, if different spectral species are very close in term of emission spectra, by using the higher harmonics of the fundamental frequency (First harmonic) is possible to resolve the different spectral components.

As describe above, different harmonics provide a more sensitive information about the different spectral components, changing the position of the phasors along the phasor plot due to the variation of the phase and modulation parameters.

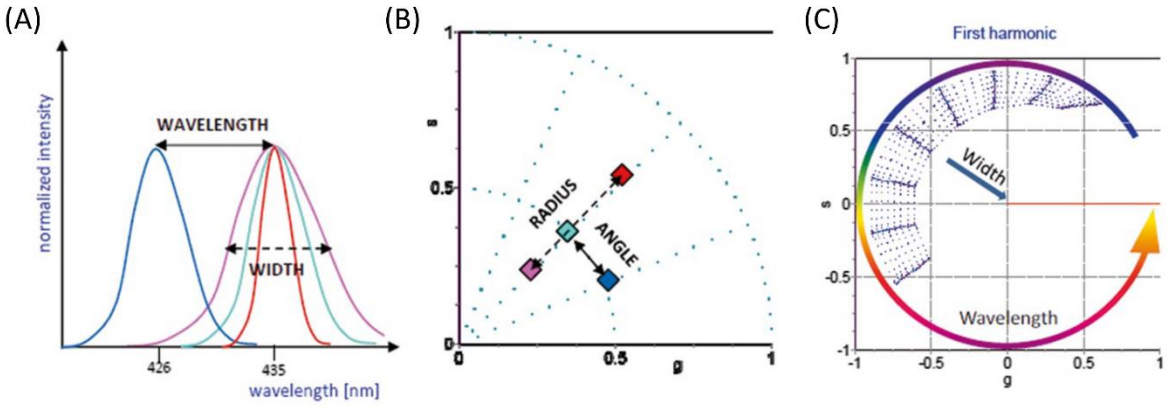

Figure 2.5. Basic principles of the spectral phasor approach. Gaussian spectra in **(A)** are transformed into phasors and represented in **(B).** Changes in the spectral center of mass are translated into different phasor angle (from blue spectrum/phasor to cyan spectrum/phasor). Changes in the spectral bandwidth correspond to different phasor radius (red, cyan and pink spectra/phasors). **(C)** Spectral phasor simulation using the first harmonic: blue pixels in the plot corresponds to Gaussian spectra with varying center of mass and bandwidth [108].

Fereidouni et al. showed the spectral phasor capabilities by using dye solutions. The aqueous fluorescent dyes are generally characterized by a single spectral component, which are identified in a precise position in the phasor plot. Different emission wavelengths correspond to different positions in the phasor plot, following a circular direction that covers the entire visible spectral range. The analyzed spectra of Coumarin 120, Rose Bengal and Fluorescein showed single-spectral components, which corresponded to the vertices of a polygon. The mixture of dyes showed a mixed phasor inside the polygon, whose position is dependent on the amount of every fractional component of each dye (Fig.2.6).

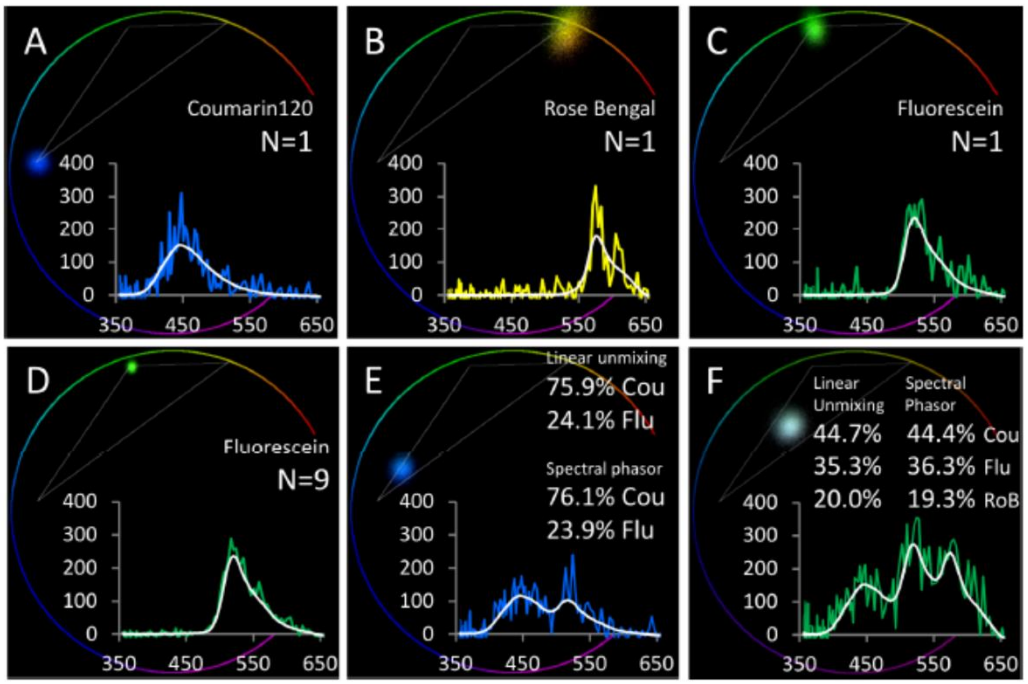

Figure 2.6. Spectral phasor analysis of solutions of organic dyes. Shown are Coumarin 120 **(A)**, Rose Bengal **(B)** and Fluorescein **(C-D)**, mixtures of Coumarin 120 and Fluorescein **(E)**, and a mixture of Coumarin 120, Fluorescein and Rose Bengal **(F).** In each phasor diagram also the average spectrum over the whole image (white line) and of a single pixel is displayed (colored line). A reference semicircle of Gaussian spectra (370-650 nm, 500 cm−1) and a grey triangle connecting the reference positions of the dyes are indicated in each phasor diagram.

The evaluation of the spectral phasor analysis on labeled BPAEC cells showed an accurate analysis of the spectral properties of each pixel of the cell, achieving a clear segmentation without bleeding through of actin, mitochondria and nucleus. The presence of bleed-through, in particular in the autofluorescence samples, may complicate the spectral analysis of the mixed phasor, due to the difficulty to reveal the position of the reference spectra of the individual components. [109].

An interesting application of the spectral phasor concerns the study of the membrane heterogeneity, by using environmental-sensitive dyes as Laurdan, sensitive to the membrane dipolar relaxation. The spectral shift of the emission wavelength, due to the reorientation of the water molecules close to Laurdan dye, is analyzed by the spectral phasor to identify the pixels of the image corresponding to different membranes in NIH3T3 and HEK293 cells. [106][110]. Laurdan properties were applied to the study of the Lamellar bodies (LBs) from A549 cells. The spectral phasor analysis of Laurdan dye

showed the evolution of the LB-like structure membrane of A549 cells in hydration and dehydration states [111]. The sensitivity of Laurdan, as others environmental sensitive probes, in combination with the spectral phasor analysis opens the possibility to comparing with accuracy cellular structures with different environmental properties.
The phasor approach has also been applied to other types of spectra obtained in non-linear microscopy. One example is polarization-resolved second harmonic generation (SHG) [112][113].

2.5 The phasor approach in fluctuation-based techniques

The fluctuation-based techniques represent the basic tool for the investigation of the diffusion of a fluorescent protein inside the cell. Fluorescence Correlation Spectroscopy (FCS) and Image Correlation Spectroscopy (ICS) are the general approach to analysis of intensity fluctuation in time and in space, respectively. Whereas ICS allows to analyze the fluorescence distribution in the entire image, the conventional single point-FCS enables to measure the distribution at each pixel of the image. Nevertheless, the single point-FCS and ICS measurements present technical limitations. In ICS, the morphological properties of the samples and the limited photostability and specificity of the probes may complicate the extraction of the average size and number of the particles in the image, making difficult the recovering the relative concentration and the shape of the correlation function of each component species. Whereas, even if single point-FCS provides information about a probe diffusion at each pixel of the image, the measurement requires a long acquisition time, resulting in photobleaching and photodamage of the cell. To overcome these limitations, it is thought to applied the phasor approach to analyze the correlation data. As explained by Ranjit and co-workers, the analysis using the phasor method provides an estimation of the diffusion coefficient at each pixel in much shorter time than the conventional FCS, transforming the correlation functions to the Fourier space into a phasor plot and generating a diffusion

map of the cell. The basic concept of this implementation is similar to the phasor approach developed for Fluorescence Lifetime Imaging Microscopy (FLIM). The autocorrelation functions $G(\tau)$ measured at each pixel of the image are transformed as the g and s coordinates in the phasor plot by the following equation:

$$s = \frac{\int_0^T \sin(2\pi t)\, G(\tau) dt}{\int_0^T G(\tau)\, dt} \tag{2.28}$$

$$g = \frac{\int_0^T \cos(2\pi t)\, G(\tau) dt}{\int_0^T G(\tau)\, dt} \tag{2.29}$$

where each point in the phasor plot corresponds to the correlation decay, obtained after the Fourier transform [114]. By moving the cursor along the phasor is possible to detect the diffusion coefficients of the corresponded pixels of the image, generating a pixel-detailed map of the fluorophore diffusion within the cell. The phasor analysis to FCS method was tested by measuring the diffusion of GFP in DPBS, Pax-EGFP in CHOK1 cells, and hIR-GFP in CHOK1 cells [115].

In a recent work, Scipioni et al. introduced the PLICS method, which coupled the fast and fit-free phasor analysis to local ICS, i.e. an ICS analysis performed iteratively on small regions-of-interest (ROIs) of the image. This method has been applied to maps the structural information from the particles composing a heterogeneous system. PLICS was used to map the size of the particle and provide a global number of particle sorted by size. The method was validated on live HeLa cells labeled with the pH-sensitive probe pHrodo Green dextran, which selectively stains the intracellular vesicles formed after endocytosis of the dye, by measuring the heterogeneity of the vesicles. The map of size of the vesicles and the count of the number of vesicles sorted by size by PLICS resulted more robust and quantitative, in which multiple global correlation functions are correlated to different

subspecies of vesicles [116]. In a subsequent study, phasor analysis was also applied to local Raster ICS (RICS) to produce high resolution maps of the diffusion coefficient of GFP within the nucleus and the nucleolus of live cells [117].

2.6 The phasor approach in SRM

In last years, the phasor method has been extended to the super-resolution microscopy (SRM) field. In particular, Stimulated Emission Depletion (STED) microscopy has been coupled with the phasor analysis for the improvement of the spatial resolution. The phasor plot capability to separate multiple components with different spatial-temporal information allowed the possibility to identify with pixel accuracy the photons in the center of PSF, which are not affected by the depletion effect of the doughnut-shape STED beam. The first work by Lanzanò et al., explained the principle of the method, commonly known as SPLIT (Separation of Photons by Lifetime Tuning). The SPLIT method can be applied to a fluorescence multi-dimensional "image" F(**x**,k), where **x** = (x,y,z) represents the conventional spatial dimension, and k an additional dimension able to encode extra spatial information about the specimen [118]. In other words each single-fluorophore (SF) must produce a "different" fluorescent signal $f_{SF}(k,r)$ which depends by its distance r from the centre of the detection volume, r = 0, so that two fluorophores located at two different radial distances r_{in} and r_{out} will show linear independent fluorescence signals $f_{SF}(k, r_{in})$ and $f_{SF}(k, r_{out})$ (Fig.2.7).

For each pixel **x,** the fluorescence signal F(**x**,k) can be written as:

$$F(\mathbf{x},k) = F_{in}(\mathbf{x},k) + F_{out}(\mathbf{x},k) = N_{in}(\mathbf{x})\langle f_{SF}\rangle(k,r_{in}) + N_{out}(\mathbf{x})\langle f_{SF}\rangle(k,r_{out}) \quad (2.30)$$

with: $N_{in}(\mathbf{x}) = \sum_k F_{in}(\mathbf{x},k)$ and $N_{out}(\mathbf{x}) = \sum_k F_{out}(\mathbf{x},k)$ the total fluorescent photons, or more in general the strengths, for the inner and outer signal; $\langle\text{-}\rangle$ the operator denoting the function normalization. It is clear that if $\langle f_{SF}\rangle(k,r_{in})$ and $\langle f_{SF}\rangle(k,r_{out})$ are known, the separation between the inner and the outer

photons $N_{in}(\mathbf{x})$ and $N_{out}(\mathbf{x})$ can be obtained by fitting the signal $F(\mathbf{x},k)$. A robust, fitting-free, and fast method to obtain the same "photons" separation can be obtained by using the phasor representation $\mathbf{P}(\mathbf{x}) = (g(\mathbf{x}), s(\mathbf{x}))$ of the signal $F(\mathbf{x},k)$. In particular, we calculate the Fourier transform (FT) along the dimension k of $F(\mathbf{x},k)$ to obtain its phasor representation. Thanks to the linear decomposition of $F(\mathbf{x},k)$, the phasor $\mathbf{P}(\mathbf{x})$ will be the vectorial superposition of the individual phasors $\mathbf{P}_{in} = (g_{in}, s_{in})$ and $\mathbf{P}_{out} = (g_{out}, s_{out})$ associated to $\langle f_{SF}\rangle(k, r_{in})$ and $\langle f_{SF}\rangle(k, r_{out})$

$$\mathbf{P}(\mathbf{x}) = \big(N_{in}(\mathbf{x})/N(\mathbf{x})\big)\mathbf{P}_{in} + \big(N_{out}(\mathbf{x})/N(\mathbf{x})\big)\mathbf{P}_{out} = w_{in}(\mathbf{x})\mathbf{P}_{in} + w_{out}(\mathbf{x})\mathbf{P}_{out}. \quad (2.31)$$

Thus, for every pixel, and for a given pair of $\mathbf{P}_{in}$ and $\mathbf{P}_{out}$ (the same for each pixel and previously obtained by choosing appropriate value of r_{in} and r_{out}) it is possible to obtain the value of the fractions $w_{in}(\mathbf{x})$ and $w_{out}(\mathbf{x})$. We can set $w_{in}(\mathbf{x})+w_{out}(\mathbf{x})=1$, and Equation (2.31) can be rewritten as:

$$\mathbf{P}(\mathbf{x}) = w_{in}(\mathbf{x})\mathbf{P}_{in} + (1 - w_{in}(\mathbf{x}))\mathbf{P}_{out}. \quad (2.32)$$

From which:

$$w_{in}(\mathbf{x}) = |\mathbf{P}(\mathbf{x}) - \mathbf{P}_{out}|/|\mathbf{P}_{in} - \mathbf{P}_{out}|. \quad (2.33)$$

Finally, the high-resolution SPLIT-STED image $F_{SPLIT}(\mathbf{x})$ is given by:

$$F_{SPLIT}(\mathbf{x}) = \sum_k F_{in}(\mathbf{x}, k) = w_{in}(\mathbf{x}) \sum_k F(\mathbf{x}, k) = w_{in}(\mathbf{x})N(\mathbf{x}) \quad (2.34)$$

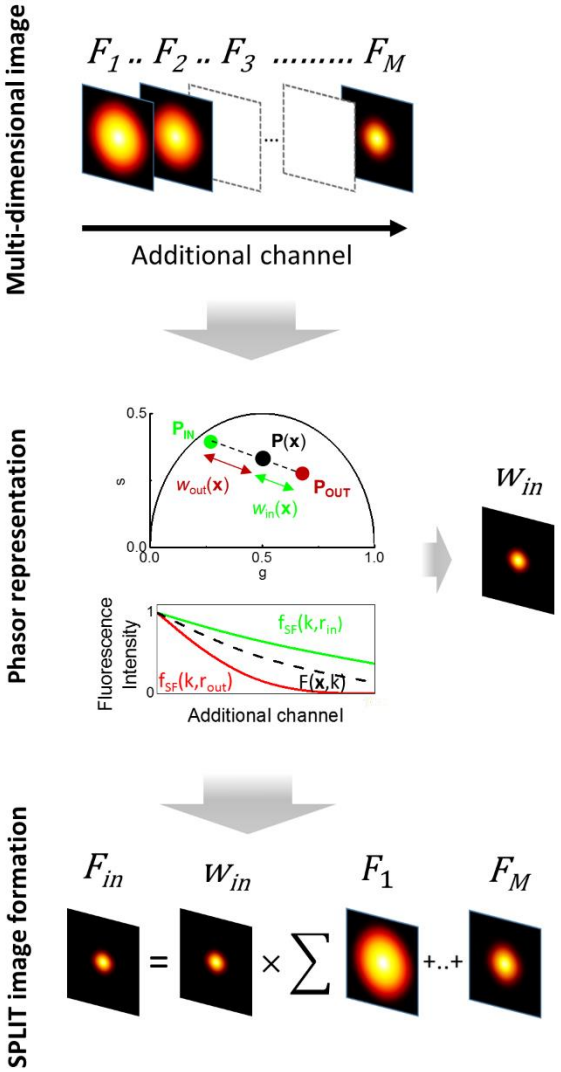

Figure 2.7. Schematic of the formation of the final SPLIT image. The SPLIT image represents the product of the fraction $w_{IN}(x,y)$ extracted by the phasor plot along the additional channel (i.e. lifetime gradient) with the images of the stack $F_{1\text{-}n}(x,y)$. The SPLIT image is generated from the integration of a single or total images of the stack to the fraction $w_{IN}(x,y)$.

In CW-STED, this additional channel is the nanosecond fluorescence lifetime. In CW-STED, the lifetime of the fluorophores in the center of the point spread function (PSF) is longer than the lifetime of those located in the periphery of the PSF [73][76]. Within the confocal-PSF, by superimposition of the continuous wave (CW)-STED beam and excitation beam, the fluorescence decay rates of the fluorophores increase in the peripheral position, where the depletion effect occurs. Fluorescence lifetime is measured at each pixel and the temporal information is decoded by using the phasor

approach. The different fluorescence decays recorded with TCSPC module are distinguished in 2 components as two vectors in the phasor plot. The phasor generated by the analysis corresponds to a multi-exponential lifetime species $P = (s, g)$, which is the linear combination of the vectors $P_{IN} = (g_{IN}, s_{IN})$ and $P_{OUT} = (g_{OUT}, s_{OUT})$, associated with the two components. In addition, the phasor analysis can reveal a third component corresponding to the uncorrelated background $P_{BKGD} = (g_{BKGD}, s_{BKGD})$. In this case, following the rules of the phasors, the phasor P will lay in the triangle with the vertices P_{IN}, P_{OUT} and P_{BKGD}. In a pulsed excitation, CW–STED microscopy experiment the fluorescence decay of a single-fluorophore as a function of the position r reads

$$f_{SF}(t, r) = I_{exc}(r)\exp\left(-t\left(k_{fl} + I_{STED}(r)\sigma_{STED}\right)\right), \qquad (2.35)$$

with: I_{exc}(r) and I_{STED}(r) the co-aligned excitation and stimulated emission radial focal intensity distribution (the center of the Gaussian excitation profile is co-aligned with the "zero–intensity" point of the doughnut-shaped stimulated emission profile), respectively; $k_{\text{fl}} = 1/\tau_{\text{fl}}$ the rate of spontaneous emission of the fluorophore (τ_{fl}, the natural fluorescence lifetime of the fluorophore); σ_{STED} the stimulated emission cross-section of the fluorophore. In essence, since I_{STED}(r) decreases in proximity of the center (r = 0), the closer the fluorophore is to the center of the detection volume the slower is its decay. This observation is the basis for improving the resolution of STED microscopy by time-gating detection: by collecting the fluorescence signal after a fix temporal delay from the excitation events, highlights the fluorescence signal from the fluorophores close to the center, while discarding fluorescence from fluorophores in the periphery.

The equation 2.34 shows that the improvement of spatial resolution of the SPLIT image is provided by the fraction $w_{in}(x,y)$ extracted by phasor analysis of the data along the additional channel k. It also shows that the signal-to-noise ratio (SNR) of the SPLIT image will be affected by any additional noise introduced by $w_{in}(x,y)$. In fact, $w_{in}(x,y)$ is calculated by decomposition of the phasor P(x,y) which, in turn, is affected by an experimental error dependent

on the total number of photons detected at a given pixel. The SPLIT method is considered a powerful tool to enhance the spatial resolution, decoding the temporal dynamics information encoded in each pixel of the image, without the necessity to increase the STED power, which may generate photodamage and photobleaching of the sample. Notably, the phasor analysis allows to discriminate the pixels of the images correlated with the STED-induced background, increasing the signal-to-noise (SNR) ratio. In this work, the applicability of the method was tested on imaging of microtubules of fixed HeLa cells, labeled with Alexa Fluor 488 and Oregon Green 488 [76]. The SPLIT method has been also extended to pulsed-STED (pSTED) implementations. The pSTED-SPLIT technique improves the spatial resolution of a time-resolved pSTED-PSF, as the CW-STED microscope, facilitating the integration of SPLIT method to any time-resolved STED microscope [119].

Notably, the phasor analysis is able to decode the spatial information encoded in an additional channel, not necessarily related to the fluorescence lifetime. This property further extends the applicability of the SPLIT method to all STED microscopes, even those not provided of pulsed excitation and dedicated hardware for lifetime detection in the nanosecond temporal scale.

In another implementation of SPLIT, the additional channel for SPLIT was represented by the depletion power, demonstrating that SPLIT could be applied to stacks of n STED images acquired sequentially at increasing depletion power. In this specific implementation, a stack of n = 8 images was generated by linearly increasing the value of STED power P_{STED} from zero (P_{STED}=0) up to a maximum value (P_{STED}=P_{max}), generating multiple STED-PSFs. Here, the STED architecture can collect a sequence of STED images at different STED beam power values. In the gated CW-STED microscope, the fluorescence signal of a single-fluorophore as a function of the position r can be expressed as [73]:

$$f_{SF}(P_{STED}, r) \cong I_{exc}(r)(k_{fl}/(k_{fl} + P_{STED}a(r)\sigma_{STED}))\exp(-T_g(k_{fl} + \\ + P_{STED}a(r)\sigma_{STED})) \tag{2.36}$$

with: *a(r)* the function that relates P_{STED} to the STED intensity, $I_{STED}(r) = P_{STED}$ *a(r)*; T_g the time gating value. Note that for large values of T_g, Equation (2) can be approximated by an exponential decay function, as described in Sarmento et al. Nat. Comm., 2018. The resulting phasor corresponding to the center of the PSF lies on the phasor coordinates (0,0), while the phasor corresponding to the periphery spreads away from the origin. By using the SPLIT algorithm, the improved resolution image is extrapolated by splitting the "wanted" fluorescence emission from the pixels in the center of the PSF from the modulated emission originating from the periphery. A recent work with a commercial gCW-STED setup showed the capability of the method to visualize replication and transcription foci in intact nuclei of eukaryotic cells with an improved resolution [120].

Notably, for both SPLIT-STED implementations, the fluorescent signal f_{SF} is non-linear with respect to the stimulated emission intensity $I_{STED.}$ Thanks to this non-linearity, two fluorophores located at two different radial distances r_{in} and r_{out} will show linear independent fluorescence signals $f_{SF}(k, r_{in})$ and $f_{SF}(k, r_{out})$. Which is exactly a mandatory ingredient of the SPLIT method. In other words, the non-linearity introduced by the stimulated emission process, together with the doughnut-shaped STED beam intensity profile allows introducing a sub-diffraction spatial signature in the fluorescence signal.

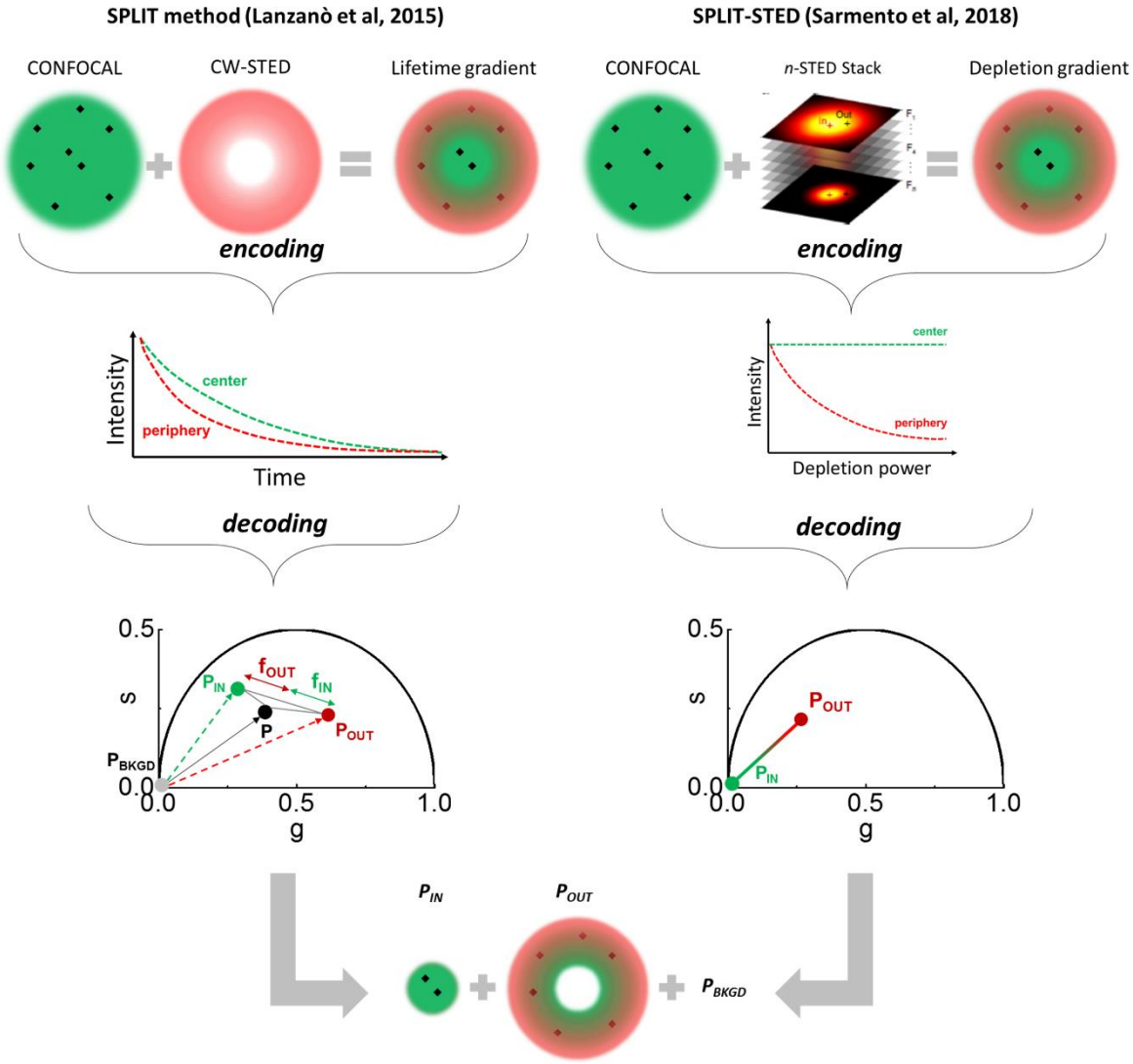

Figure 2.8. Phasor analysis in STED microscopy. Schematic representation of the SPLIT and the SPLIT-STED methods, based on the same basic principle. The goal is to separate the photons emitted from the center of the confocal-PSF (green), from those emitted from the periphery (red), in the overlapping region of the excitation and depletion beams. The encoding information is provided by lifetime gradient (Lanzano et al, 2015) and depletion gradient (Sarmento et al, 2018). The decoding is obtained by the phasor analysis expressing the phasor of the central region (P_{IN}) and the phasor of the peripheral region (P_{OUT}). With the SPLIT algorithm, the SPLIT image is generated by the photons emitted from the pixels in the center of the PSF (P_{IN}), improving the spatial resolution.

Chapter 3

3.Chromatin organization investigated at the nanoscale by FLIM-FRET

3.1 State of the art

Förster resonance energy transfer (FRET) can be considered an interesting strategy to get information on the nanoscale chromatin environment, without the help of SRM. As explained in the introduction, FRET is a process that occurs between an excited donor and an acceptor molecule when the two fluorophores are within ~10 nm distance [121]. For this reason, FRET is considered as a 'spectroscopic nanoruler' and it is a powerful tool for the detection of protein-protein interactions in live cells [100][63][99]. Even if FRET imaging is usually performed with optical systems limited by diffraction, the FRET phenomenon detects changes in the distribution of nanometer-sized fluorophores and can be used to indirectly infer properties of the nanoscale chromatin architecture [117][33][34][35][36].

FRET can be eventually coupled with Fluorescence Lifetime Imaging Microscopy (FLIM), which has been used to detect variations in the local environment around a fluorescent probe and relate them to the chromatin condensation state [122][123][124][125]. The sensitivity to nanometer distances makes FRET especially useful in the investigation of chromatin environment. Originally, Lleres and coworkers developed a quantitative FRET approach to assay nanoscale chromatin compaction [126]. Through FLIM-

based detection of FRET between stably incorporated GFP-H2B and mCherry-H2B histones, they quantified the nanoscale proximity between nucleosomes. This FRET assay has been used to reveal distinct regions and quantitatively discriminate different levels of nanoscale chromatin compaction in live HeLa cells [126] and in living C. Elegans as a model system [127]. More recently, Lou et al. applied the same FRET assay to measure chromatin organization in live cells in combination with the phasor analysis of FLIM[95][128]. Coupling the phasor FLIM-FRET technique with laser micro-irradiation allowed to identify the DNA damage response (DDR)-dependent chromatin architectural changes that occur in response to DNA double-strand breaks (DSBs) [128]. In all these works, it has been demonstrated that FRET can be a powerful tool to map nanoscale chromatin compaction in vivo.

However, there are some pitfalls in the mentioned chromatin compaction FRET assays. First, the applicability of the method may be limited by the induction of transient or stable fluorescent protein expression, which might be challenging in some specific cell lines. Besides, the transfection protocol, in general, requires a longer time to prepare samples for inducing a transient expression of the proteins, or the establishment of a stable cell line. Furthermore, in contrast to FRET detection of protein-protein interactions, in which the stoichiometry of the putative protein clusters is often predictable, in the chromatin FRET assay, the effective number of donors and acceptors involved in the FRET interaction is not well defined. An additional variation of FRET may be generated by a high variability in the number of donor and acceptor molecules, not necessarily linked to changes in the average donor-acceptor distance [129][130][131][132][133] (Fig.3.1). In this case, the measured FRET level should be corrected for the relative acceptor donor abundance.

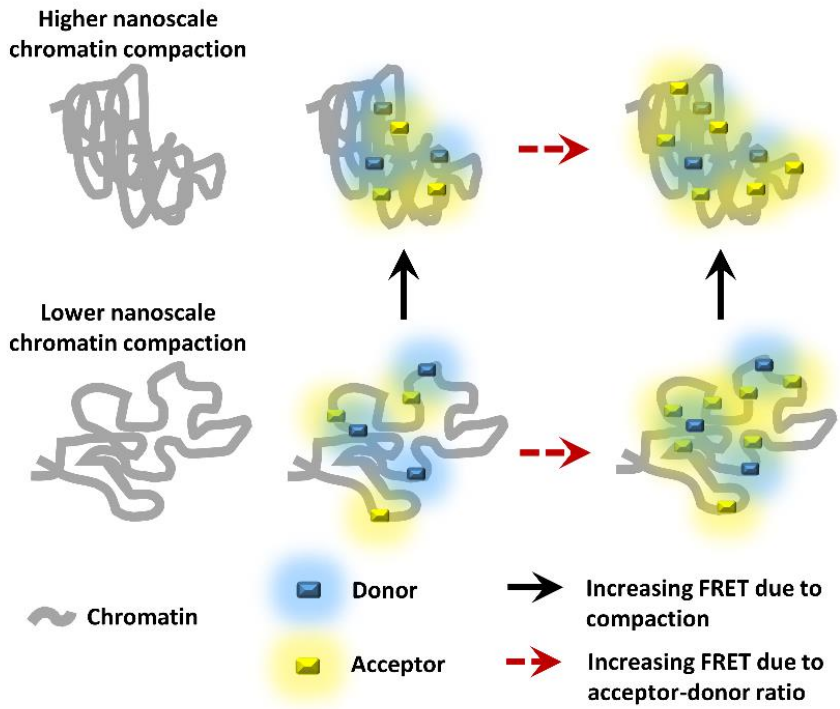

Figure 3.1. Schematic representation of the FRET assay for chromatin nanoscale compaction. Donor (cyan) and acceptor (yellow) molecules are bound to nuclear chromatin (grey). Variations in the measured FRET level can be due both to changes in chromatin density (black solid arrow) and/or to changes in relative acceptor-to-donor abundance (red dashed arrow).

3.2 Main goal of the project

The main aim of this project is the introduction of a novel FRET assay that provides a FRET level independent of the acceptor-donor ratio. I explored the possibility of using the FRET occurring between two conventional DNA-binding dyes with overlapping emission/excitation spectra to measure chromatin compaction in live cells at the nanoscale level, rather than between fluorescently labeled histones. In this project, I made use of a FRET pair represented by Hoechst 33342 and Syto 13 as the donor and acceptor molecules, respectively. As shown in Fig.3.2, Hoechst 33342 emits in the blue spectrum with an emission peak at 460 nm, whereas Syto 13 shows the emission peak around 500 nm in the green range. The spectral overlap between the donor emission and acceptor excitation spectra makes Hoechst 33342 and Syto 13 suitable dyes for the FRET process. Hoechst 33342 is a

bis-benzimidazole dye binding to the minor groove of DNA with a preference for sequences rich in adenine and thymine (AT-rich sequence specificity). Syto 13 exhibits affinities for both DNA and RNA, labeling DNA in the nucleus and mitochondria and RNA in the cytoplasm and nucleoli [134].

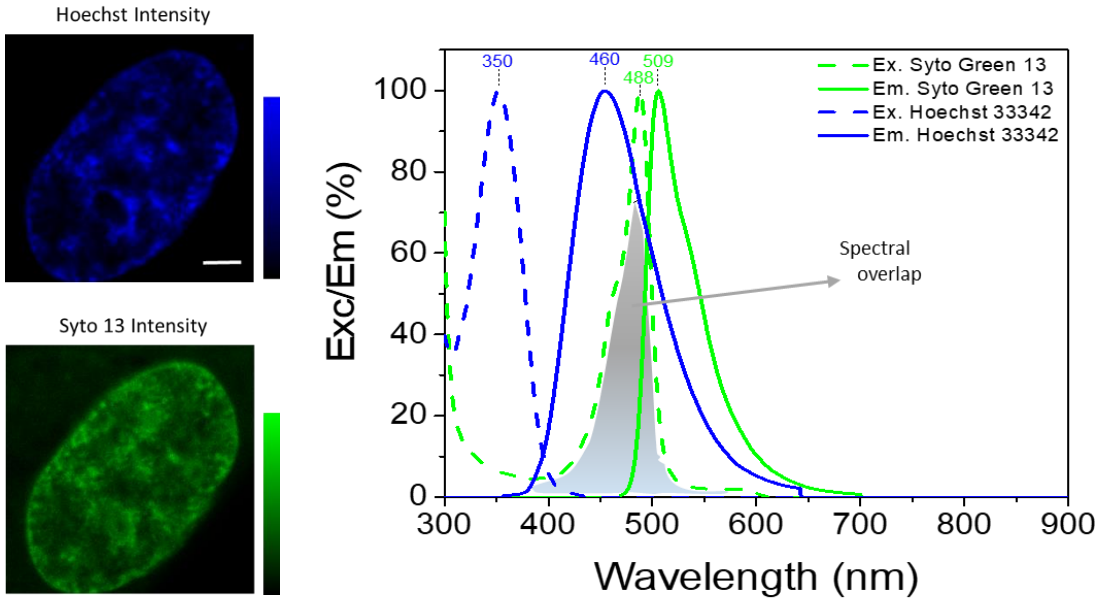

Figure 3.2. **Excitation and emission spectra of Hoechst 33342 and Syto Green 13** (Source: thermofisher.com). The shaded region represents the spectral overlap between Hoechst 33342 emission and Syto Green 13 absorption. Scale bar: 5μm.

As shown in Fig.3.1, I assume that a higher nanoscale chromatin compaction corresponds, on average, to a shorter distance between the fluorescent probes and, hence, an increasing FRET efficiency. On the other side, an increase of the acceptor-to-donor abundance could produce by itself an increasing FRET efficiency, not necessarily related to nanoscale distance due to chromatin compaction level.

FRET interaction between Hoechst 33342 and Syto 13 was initially measured by frequency domain-FLIM monitoring the decrease of the donor lifetime, as explained in the previous sections. FRET consists in a non-radiative process, in which the donor (Hoechst 33342) lifetime is reduced due to energy transfer to the acceptor fluorophore (Syto 13). FLIM is an advantageous technique, which provides a value of FRET efficiency without the corrections (e.g. cross-

talk between channels, estimation of the relative concentration of the fluorophores) required by intensity-based methods [135]. In FD-FLIM, the decrease in the donor lifetime induced by FRET was detected as a decrease in the value of phase measured at a given frequency (in this experiment, the fundamental harmonic at 80MHz) (Fig. 3.3a). In the phasor plot of Fig.3.3b, a cell stained with only Hoechst 33342 (Cell 1, Fig.3.3c) is compared with two cells stained with both Hoechst 33342 and Syto 13 (Cells 2 and 3, Fig.3.3d,e). The lower phase value measured in the donor-acceptor samples with respect to the donor-only sample shows the occurrence of FRET between Hoechst 33342 and Syto 13 (Fig.3.3b-e).

I noticed that the degree of staining with these two fluorophores was heterogeneous within the cells of the sample. In particular, I observed that a higher acceptor-to-donor abundance (i.e. more Syto 13 relative to Hoechst 33342) corresponded to a stronger decrease of the donor lifetime (Fig. 3.3d,e). In Fig.3.3, the average lifetime of Hoechst 33342 changed from $\tau_D \sim 2.7$ ns (donor only sample) to τ_{DA}~1.9 ns (Fig.3.3d) and $\tau_{DA} \sim 1.7$ ns (Fig.3.3e) respectively, due to the donor quenching in the proximity of Syto 13, resulting in different levels of the FRET efficiency E, defined by the expression $E = 1 - \tau_{DA}/\tau_D$ (Fig.3.3f,g).

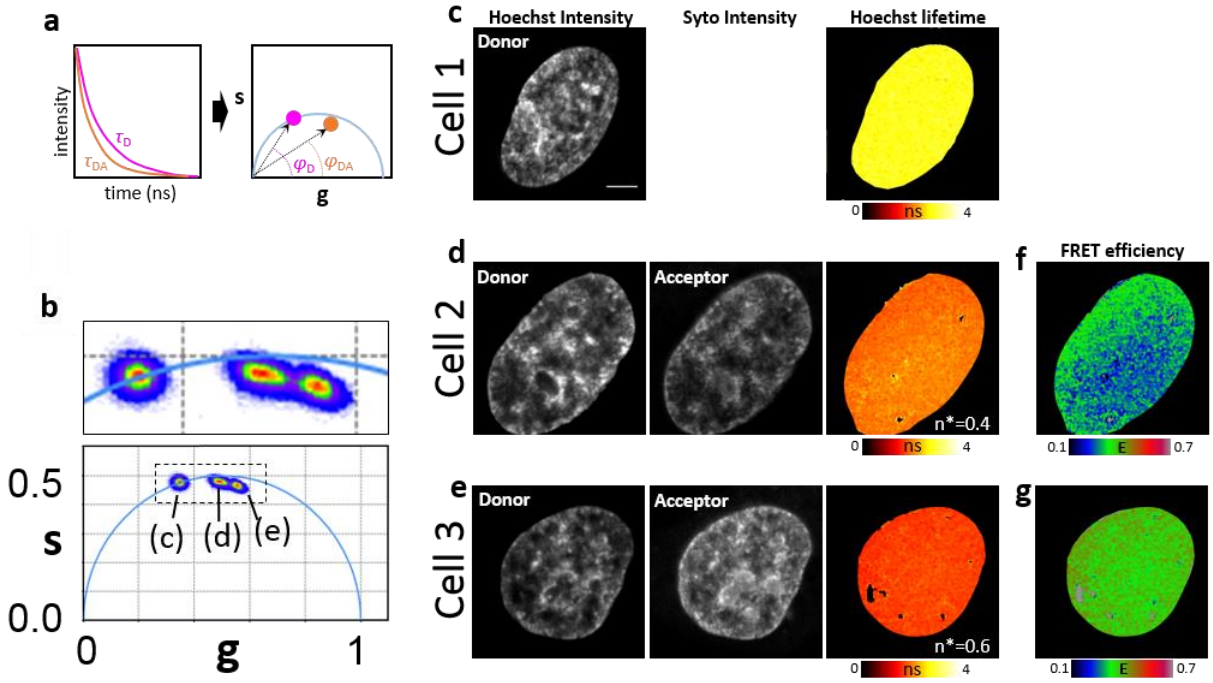

Figure 3.3. **FD-FLIM detection of FRET affected by the acceptor-donor ratio. (a)** Schematic representation of frequency domain analysis of FLIM-FRET data. The FRET-induced decrease in the donor lifetime from τ_D to τ_{DA} is detected as a decrease in the value of phase (from φ_D to φ_{DA}) measured at a given frequency. **(b)** Phasor analysis of FLIM-FRET of Hoechst 33342 and Syto 13 in live HeLa cells. The three clusters correspond to the representative samples reported in **(c-e)**. **(c)** Representative image of a cell labeled with the donor only. Shown are the intensity in the donor channel and the lifetime of the donor. **(d,e)** Representative images of two cells in the donor-acceptor sample with different level of acceptor-donor ratio. Shown are the intensity in the donor channel, the intensity in the acceptor channel and the lifetime of the donor. Indicated is the average value of acceptor-donor ratio n*. **(f,g)** Shown are the map of the FRET efficiency E. Scale bar: 5μm.

For this reason, it is important to extract a value of FRET efficiency related only to the average distance between the fluorophores but not to their relative abundance. To provide an accurate FRET level, I monitor variations of the lifetime of the donor by frequency-domain FLIM and normalize the FRET efficiency to the relative acceptor-to-donor abundance. I show that, thanks to this correction, the method provides consistent spatial maps of nanoscale chromatin compaction independently of the local donor and acceptor concentrations. I validate the method by quantification of different degrees of chromatin compaction in live interphase nuclei, distinguishing different density patterns, both in the physiological and hyperosmolar environment. As an application, I study changes in nanoscale chromatin architecture

during the DNA damage response (DDR), generated by stimulation with laser UV-microirradiation, inside nuclear-defined regions.

3.3 Materials and Methods

3.3.1 Cell Culture and Treatments

HeLa cells were cultured in a flask in Dulbecco's modified Eagle's medium (DMEM) supplemented with 10% FBS, 2 mM L-glutamine and 1% penicillin/streptomycin in a humidified incubator at 37°C with 5% CO2. Subsequently, cells were plated on a Ibidì µ-slide 8-well chamber and let grow overnight. Cells were washed in Phosphate Buffer Saline (PBS 1X, pH 7.4; Thermofisher Scientific) and stained with 2µM Hoechst 33342 (Thermofisher Scientific) (donor only sample) or with 2µM Hoechst 33342 and 2µM Syto 13 (Thermofisher Scientific) (donor-acceptor sample) and left incubating for 25 min at 37°C. For FRET measurements, cells were observed without any washing step, i.e., leaving the fluorophore diluted in DMEM.

For hyperosmolar experiment, HeLa cells were washed in PBS 1X and hyper-compacted chromatin (HCC) formation was induced by incubating HeLa cells in a hyper-osmolar medium at osmolarities ~570 mOsm for 25min at 37°C with 5% CO2. Afterwards cells were stained with 2µM Hoechst 33342 (donor only) or with 2µM Hoechst 33342 and and 2µM Syto 13 (donor-acceptor sample) and left incubating for 20 min at 37°C in hyperosmolar solution. As a standard protocol, 1 ml 20 X PBS (2.8 M NaCl, 54 mM KCl, 130 mM Na2HPO4, 30 mM KH2PO4 in H2O, pH adjusted with HCl to 7.4) was diluted with 19 ml standard culturing medium (290 mOsm) to yield an osmolarity of 570 mOsm [136].

For monitoring the DNA damage response, cells were transiently transfected with PARP1-Chromobody-TagRFP (Chromotek), according to QIAGEN Effectene protocol and imaged 24 h after transfection.

3.3.2 Laser microirradiation

DNA damage was induced by laser micro-irradiation on cells pre-sensitized by Hoechst 33342. I used the 405 nm-laser beam of the Nikon's A1R MP confocal and multiphoton microscope. The laser power was set at 80% and the laser beam was focused on a selected region of interest (ROI) of the nucleus (15 μm × 6 μm) for a total micro-irradiation time of 40 s. For monitoring the response of PARP-1 to DNA damage induction, a 65 s time-lapse movie was recorded (256 × 256 pixels, 9.5 μs/pixel, 634 frames). FLIM-FRET microscopy was performed in parallel using the microscope and acquisition settings described above. FLIM-FRET acquisitions were recorded immediately after laser micro-irradiation.

For cells analyzed by immunostaining, the induction of DNA damage was set with a laser power at 100%, on a selected ROI of size 3 μm × 3 μm, for a total micro-irradiation time of 20 s. Micro-irradiated cells were fixed within ~5 min after micro-irradiation.

3.3.3 Cell fixation and immunostaining

Cells were fixed with 4% formaldehyde in PBS 1× for 15 min and washed several times with PBS 1×. After fixation, HeLa cells were permeabilized and incubated in blocking buffer solution (5% w/v bovine serum albumin (BSA), 0.1% (v/v) Triton X-100 in PBS) for 1 hour at room temperature.

For PARP-1 detection, cells were incubated overnight at 4 °C with the primary antibody mouse anti-PARP1 (sc-8007; Santa Cruz Biotechnology), in blocking buffer (1/50 dilution), followed by several washing steps. Cells were then incubated with the secondary antibody Alexa488- conjugated anti-mouse (A28175; Thermofisher Scientific) in PBS (1/600 dilution), for 1 hour at room temperature, and washed with PBS.

Cells were stained with TO-PRO-3 Iodide (T3605; Thermofisher Scientific) (dilution 1:2000) in PBS and left incubating for 25 min at room temperature and subsequently were washed several times with ultrapure water.

Confocal images of immunostained samples were acquired on a Leica TCS SP5 microscope, using a HCX PL APO ×100 100/1.40/0.70 oil immersion objective lens (Leica Microsystems, Mannheim, Germany). Excitation source was provided by a white laser at the desired wavelength starting from 470 nm. Alexa488 was excited at 488 nm and its fluorescence emission detected at 500–560 nm. TO-PRO-3 Iodide excitation was performed at 633 nm and its emission collected in the band 645-710.

3.3.4 Experimental setup

FLIM-FRET data were acquired with Nikon's A1R MP confocal and multiphoton microscope, coupled to an ISS A320 frequency-domain FastFLIM box to acquire the lifetime data. A Nikon Plan Apo VC 100X Oil DIC N2 objective, NA 1.45, was used for all the measurements. The donor fluorophore was excited at 405 nm. This wavelength caused also direct excitation of the acceptor. The fluorescence signal was split between two hybrid photodetectors, with the following emission band-pass filters in front of each: 450/50 (Hoechst 33342) and 585/40 (Syto 13), respectively. I simultaneously acquired intensity and lifetime data by scanning with a 80 MHz pulsed laser beam (405 nm, PDL 800-D, PicoQuant). The frame size was set to 512×512 pixels, with a pixel size of ~0.05 μm. The scanning pixel-dwell time was set at 12.1 μs/pixel. Each FLIM image was obtained by integrating the signal of 20 frames corresponding to an acquisition time of ~1 min.

The FLIM data acquisition was managed by the ISS VistaVision software. In frequency domain FLIM, the lifetime is determined from the phase delay and the de-modulation of the fluorescence emission with respect to a modulated excitation signal [137]. For each pixel, the FLIM system records a value of phase (ϕ) and modulation (M) at multiple frequencies with respect to the excitation signal. All the data were analyzed at the frequency of 80 MHz. The raw FLIM data were visualized in the phasor plot where $g=M\cos(\phi)$ and $s=M\sin(\phi)$ [95].

Figure 3.4. ISS-FastFLIM implementation

Calibration of the system was performed by measuring Fluorescein in 0.1M NaOH (pH 9.0), which has a known single exponential lifetime of 4.1 ns. Before each experiment, I calibrated the donor channel using a solution of Alexa Fluor 405 (Thermofisher) which is excited at the same excitation wavelength of the donor (Hoechst 33342). I determined that Alexa Fluor 405 in DMSO has a single exponential lifetime of 3.5 ns (Fig.3.5). For each measurement, the following four images were exported for further processing on ImageJ [138]: the intensity in the donor channel $I_1(x,y)$, the intensity in the acceptor channel $I_2(x,y)$, the phasor coordinate $g(x,y)$ in the donor channel and phasor coordinates $s(x,y)$ in the donor channel.

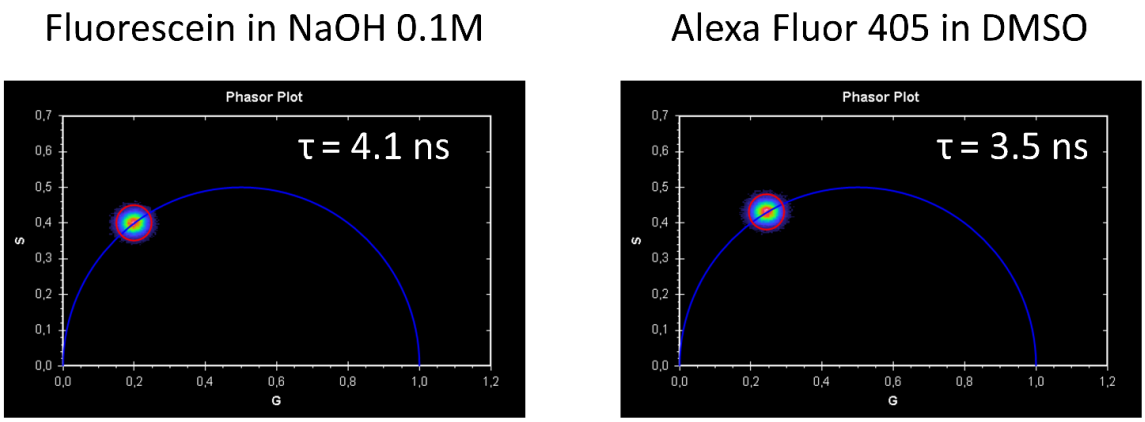

Figure 3.5. Determination of the fluorescence lifetime of Alexa 405 in DMSO. The lifetime has been measured using 405 nm excitation modulated at 80 MHz. Shown is the phasor plot of a solution of Fluorescein in NaOH 0.1M used for calibration (left) and the phasor plot of a solution of Alexa 405 in DMSO (right).

3.4 Results

The preliminary measurements of FRET detection by FD-FLIM showed the dependence of the FRET efficiency value on the relative acceptor-to-donor abundance. To obtain an accurate FRET value providing structural information about the nanoscale chromatin compaction, I implemented a FRET calculation finalized to the calculation of a FRET efficiency value linked to the average distance between the fluorescent molecules. I will show the principle of the method on simulations data generated using Matlab (Mathworks) and, subsequently, a series of image operations for FRET calculation on experimental data with ImageJ software.

3.4.1 Corrected FRET assay on simulated data

The simulated data were generated in Matlab (Mathworks). I simulated a mixture of N_D donors undergoing FRET with a variable number N_A of acceptors. The lifetime of the unquenched donor was set to the value τ_0=2.7 ns.

The FRET efficiency of a donor interacting with a single acceptor was set to the value E_0. The FRET efficiency of a donor interacting with an integer number n_A acceptors was set to the value E_n, where $E_n=1/(1+1/A_n)$, $A_n=n_A A_0$ and $A_0=E_0/(1-E_0)$ [129]. For any given value of N_A/N_D, the mixture was set in the following way: for $n_A-1<N_A/N_D<n_A$, a value of efficiency E_n was assigned to a fraction of donors equal to N_A/N_D-n_A, whereas a value of efficiency E_{n-1} was assigned to all the other donors. The temporal decay corresponding to this mixture was then analyzed in frequency domain via a Fast Fourier Transform algorithm. The phase value φ corresponding at the frequency f=80 MHz was used to calculate a value of phase lifetime

$\tau_\varphi = \tan\varphi/(2\pi f)$. Finally, the efficiency E was calculated as $E = 1 - \tau_\varphi/\tau_0$ and the value of A was calculated as $A = E/(1-E)$.

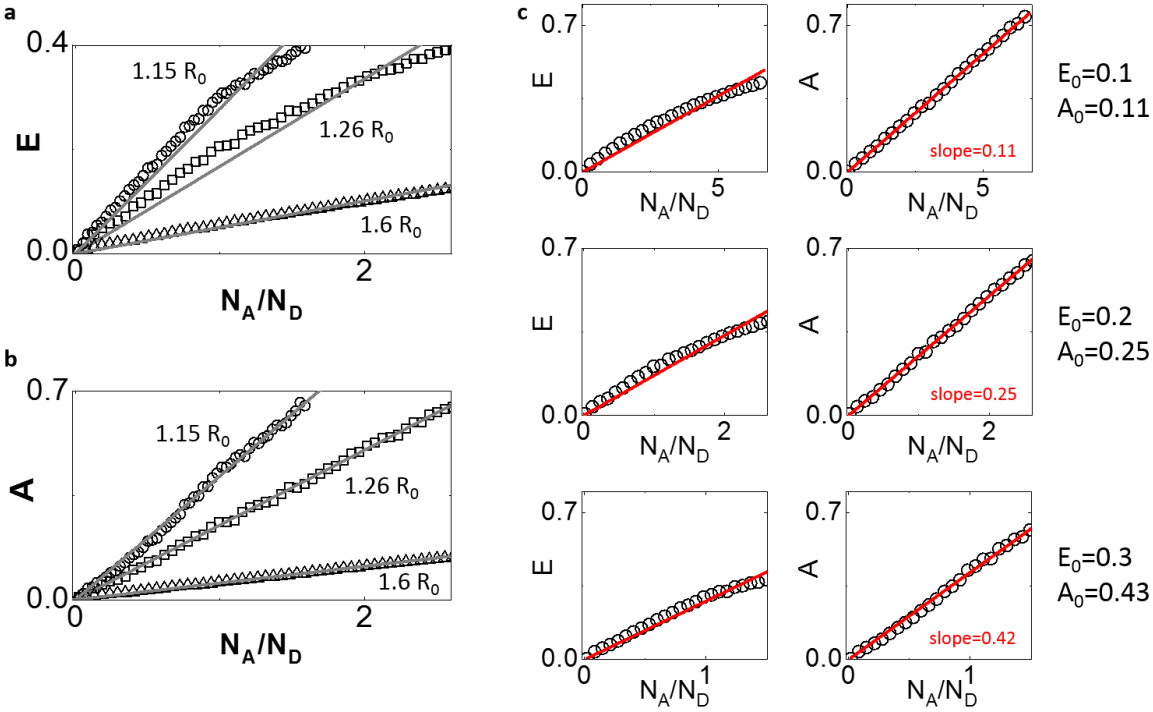

Figure 3.6. Calculation of FRET efficiency E and FRET level A on simulated data. **(a,b)** Plot of the FRET efficiency E and of the FRET level A versus the acceptor-donor ratio for simulated data. Numbers indicate the simulated acceptor-donor distance expressed in Forster radius (R_0) units. Solid lines are linear fits of the data through the origin. **(c)** Data represent the FRET measured from a mixture of N_D donors undergoing FRET with a variable number N_A of acceptors. Each simulation has been obtained by fixing the value of E_0, corresponding to the FRET efficiency of a donor interacting with a single acceptor, and by varying the acceptor donor ratio N_A/N_D. The solid red lines are linear fit of the data through the origin.

3.4.2 Corrected FRET assay on experimental data

In the experimental data, the corrected FRET value was calculated by a series of image operations, implemented on ImageJ. For each measurement, the image of the phase lifetime $\tau(x,y)$ was obtained from the phasor images $g(x,y)$ and $s(x,y)$ using the formula:

$$\tau(x,y) = \frac{1}{2\pi f}\frac{s(x,y)}{g(x,y)} \tag{3.1}$$

where f=80 MHz. To quantify the relative acceptor-to-donor abundance I used the ratio of the fluorescence intensities emitted by the two fluorophores, I_A and I_D, which are proportional to the concentrations of the two fluorophores (N_A and N_D) and their quantum yields.

First, the contribution of the donor bleed-through was removed from the acceptor channel:

$$I_A(x,y) = I_2(x,y) - k_{BT}I_1(x,y) \tag{3.2}$$

where the constant k_{BT} was determined from the donor only sample as the average value of $I_2(x,y)/I_1(x,y)$ from at least 3 different cells. The corrected intensity $I_A(x,y)$ represents all the fluorescence emission detected from Syto 13, including fluorescence resulting from direct excitation of Syto 13 at 405 nm and FRET signal. I will assume that the contribution of the FRET signal to $I_A(x,y)$ is negligible compared to the contribution due to direct excitation. The intensity in the donor channel was not affected by spectral cross-talk so we set $I_D(x,y)=I_1(x,y)$.

For the donor channel is $I_D(x,y)=\beta_D N_D(x,y)(\tau_{DA}(x,y)/\tau_D)$, where β_D is the brightness (counts per molecule per integration time) of the unquenched donor in the donor channel, $N_D(x,y)$ is the number of donor molecules at a given pixel and the factor τ_{DA}/τ_D takes into account the decrease of quantum yield of the donor due to FRET [139]. For the acceptor channel is $I_A(x,y)=\beta_A N_A(x,y)$, where β_A is the brightness of the acceptor in the acceptor channel and $N_A(x,y)$ is the number of acceptor molecules at a given pixel. We calculated an image of the experimental acceptor-donor ratio as:

$$n^*(x,y) = \frac{I_A(x,y)}{I_D(x,y)}\frac{\tau_{DA}(x,y)}{\tau_D} \tag{3.3}$$

The quantity $n^*(x,y)$ is proportional to the absolute value of the acceptor-donor ratio $N_A(x,y)/N_D(x,y)$:

$$n^*(x,y) = \frac{\beta_A}{\beta_D}\frac{N_A(x,y)}{N_D(x,y)} \tag{3.4}$$

As previously explained, the FRET efficiency $E(x,y)$ was obtained as:

$$E(x,y) = 1 - \frac{\tau_{DA}(x,y)}{\tau_D} = \frac{K_{transfer}}{K_{transfer} + K_{other}} \tag{3.5}$$

where $\tau_{DA}(x,y)$ is the phase lifetime image of a donor-acceptor sample and τ_D represents the phase lifetime of the unquenched donor. The lifetime of the unquenched donor was determined, in each experiment, from lifetime images of a donor only sample prepared in the same conditions of the donor-acceptor sample. The value τ_D was set as the average value obtained from at least 3 different cells. In general, the FRET efficiency $E(x,y)$ is measured, defined as the ratio of the energy transfer rate to the total donor de-excitation rate, where $K_{transfer}$ is the transfer rate and K_{other} is the sum of the rate constants of all the other de-excitation processes. The term above can be linearized as a function of n* if the expression $A(x,y)$ is used instead of E.

The FRET level $A(x,y)$ was then obtained as:

$$A(x,y) = \frac{E(x,y)}{1 - E(x,y)} = \frac{K_{transfer}}{K_{other}} \tag{3.6}$$

As shown in Fig.3.7a, the value of $n^*(x,y)$ revealed the experimental dependence of the FRET efficiency E and the FRET level A versus the experimental acceptor-to-donor ratio for all the different cells measured in one experiment. The plots in Fig.3.7a indicate that the observed variations in FRET between Hoechst 33342 and Syto 13 are related to variations in the relative acceptor-to-donor ratio naturally occurring on a given specimen. These variations were probably due to an intrinsic

variability in the internalization of the dyes into chromatin, even if the cells were stained with the same amount of the two dyes.

Finally, I used the value of $n^*(x,y)$ to normalize the FRET level $A(x,y)$ for variations of the acceptor-donor ratio and generate, at each pixel of an image, a corrected value of FRET level:

$$A_0^*(x,y) = \frac{A(x,y)}{n^*(x,y)} \tag{3.7}$$

In principle, the corrected FRET level A_0^* is a FRET parameter related only to the average distance between donors and acceptors but not to their relative abundance. Therefore, an increase in the transfer rate from an initial value will result in an increase non-linear transfer efficiency with a linear increase in E / (1 - E).

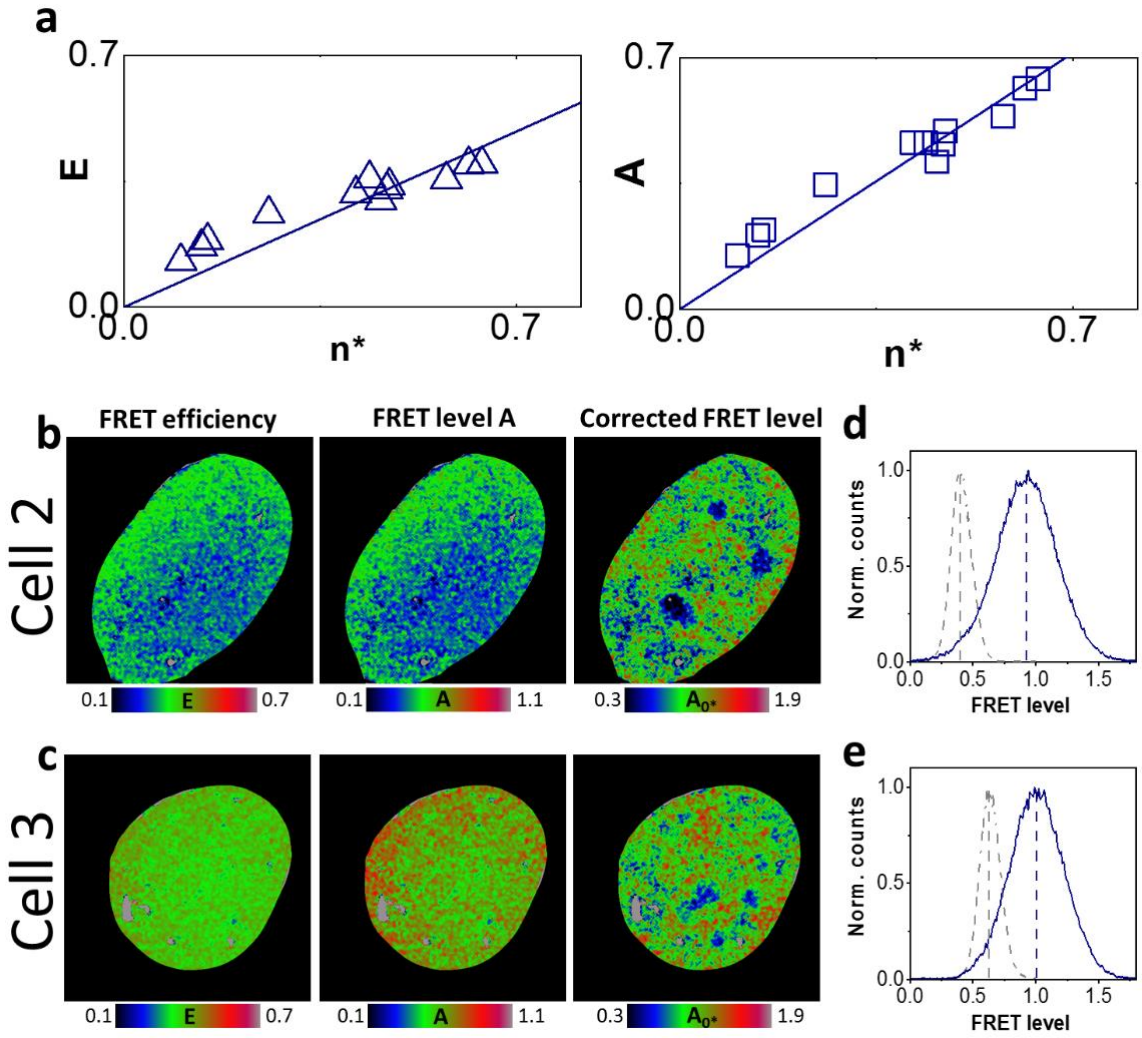

Figure 3.7. FRET assay corrected for the acceptor-donor ratio (a) Experimental values of E and A versus n*. Each point is the mean ± s.d value of E (blue triangles) and A (blue squares) for every single cell of the sample population. Solid lines are linear fits of the data through the origin. **(b,c)** FRET level before and after correction for the samples reported in **(Fig.3.3d,e).** Shown are the map of the FRET efficiency E, the map of the FRET level A and the map of the corrected FRET level A_0*. **(d,e)** Histograms of the pixel values of the FRET level before (parameter A, dashed grey) and after (parameter A_0*, solid blue) correction. The vertical dashed lines mark the position of the peaks of the FRET histograms. Scale bar: 5μm

3.4.3 Corrected FRET assay shows different nanoscale chromatin compaction

To validate this approach, we first compared the FRET level measured on chromatin regions of high and low DNA density, identified by the fluorescence intensity of Hoechst 33342 in each cell (Fig.3.8a,b). The peripheral and perinucleolar heterochromatin typically showed a higher Hoechst 33342 signal because these regions corresponded to a higher DNA density, characterized by a concentration of AT-rich sequences, for which the dye owns a preferential affinity [140]. The average FRET level A measured in the two regions, for each cell, was reported as a function of the relative acceptor-to-donor abundance n* (Fig.3.8c,e). The regions with high Hoechst signal (the heterochromatin regions) have a higher level of nanoscale compaction compared to the regions with low Hoechst signal (the euchromatin regions), as showed by the different slope of the two sets of data. Similarly, the maps of corrected FRET level A_0^* (Fig.3.8d,f) indicated that nanoscale compaction was higher in heterochromatin (A_0^*=1.09 ± 0.025, mean ±s.e.m., n = 10 cells) than in euchromatin (A_0^*=0.90 ± 0.025, n = 10 cells) ($P<0.001$, paired t-test, n = 10 cells).

I further confirmed the method by testing the sensitivity to alterations of the higher-order chromatin architecture through the application of the approach used by Albiez et al. [136]. It consists in a modulation of chromatin compaction in living cells from normally condensed chromatin to hypercondensed chromatin (HCC) by increasing the osmolarity of the culture medium from 290 mOsm (standard osmolarity of normal growth medium) to 570 mOsm. This protocol increased chromatin condensation (Fig.3.8g,h). HeLa cells showed dense chromatin regions throughout the nucleus, followed by a reduction in nuclear size. The average FRET level A was reported as a function of the relative acceptor-to-donor abundance n* (Fig.3.8i). The larger value of slope indicated that treatment with hyperosmolar solution had induced an increase in the nanoscale compaction as measured by FRET. Similarly, the maps of corrected FRET level A_0^* showed that nanoscale compaction was higher ($P<0.001$, t-test) in

hypercondensed chromatin (A_0^*=1.57 ± 0.025, mean ±s.e.m., n = 11 cells) compared to control nuclei (A_0^* =0.92 ± 0.025, mean ±s.e.m., n = 8 cells) (Fig.3j).

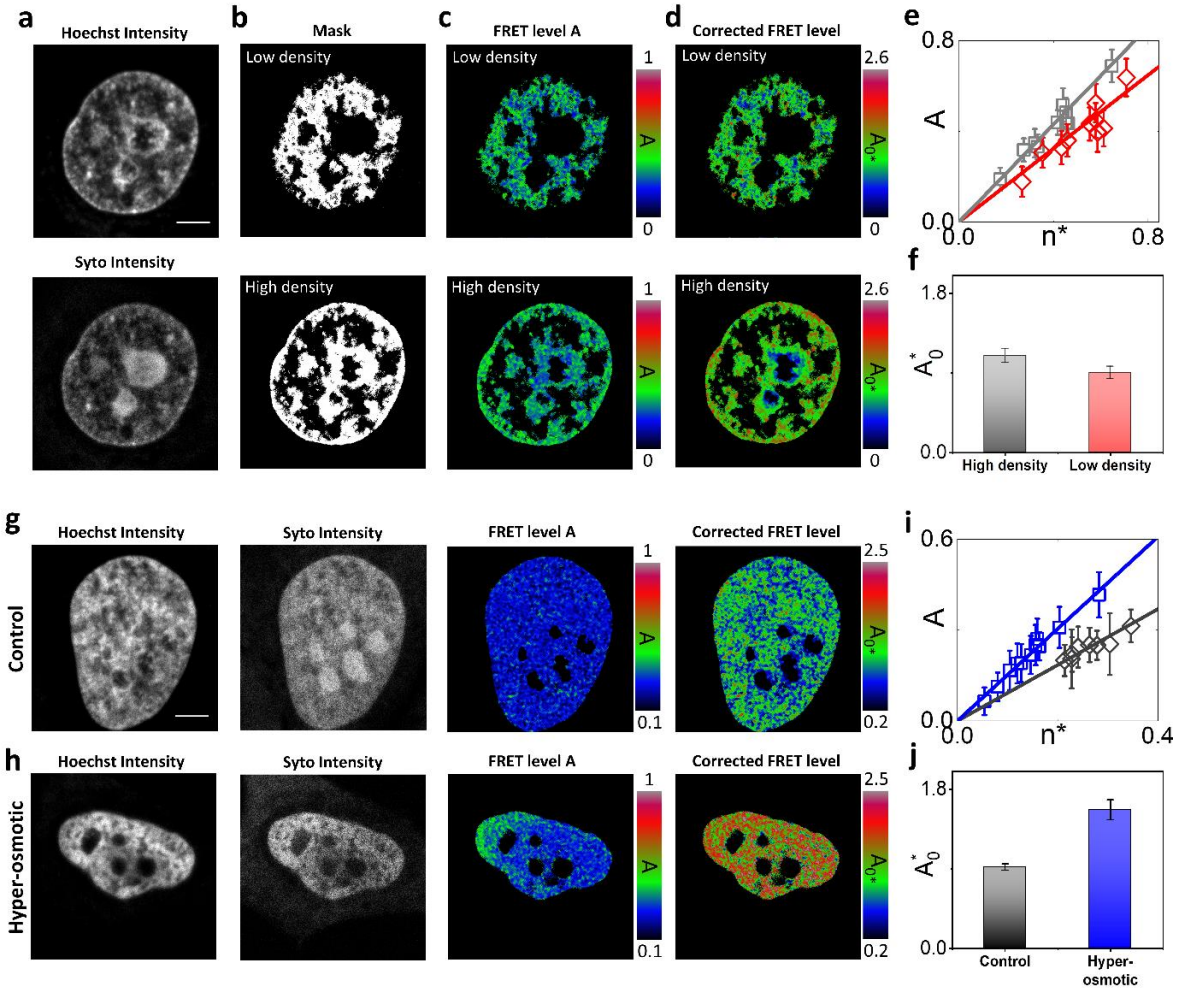

Figure 3.8. Corrected FRET assay shows different levels of nanoscale chromatin compaction. (a-f) FRET analysis of regions of different chromatin density in live HeLa cell nuclei. **(a)** Intensity images of the donor and acceptor channel. **(b)** Masks generated from the Hoechst intensity signal to discriminate between high-density (heterochromatin) and low-density (euchromatin) regions. **(c)** Color maps of FRET level A in low density (left) and high density (right) regions. **(d)** Color maps of the corrected FRET level A_0^*. **(e)** Plot of A versus the relative acceptor-to-donor abundance n*. Each experimental point is the mean ± s.d value of A calculated in a high (grey squares) or low (red diamonds) density region. The solid lines are linear fits of the data through the origin (high density: slope= 1.07; low density: slope= 0.81). **(f)** Comparison of mean value of A_0^* of heterochromatin (high density) and euchromatin (low density). Data are mean ± s.d. (n=10 cells) of the mean values of A_0^* calculated on each cell. **(g-j)** FRET analysis of hyper-osmotic nuclei. **(g,h**) Representative images of a control cell nucleus and a nucleus after hyper-osmolar treatment. Shown are the intensity in the donor and acceptor channel, the FRET level A and the corrected FRET level A_0^*. A_0^* color maps reveals and higher nanoscale compaction in hyper-osmotic nucleus with respect the control. **(i)** Plot of A versus the relative acceptor-to-donor abundance n*. Each experimental point is the mean ± s.d value of A calculated in control (grey diamonds) or hyper-osmotic (blue squares) nuclei. The solid lines are linear fits of the data through the origin (control: slope= 0.92; hyper-osmotic: slope= 1.52) **(j)** Comparison of mean value of A_0^* of control and hyper-osmotic

nuclei. Data are mean ± s.d. (control: n=8 cells; hyper-osmotic: n=11 cells) of the mean values of A_0* calculated on each cell. Scale bar: 5μm.

3.4.4 Corrected FRET assay reveals chromatin remodeling during DNA damage response (DDR)

In this section, I applied the corrected FRET method to investigate the decompaction of chromatin, at the nanoscale, in response to induction of DNA damage. Chromatin remodeling during DNA damage response (DDR) is a complex process. In particular, it has been previously reported that, in a short time interval immediately after the local induction of DNA damage (<5 min), chromatin undergoes a rapid transient expansion followed by a slower compaction phase [141][142]. The rapid decondensation of chromatin in the early phase of DDR is a required step to allow the DNA-repair machinery to access the damaged region, thereby facilitating DNA damage repair [19].

I generated DNA damage on a selected region of interest (ROI) of the nuclei by 405nm-laser micro-irradiation and sensitization with Hoechst 33342, as reported previously [143]. To verify the DNA damage effect of the 405nm-laser micro-irradiation on HeLa cell nuclei stained with Hoechst 33342, employed as a sensitizer, I monitored the expression of the DDR marker PARP-1 (poly-(ADP-ribose) polymerase1). PARP-1 is a specific protein that rapidly accumulates at genome sites where single strand breaks (SSBs) or double strand breaks (DSBs) have occurred [144][145]. The expression of PARP-1 was monitored in cells fixed immediately after micro-irradiation and in live cells (Fig.3.9).

To confirm a local decondensation of DNA at the irradiation site, I observed accumulation of PARP-1 on the irradiated region in fixed cells, revealed by post-fixation labeling with the DNA dye TO-PRO-3 [146], as expected (Fig.3.9a-c). In live cells, we also observed photobleaching of Hoechst 33342 and accumulation of PARP-1 on the irradiated region (Fig. 3.9d). The accumulation of PARP-1 was more noticeable towards the center of the nucleus (Fig.3.9d). One possible explanation for this effect is that more DNA damage is generated towards the center of the nucleus where the

thickness is larger. In this respect, it is worth noting that, under one-photon excitation regime, the absorption of light and the subsequent generation of DNA damage is not limited to the focal plane but extended to the whole exposed volume [147].

I then measured the FRET level on HeLa cells stained with Hoechst 33342 and Syto 13 right after a region of the nucleus was exposed to laser micro-irradiation (Fig.3.9e-h). The FRET measurements were performed immediately after irradiation (within minutes), to focus only on the nanoscale rearrangement of chromatin occurring during the first expanding phase. The maps of corrected FRET level A_0^* showed that nanoscale compaction was lower in the exposed region of the nucleus (A_0^*=0.87 ± 0.05, mean ±s.e.m., n = 6 cells) compared to the non-exposed region (A_0^*=1.14 ± 0.05, mean ±s.e.m., n = 6 cells) (Fig.3.9f-h, $P<0.005$, paired t-test). The lower value of corrected FRET shows a local decompaction of chromatin, at the nanoscale, in response to DNA damage induction, probably to promote the access of the DNA-repair machinery required for DNA damage repair, in keeping with reported models of chromatin organization [19].

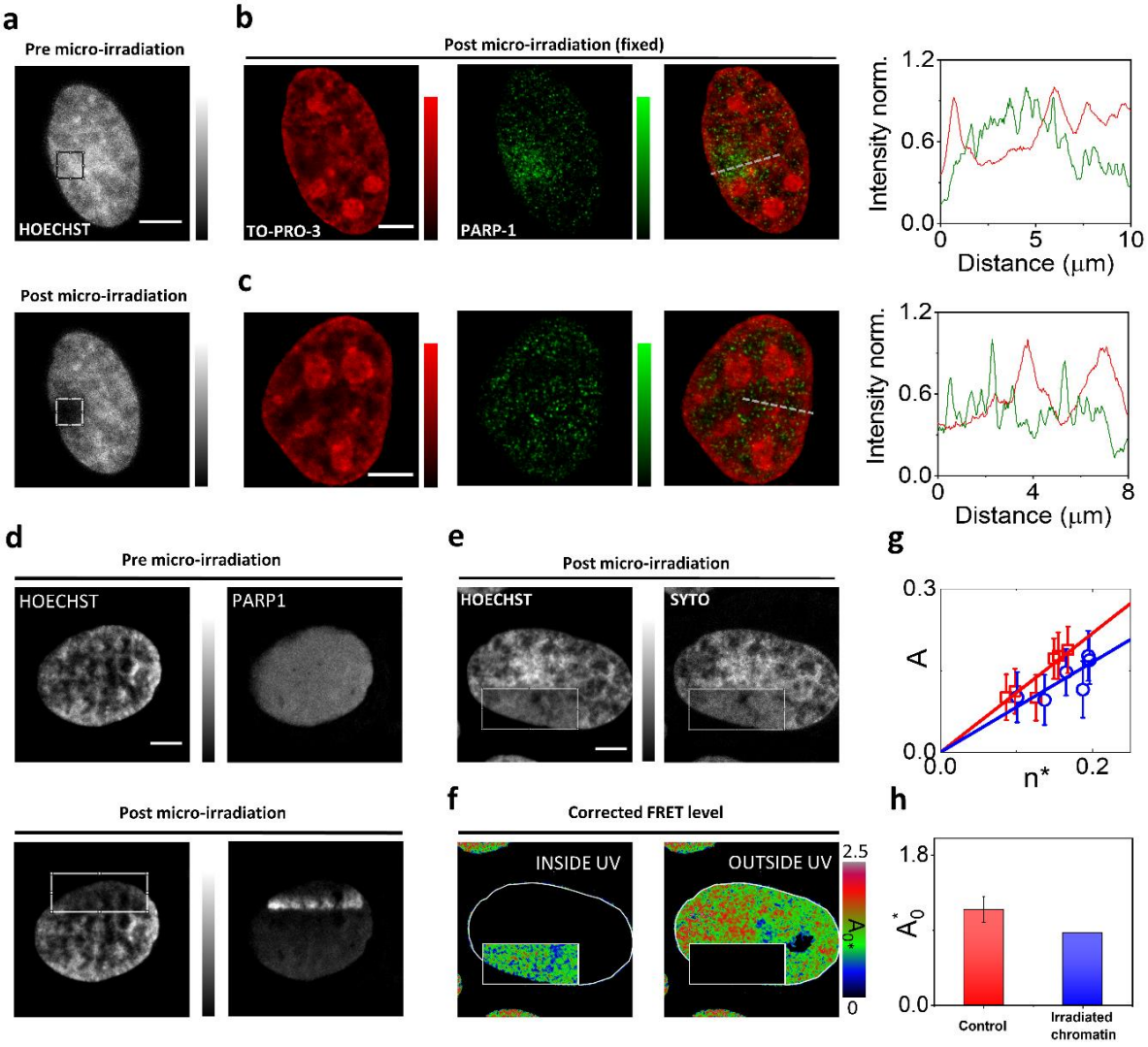

Figure 3.9. **Corrected FRET assay reveals nanoscale decompaction of chromatin in response to DNA damage. (a)** DNA damage is induced by UV-microirradiation in a region of interest (ROI) in a live HeLa cell nucleus labeled with Hoechst. **(b,c)** Confocal images showing DNA staining with TO-PRO-3 and immunodetection of PARP-1 in the same HeLa cell fixed in 4% PFA immediately after micro-irradiation **(b)** and in a control cell **(c).** Line profile shows the intensity signal distribution of TO-PRO-3 (red) and PARP-1 (green) in the irradiated region. **(d)** Representative images of a live HeLa cell nucleus stained with Hoechst and expressing PARP1-Chromobody-TagRFP. Following local UV-microirradiation, there is accumulation of PARP-1 in the irradiated region. (e-h) FRET analysis in live HeLa cells stained with Hoechst and Syto 13 after local UV-microirradiation. **(e)** Intensity images of the donor and acceptor channel**. (f)** Color maps of the corrected FRET level (A_0*) in selected masks representing the UV-irradiated ROI and outside ROI. **(g)** Plot of A versus the relative acceptor-to-donor abundance n*. Each experimental point is the mean ± s.d value of A calculated in UV-irradiated ROI (blue circles) or outside ROI (red squares) inside nuclei. The solid lines are linear fits of the data through the origin (UV-irradiated ROI: slope= 0.82; outside ROI: slope= 1.1) **(h)** Comparison of mean value of A_0* of UV-irradiated and outside ROIs inside nuclei. Data are mean ± s.d. (n=6 cells) of the mean values of A_0* calculated on each cell. Scale bar: 5μm.

3.4.5 Estimation of the concentration of Hoechst 33342 and Syto 13 molecules involved in FRET interaction

As already explained, FRET process provides information about the nanometer distances between fluorophores. However, I showed that the average FRET efficiency measured on a given pixel depends also on how many donors and acceptors are engaged in the FRET interaction. For instance, in protein-protein interactions it is common to describe FRET data in terms of a mixture of two species: a fraction of unquenched donors and a fraction of donors undergoing FRET with an acceptor [100]. Working in a crowded system as the cell nucleus, I cannot make any prior hypothesis on the stoichiometry of the FRET interaction. In order to convert the measured values of FRET efficiency into nanometer values, it is necessary to know the absolute value of the ratio N_A/N_D. Assuming that $n^*(x,y) = \frac{\beta_A}{\beta_D}\frac{N_A(x,y)}{N_D(x,y)}$, the relationship between N_A/N_D and our experimental parameter n^* is given by:

$$\frac{N_A}{N_D} = \frac{\beta_D}{\beta_A} n^* \tag{3.8}$$

where β_A and β_D are the brightness of the acceptor and of the unquenched donor in the acceptor and donor channel, respectively. The corrected FRET value $A_0^*(x,y) = \frac{A(x,y)}{n^*(x,y)}$ is proportional to the FRET level $A_0(x,y) = \frac{A(x,y)}{N_A/N_D}$ corresponding to an acceptor-donor ratio of 1:

$$A_0^*(x,y) = \frac{\beta_D}{\beta_A}\frac{A(x,y)}{N_A(x,y)/N_D(x,y)} = \frac{\beta_D}{\beta_A} A_0(x,y) \tag{3.9}$$

Using solutions of known concentration of organic dyes with similar emission spectra, I estimated the value of the constant β_A/β_D (Fig. 3.10).

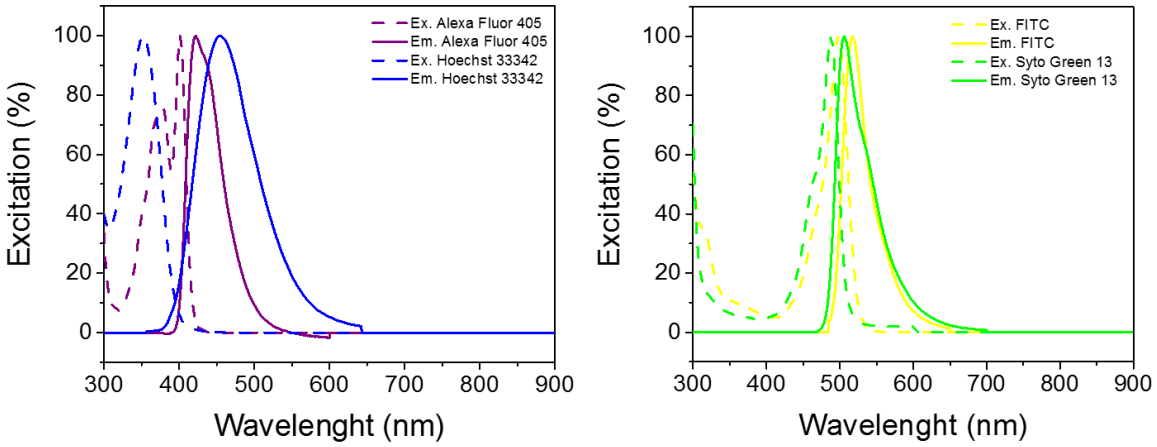

Figure 3.10. Excitation and emission spectra of Hoechst 33342/Alexa Fluor 405 and Syto Green 13/FITC, respectively (Source: thermofisher.com).

I first determined the ratio between the brightness of Fluorescein in the acceptor channel (β_2) and the brightness of Alexa 405 in the donor channel (β_1). This ratio was determined by measuring the fluorescence intensity I_1 and I_2 from distinct solutions of known concentration C_1 and C_2 of the two dyes under the same level of 405 nm excitation power.

$$\frac{\beta_2}{\beta_1} = \frac{I_2 C_1}{I_1 C_2} \tag{3.10}$$

Then I estimated the value of β_A/β_D as:

$$\frac{\beta_A}{\beta_D} = \frac{\beta_2}{\beta_1} \frac{\varepsilon_A QY_A \, \eta_A \varepsilon_1 QY_1 \eta_1}{\varepsilon_D QY_D \, \eta_D \varepsilon_2 QY_2 \eta_2} \tag{3.11}$$

Where the values of quantum yield (QY) and extinction coefficient (ε) at 405 nm for each dye were estimated from reported literature and manufacturers datasheets (Table 1). The parameter η represents the percentage of the emission spectrum of each fluorophore that is collected within its specific bandpass filter.

DYE	Q.Y.	ε	% abs (405nm)	ε_{405nm}
Alexa Fluor 405	0.54	35000 $M^{-1}cm^{-1}$	86%	30100 $M^{-1}cm^{-1}$
Fluorescein	0.93	76900 $M^{-1}cm^{-1}$	2%	1540 $M^{-1}cm^{-1}$
Hoechst 33342	0.38	47000 $M^{-1}cm^{-1}$	3.5%	1645 $M^{-1}cm^{-1}$
Syto Green 13	0.4	50000 $M^{-1}cm^{-1}$	5%	2500 $M^{-1}cm^{-1}$

Table 1. Parameters related to the dyes Alexa Fluor 405 in DMSO, fluorescein in 0.1M NaOH, Hoechst 33342 bound to DNA, Syto 13 bound to DNA. Reported are the quantum yield (QY), the extinction coefficient at the absorption peak (ε), the percentage of absorption at λ=405 nm relative to the absorption peak and the extinction coefficient at λ=405 nm (ε405).

Following the expression $N_A/N_D = (\beta_D/\beta_A) \times n^*$, I finally estimated indirectly that, in our system, β_D/β_A~2.5, resulting in absolute values of acceptor-to-donor ratios N_A/N_D ranging between ~0.4 and ~2 in our experiments. If this estimation is correct, we can then calculate the FRET level corresponding to a donor-acceptor pair as $A_0=A_0^*/(\beta_D/\beta_A)$. For the control samples, this value is in the order of A_0~0.4, corresponding to a FRET efficiency in the order of E_0~0.3 and average donor-acceptor distances in the order of ~1.2 Forster radii. Assuming a Forster radius of ~5 nm, this corresponds to ~6 nm. According to recent electron microscopy observations, chromatin can be described a disordered chain with diameters between 5 and 24 nm, packed together at different concentration densities in interphase nuclei [23]. We can speculate that variations in the local density of this chain determine variations of the average acceptor-donor distance and thus variations in the detected FRET. In this framework, a variation of A_0 from 0.36 to 0.44, like that observed between euchromatin and heterochromatin (Fig.3.8), would correspond to a variation of average acceptor-donor distance from ~1.2 to only ~1.1 Forster radii.

3.5 Conclusions

In this work, I showed that a pair of DNA-binding dyes, normally used as nuclear counterstains, can be used as a FRET system to map chromatin compaction within live cell nuclei. I defined a successful strategy to distinguish the variations of FRET related to the donor-acceptor distance from the variations of FRET related to the acceptor-to-donor abundance. This approach is based on the combination of both spectroscopy parameters of fluorescence lifetime and intensity. The FRET level is quantified by the decrease of the donor lifetime, which is detected by frequency domain-FLIM, and then normalized to the relative acceptor-donor ratio, which is estimated from the intensity values in the acceptor and donor channels. To validate this strategy, we measured the FRET level in regions of high and low DNA density, as defined by the relative amount of Hoechst signal, and found that heterochromatin regions had a higher FRET level compared to the euchromatin regions. We also showed that nuclei of cells treated with a hyperosmolar medium reveal a higher FRET level compared to control nuclei. Finally, we applied our FRET method to monitor nanoscale reorganization of chromatin during response to DNA damage: we found that chromatin is locally decompacted, at the nanoscale, in response to DNA damage induction, probably to promote the access of the molecular machinery required for DNA damage repair.

These results show that, thanks to the normalization step, the reported FRET assay can be used to investigate chromatin organization in live cells, and is a valid alternative to the previously reported histone-based FRET systems. A major drawback, compared to the histone-based FRET assay, is that it is not straightforward to interpret our data in terms of the higher order organization of chromatin-DNA. Indeed, while the inter-nucleosome distance is a parameter directly connected to the chromatin higher order organization, here the precise spatial distribution of the two fluorophores on the DNA macromolecule is poorly defined. I can only make some simple assumptions on the distribution of the two binding dyes on DNA and

attempt to estimate their average distance from the measured values of FRET efficiency.

A second consideration concerns the variation of average acceptor-donor distance (from ~1.2 to only ~1.1 Forster radii) between hetero- and eu-chromatin regions. Comparing with an estimated 2.6-fold difference of total DNA density between the two compartments, this variation of distance can seem relatively small [148]. However, this is not shocking considering the heterogeneity in the nanodomain size recently observed for DNA and nucleosome higher-order structures [84][148][23]. The estimation of the average interaction distance might be inaccurate, as it does not rely on a robust calibration protocol. The simplest way to estimate the ratio $\beta D/\beta A$ would be to use a sample with a 1:1 stoichiometry of the two fluorescent dyes [149]. This is particularly challenging in my system, since the effective amount of dye bound to DNA can be very different from that of the staining solution, and the brightness of a dye bound to DNA is much higher than that of the free dye. In this context, I believe it would be interesting to perform a similar analysis on the histone-based FRET assays [126][127][95] where the use of fluorescent proteins would allow a more robust calibration with constructs of known stoichiometry [149] and a direct estimation of the average nanometer distance between labeled histones.

Chapter 4

4.Chromatin organization investigated at the nanoscale by SPLIT-STED

4.1 State of the art

In the eukaryotic cell nucleus, several heterogeneous nuclear structures, such as the nuclear lamina (NL), participate in the nanoscale organization of chromatin. The NL is a meshwork consisting of A- and B-type lamins and lamin-associated proteins and serves as a grid for multiple chromatin anchoring sites. It shapes the spatial organization of chromosomes in the interphase nucleus, where the high-density heterochromatin is mainly located at the nuclear periphery, in opposite to the less compacted euchromatin, which is in a more interior nuclear position [10][150][151][152][20]. At a morphological level, the organization and dynamics of these nuclear structures are suggested to play an active role in the activation and repression to gene expression and, consequently, to be required for healthy cell proliferation and maintenance. One of the strategies to study chromatin organization at the nanoscale is to use FRET, a process sensitive to nanometer distances but limited to the 10nm range [126][127][153]. The recently developed super-resolution fluorescence microscopy (SRM) techniques provide a spatial resolution tunable down to molecular levels (1-200nm). The super-resolution STED microscopy [28] can reach the molecular size by increasing the intensity of the STED beam, but

it is limited by other factors, such as the amount of laser power that can cause photodamage effects to the sample. For this reason, new strategies have been developed to reduce the peak power of the STED beam necessary to reach a given spatial resolution. An example is represented by Time-gated Continuous-Wave STED microscopy (gCW-STED), which exploits the reduction of fluorophore lifetime due to the STED beam, reducing the depletion power more than 50% [73][19]. Theoretically, the spatial resolution of the gated STED microscope improves with the time-delay, but since a portion of photons from the PSF center is also discarded, the limiting factor becomes the signal-to-noise ratio (SNR). This can be made worse by the presence of uncorrelated background signal, such as that generated by direct excitation from the CW-STED beam[73][154][155].

In last years, our group introduced a novel approach to achieve the nanoscale resolution required to image nuclear structures, which interact with chromatin nanoscale organization: separation of photons by lifetime tuning (SPLIT)[76]. As explained in Chapter 2, to improve the spatial resolution of a CW-STED microscope, the SPLIT method extracts, at each pixel, the fraction of the signal corresponding to the longer fluorescence lifetime. To extract this fraction, SPLIT performs a phasor analysis of the time-resolved data, namely, the nanosecond fluorescence intensity decay at each pixel of the image is transformed from time to frequency domain and represented as a phasor by using the Fourier transform. This phasor is decomposed into a phasor component corresponding to the center of the PSF (longer lifetime) and a phasor component corresponding to the periphery of the PSF (shorter lifetime). The phasor $P(x,y)$ can be expressed as the linear combination of the total number of photons of the single spatial components $P_{IN}(x,y)$ and $P_{OUT}(x,y)$, plus the uncorrelated background *(BKGD)* $N = N_{IN} + N_{OUT} + N_{BKGD}$, where only N_{IN} represents the "photons of interest". The phasor of the confocal image (zero STED power) is centered to the position corresponding to a single exponential decay lifetime of the fluorophores. With the increasing of the STED beam power the phasor becomes elongated, generating different fluorescence dynamics at the periphery of the PSF. For each pixel, the fraction $\omega_{in}(x,y)$ of fluorescence decay intensity associated with the center of

the PSF was estimated by expression of phasor P(x,y) as a combination of the phasors of the two spatial components, representing the fluorescence dynamics within PSF.

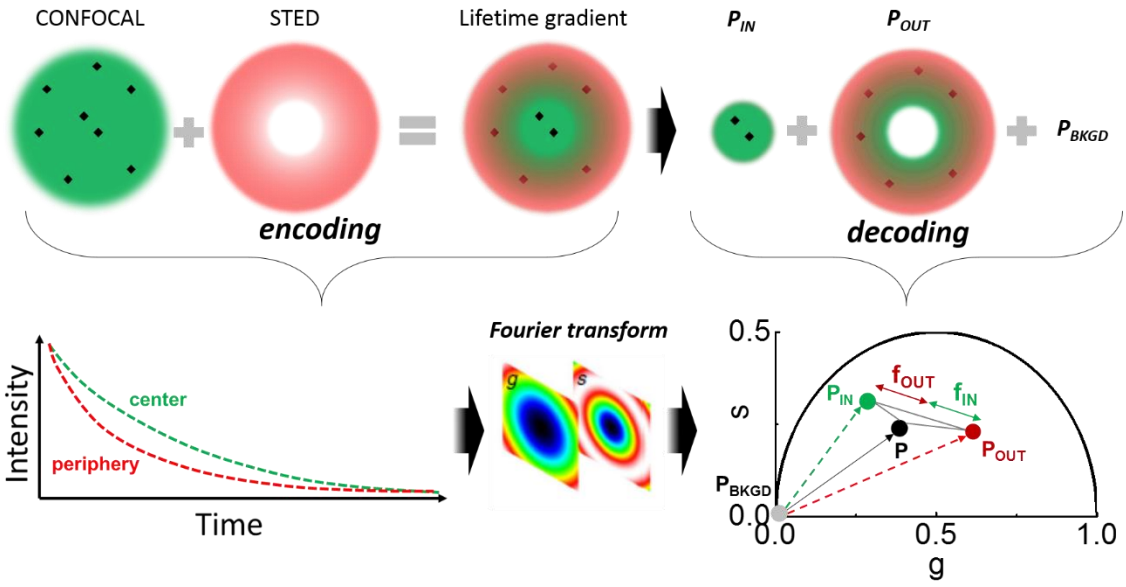

Figure 4.1. Schematic principle of the SPLIT method in time-resolved CW-STED. A doughnut-shaped STED beam overlapped with a confocal spot generates a continuous distribution of dynamics within the diffraction limited (DL)-PSF. The STED beam intensity determines the relative variation of decay rate within a Gaussian DL-PSF. It is assumed that the photons are emitted within the DL-PSF with a different dynamics (center or periphery) according to the emitter position. The SPLIT method uses the temporal information of the signal at each pixel to generate a set of g and s images throughout Fourier transform. The phasor plot, expressing the experimental phasor P as a linear combination of the phasors P_{IN} and P_{OUT} plus the phasor of the background (P_{BKGD}), decodes the temporal information. The goal is to separate the photons emitted from the center, those emitted from periphery and those with no temporal dynamics (uncorrelated background, BKGD).

An advantage of lifetime-based SPLIT is the intrinsic removal of direct excitation from the STED beam from the final image [76]. On the other hand, the generation and observation of fluorescence lifetime gradients require pulsed excitation and dedicated hardware for lifetime detection in the nanosecond temporal scale, which are not available on every STED microscope.

Recently, we have overcome this limitation by applying the SPLIT algorithm to STED images obtained with tunable depletion power [32]. The results of this work clearly demonstrated that the 'spectroscopy' approach to super-

resolution microscopy proposed by SPLIT is not limited to the analysis of fluorescence lifetimes but can have a more general application in STED microscopy. In this case, the additional channel for SPLIT was represented by the depletion power, a parameter that can be easily tuned on any STED microscope, without the need for dedicated lifetime detection hardware. In a straightforward implementation, we demonstrated that SPLIT could be applied to stacks of n STED images acquired sequentially at increasing depletion power [120]. In this implementation [120], the spatial information is encoded in the fluorescence signal by using the power of the STED beam ($k = P_{STED}$).

Application of SPLIT to the stacks resulted in improved super-resolution imaging of nuclear transcription and replication foci in fixed cells [120].

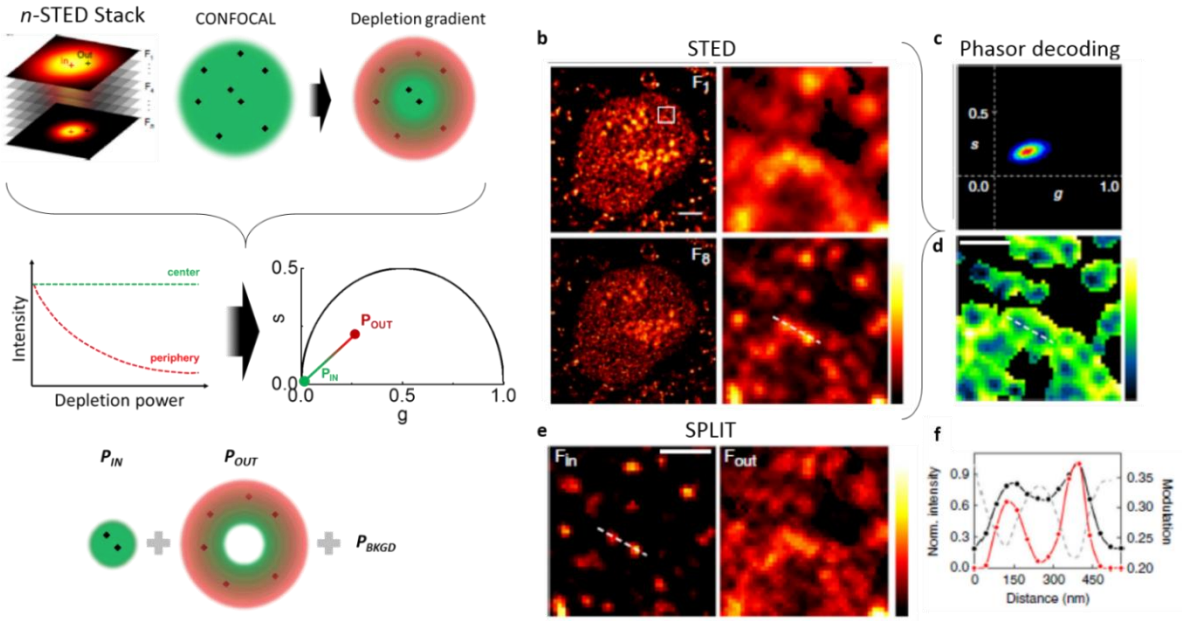

Figure 4.2. SPLIT-STED microscopy implementation and application on transcription foci in MCF10A cells. (a) Schematic representation of acquired image stack with increasing STED power, from F1 to Fn. STED beam generates a fluorescence depletion gradient of photons arising from the center (in) and the periphery (out) of the PSF, along the stack. The encoded fluorescence dynamics information is decoded by the phasor analysis, separating the photons in the center and in periphery. The SPLIT image is obtained upon application of the SPLIT alghoritm. **(b)** Acquired stack images, from the confocal (F1) to maximum STED power (F8) of transcription foci within intact MCF10A nuclei. Scale bar: 3 µm. **(c)** Phasor plot obtained from the data and **(d)** the corresponding modulation image M(x,y). Scale bar: 500 nm. **(e)** F_{in} and F_{out} images obtained by application of SPLIT to F8. Color scale: normalized intensity. Scale bar: 500 nm. **(f)** Line profile of the two foci within intact nuclei between F8 (black line) and Fin (red line), and the relation with the information encoded in the modulation M (dash grey line). Shown is the ability of SPLIT to improve the optical resolution.

Optimal STED imaging of a given sample always relies on the proper tuning of several acquisition parameters, including the depletion and excitation powers, and the integration time. In particular, a major limitation to the total number of photons that can be collected during STED imaging is represented by the onset of photobleaching. For this reason, the acquisition of a stack of n STED images, required for SPLIT, may present some practical limitations. For instance, in the specific implementation described in Ref. [156], a stack of n = 8 images was generated by linearly increasing the value of STED power PSTED from zero (PSTED=0) up to a maximum value (PSTED=Pmax), keeping a constant laser excitation power. Even if one has already optimized the STED imaging parameters for a given sample at the STED power Pmax, these parameters must be carefully modified for the acquisition of a stack of n frames with STED power varying from 0 to Pmax. In fact, in addition to the number of photons N required for the acquisition of the STED image at PSTED, one has to collect an extra number of photons $\sim(n-1)\times N$ for the acquisition of the other n-1 images of the stack, which is likely to results in more severe photobleaching.

4.2 Main goal of the project

In this project, I explored the potential advantages of modulating also the excitation power during acquisition of a SPLIT stack of STED images with tunable depletion power. The idea raised from the limitation provided by the photobleaching effect for a given depletion power, which affects the improvement of resolution and the maintenance of the sample. The photobleaching rate is expected to increase at higher excitation powers and/or longer integration times. Thus, the level of the excitation power plays a critical role in optimizing the acquisition of the stack of n STED images required for SPLIT. The main advantage of modulating the excitation power is that the number of photons collected can be tuned independently for each STED image of the stack. This has mainly two effects on the data:

1) the susceptibility to photobleaching can be modulated by varying the number of photons acquired at the different STED powers. This aspect is important to reduce photobleaching and improve compatibility with live cell imaging.

2) The generation of a SPLIT stack composed of single frames with very different SNR. In this respect, we need to verify that, despite the variations of SNR, it is possible to generate a final SPLIT image with improved spatial resolution compared to the STED image of highest power.

In the SPLIT-STED implementation based on tunable depletion power, described in Sarmento et al 2018, F(x,k) represents a stack of STED images acquired at increasing STED power and constant excitation power (Fig.4.3a). In this implementation, the fluorescence intensity of a fluorophore located in the center (r=0) of the detection volume (or PSF), f_{SF}(k,r=0), is constant as a function of k, whereas that of a fluorophore located in its periphery, f_{SF}(k,r>0), decays as a result of the increasing action of the STED beam (Fig.4.3a). Since the excitation power is kept constant, each STED image of the stack is collected with roughly a constant peak signal-to-noise ratio, i.e., for each detection volumes the number of photons collected from the central region (r = 0) is constant with respect to k, N1~ N2~…~Nk~…~NM (Fig.4.3a), with M the number of different values for the STED beam power. The integrated image Fsum(x), used for formation of the SPLIT image, has a spatial resolution intermediate between the STED image acquired at minimum STED power, $F_{k=1}(x)$, and the STED image acquired at maximum STED power, $F_{k=M}(x)$. I apply a modified SPLIT-STED implementation, tuning also the excitation power during the acquisition of a stack of STED images acquired at increasing STED power (Fig.4.3b,c). In this implementation, the maximum number of photons N_k collected for each STED image of the stack can be tuned independently. As a result, one can generate different SPLIT data acquisition scenarios.

For instance, one can increase the excitation power concomitantly with the depletion power, in order to get more photons at the higher STED powers and thus get a higher SNR in the frames containing higher spatial frequencies

(Fig.4.3b). In this case, the integrated image $F_{1\text{-}n}(x,y)$ used for formation of the SPLIT image has a spatial resolution closer to that of the STED image of maximum resolution, $F_n(x,y)$. This improvement of resolution comes at the expense of an increased level of photodamage.

Conversely, one can decrease the excitation power in opposition to the depletion power, to get less photons at the higher STED powers and thus reduce the potentially detrimental impact of simultaneous high excitation and STED powers (Fig.4.3c). In this second case, we expect a significant reduction of photodamage. However, this reduction of photodamage comes at the expense of a lower resolution. In fact, the integrated image $F_{1\text{-}n}(x,y)$ used for SPLIT has a spatial resolution closer to the image of the stack with minimum resolution $F_1(x,y)$.

I apply this methodology to the imaging of nuclear structures, such as nuclear lamin and the nuclear pore complex (NPC), in fixed and live eukaryotic cells. I will show that the simultaneous modulation of STED and excitation power improves the versatility of the SPLIT-STED method for super-resolution imaging of nuclear structures.

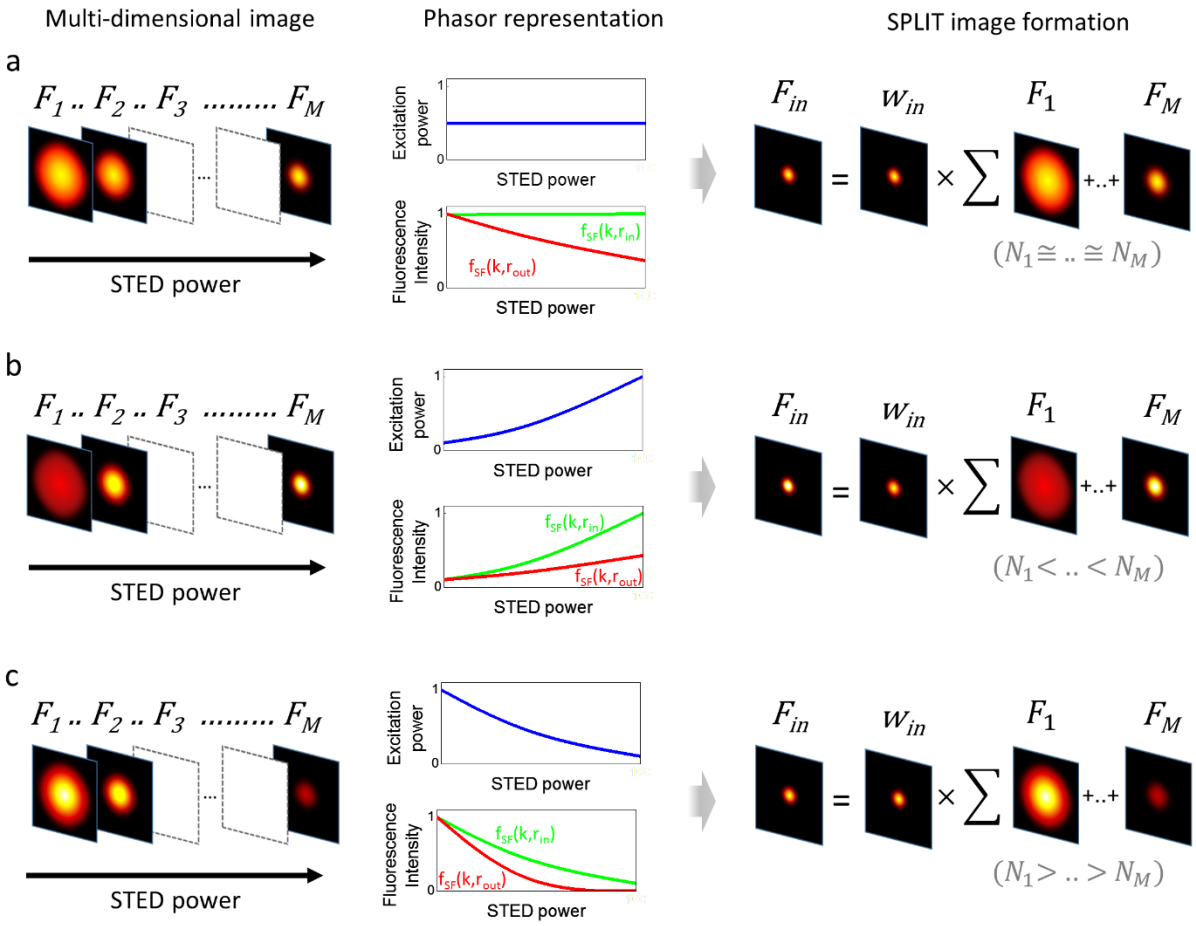

Figure 4.3. Schematic principle of different SPLIT-STED configurations. The multi-dimensional image $F_{1..M}$ contains an extra spatial information encoded in an additional channel. In **a-c**, the extra information is provided by increasing the STED power from F_1 to F_M. The intensity curves $f_{SF}(k,r_{in})$ *and* $f_{SF}(k,r_{out})$ show the fluorescence depletion dynamics of a single fluorophore arising from the center (in) and the periphery (out) of the PSF, along the stack. The fluorescence signal depends on the excitation pattern (blue line). In **a**, the excitation power is kept constant, whereas in **b,c** is exponentially modulated. In all the configurations (**a-c**), the SPLIT image F_{in} is generated by the SPLIT algorithm by the fraction w_{in}, obtained by the phasor analysis, multiplied for the integrated image $F_{sum} = \sum F_1 + .. + F_M$. The distribution of photons N along the STED stack depends on the excitation pattern.

4.3 Materials and Methods

4.3.1 Cells culture and sample preparation

HOS, HEK and HeLa cells were cultured in Dulbecco's modified Eagle's medium (DMEM) (Sigma-Aldrich) supplemented with 10% FBS, 2 mM L-glutamine and 1% penicillin/streptomycin in a humidified incubator at

37°C with 5% CO2. PC3 cells were cultured in Ham's F12K (Thermo Fisher Scientific) medium containing 7% FBS, 2 mM L-glutamine and 1% penicillin/streptomycin. Cells were grown in humidified incubator at 37°C with 5% CO2. For nuclear pore immunolabeling, immunofluorescence was carried out as described previously [Pesce et al, J Biophot 2019]. Human osteosarcoma (HOS) cells were plated at 70% confluency on 18 mm coverglass and grown overnight. The cells are pre-extracted with 2.4% PFA and 0.3% Triton-X100 in PBS for 3 min. After fixation with 2.4% PFA for 30 min, the cells are blocked for 1 hour with 5% BSA. Then, the cells are incubated overnight at 4 °C with primary antibody anti-Nup153 (ab84872; AbCam) in BSA 5%. After washing several times in PBS, the cells are incubated with the secondary antibody Alexa488 (A28175; Thermofisher Scientific) at room temperature for 1 hour. Human embryonic kidney (HEK) cells were fixed with ice-cold methanol for 10 min at –20 °C. After incubation in BSA, the cells were incubated with primary antibody anti-lamin B2 (33-2100; Thermofisher Scientific) overnight at 4 °C. After several washes in PBS, the cells were incubated with the secondary antibody Alexa Fluor 488 (A28175; Thermofisher Scientific) at room temperature for 1 h.

For live cell imaging, HeLa cells cells were plated on Ibidì µ-slide 8-well chambered coverslips and let grow overnight at 60–80% confluence. After 24h, cells were transiently transfected with SNAP-tag Lamin A (Plasmid #58193; Addgene), according to QIAGEN Effectene protocol. For SNAP-tag labeling, we used 5 µM cell-permeable SNAP-cell 505-star dye (New England Biolabs Inc.) in complete medium with 0.5% BSA, and left incubating for 30 min at 37°C. After cells were washed three times with the culture medium (Cellular Labeling protocol S9103; New England Biolabs Inc).

4.3.2 Experimental setup

All imaging experiments were performed on a Leica TCS SP5 gated-CW-STED microscope, using a HCX PL APO ×100 100/1.40/0.70 oil

immersion objective lens (Leica Microsystems, Mannheim, Germany). Emission depletion was accomplished with a 592 nm STED laser. Excitation was provided by a white laser at the desired wavelength for each sample. Alexa 488 and SNAP-cell 505-star were excited at 488 nm and the fluorescence emission detected at 500–560 nm. Time gating was set 1.5-10.0 ns for all the images. The frame size was set to 512×512 pixels (Lamin A, Nup153) and 1024x1024 pixels (Lamin B). Stacks of M=3 STED images with different STED power were obtained using the line sequential acquisition mode (1400 Hz). The STED power in the 3 images was set to 0, $P_{max}/2$ (12.5 mW), P_{max} (25 mW), respectively. The excitation level in the 3 frames was set to a constant value or tuned according to an exponential pattern:

$$P_{exc}(k) = P_{exc}(1)e^{\frac{k-1}{\tau_{exc}}} \quad (4.1)$$

Where $P_{exc}(1)$ is the excitation power at frame number 1, and the constant τ_{exc} was set to $\tau_{exc}=1$ and $\tau_{exc}=-1$, respectively. Both STED and excitation powers were measured after the objective, at the sample plane.

4.4 Results

4.4.1 Modified SPLIT-STED method on simulation data

Primarily, by using simulated images of random distributions of point-like particles, generated with Matlab (Mathworks) software, I verified if the STED stacks obtained with the new implementation could be used to produce SPLIT images. The simulated stacks consisted of n=3 STED images generated to simulate increasing STED power throughout the stack, and different patterns of the excitation intensity. Taking in account that only three different STED powers are required for the graphical

analysis of the phasor plot, I simplified the SPLIT algorithm to a series of n = 3 images with different distribution of photons.
To create the image stacks, the objects were convolved with the following PSF of a STED microscope [120][157]:

$$i(r,k) = N(k)e^{-\frac{2r^2}{w^2}}e^{-\varsigma(k)\frac{r^2}{w^2}} \tag{4.2}$$

Where N(k) is the maximum number of counts per particle, $r=(x^2+y^2)^{1/2}$, w is the width of the confocal PSF, ς(k) is the STED saturation factor at radial position r=w. The STED saturation factor is defined as the ratio between the STED intensity at position r=w and the constant I_{sat}:

$$\varsigma(k) = \frac{I_{STED}(k)}{I_{sat}} \tag{4.3}$$

The saturation factor was set as ς(1)=0, $\varsigma(2)=\varsigma_{max}/2$, $\varsigma(3)=\varsigma_{max}$. The waist of the confocal PSF was set to w = 320 nm.
To simulate different patterns of the excitation tuning, the prefactor $N(k)$ in Eq. (4.2) was set to

$$N(k) = N(1)e^{\frac{k-1}{\tau}} \tag{4.4}$$

where $N(1)$ is the maximum number of counts per particle in the first frame and the constant τ_{exc} can take both positive and negative values. To verify that the STED stacks obtained with the new implementation could be used to produce SPLIT images, we simulated images of random distributions of point-like particles. The simulated stacks consisted of M=3 STED images generated to simulate increasing STED power throughout the stack, and different patterns of the excitation intensity. We chose M=3 to further simplify the acquisition settings. The modulation of the excitation intensity along the stack depends only the constant τexc, which can take both positive and negative values. If τ_{exc} >

0, the excitation has an exponential growth, if $\tau_{exc} < 0$ the excitation has an exponential decay (Fig.4.4).

In Fig.4.4 we compare simulated data obtained with excitation patterns corresponding to $\tau_{exc}=1$ (Fig.4.4a), $\tau_{exc}=\infty$ (Fig.4.4b) and $\tau_{exc}=-1$ (Fig.4.4c). The data have been simulated with the same maximum total number of counts per particle, N(1)+N(2)+N(3)=20. For each condition, we show the first and last frame of the stack, the phasor plot and the SPLIT image (Fig.5). In all three cases, the information encoded in the variations of STED power can be used to produce a SPLIT image with higher spatial resolution than the STED images, as quantified by Fourier ring Correlation (FRC) (Fig.4.4) [158]. The integrated image used for formation of the SPLIT image in Eq.2.37 can also be obtained by a partial sum of the frames of the stack. For instance, one may want to include in the integrated image only the STED frames with higher spatial resolution. We tested by FRC if there was any advantage in using only the last frame F3 or the sum of the F_2-F_3 or F_1-F_2-F_3 frames (Fig.4.4). The results of this analysis show no significant difference between the SPLIT images calculated using the total or a partial sum of the frames of the stack. This indicates that the potential advantage of excluding the frames with poorer spatial resolution is counterbalanced by the reduction in the number of photons used for the final image.

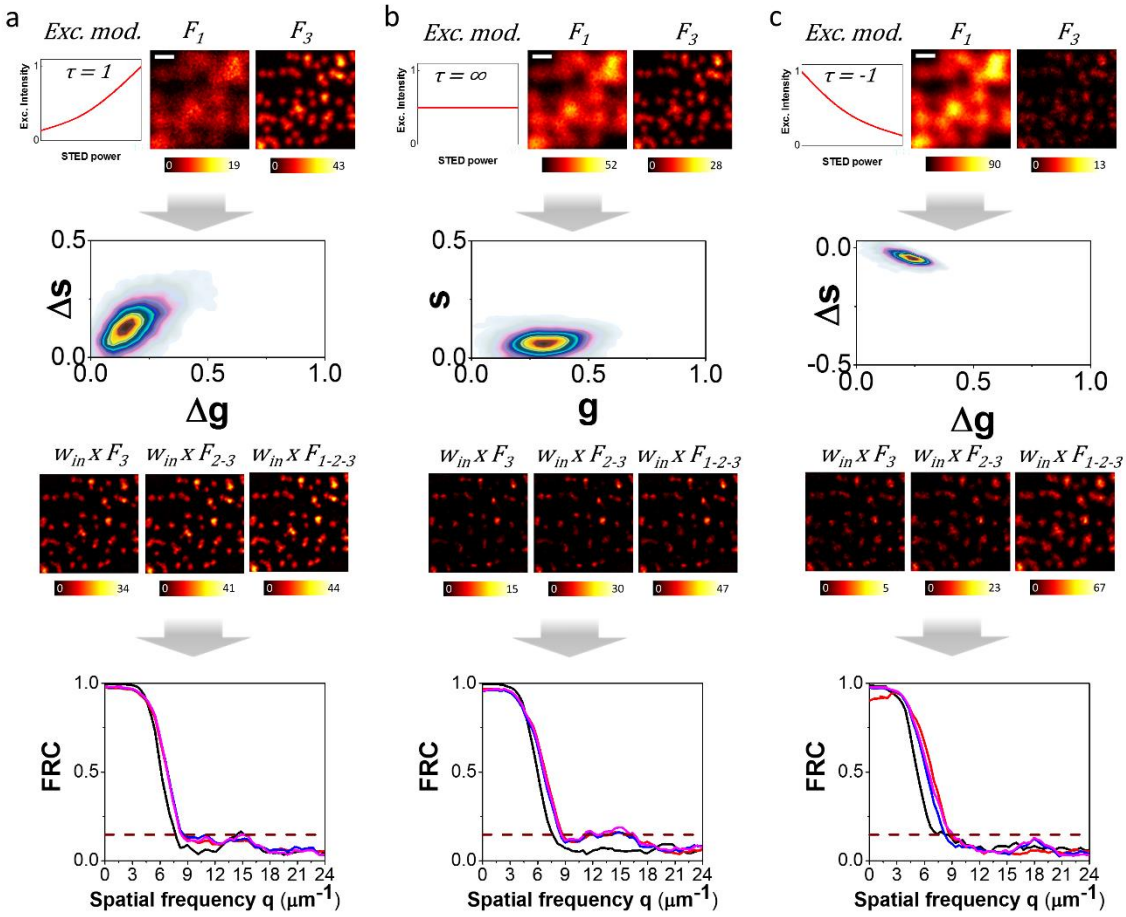

Figure 4.4. Excitation patterns and phasor analysis in SPLIT-STED. Simulations of nuclear spots under different conditions of acquisition. **a-c** were simulated with the same STED saturation factor ς_{max} = 10. The SNR varies depending on the synchronized effect of the STED power and the excitation power modulation (red excitation curve). The simulations wrere implemented with three different excitation pattern: τ_{exc} = 1 **(a)**, τ_{exc} = ∞ **(b)** and τ_{exc} = -1 **(c).** Shown are, for each simulation (from top to bottom): the average variation of fluorescence intensity in the first and last image of the stack (F_1 and F_3), the corresponding phasor plot, the final SPLIT image obtained by multiplying the fraction w_{in} with the sum of F_1 +F_2 + F_3, the FRC curves corresponding to the effective resolution of the STED image F_3 (black) and the SPLIT images (colored). The FRC analysis showed the following resolution values: for τ_{exc} = 1, 128nm (STED) and 116nm (SPLIT); for τ_{exc} = ∞, 128nm (STED) and 111nm (SPLIT); for τ_{exc} = -1, 135nm (STED) and 128nm (SPLIT). Scale bar: 1 μm.

Image spatial autocorrelation functions (ACF) were calculated in Matlab using the algorithm described in Ref. [159]. The ACFs were fitted to a Gaussian model to extract the average width of the effective PSF expressed as FWHM. The simulated data show that the SPLIT approach can be applied to STED stacks obtained by simultaneous modulation of STED and excitation power, despite the significant variations of SNR along the stack.

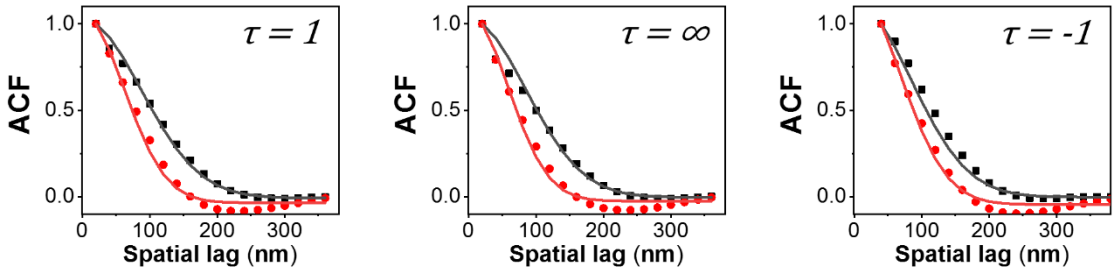

Figure 4.5. Spatial correlation functions of the STED image F_3 (black squares) and the SPLIT image (red circles). For each value of τ_{exc},the autocorrelation function measured the width of the PSF, expressed as FWHM: for τ_{exc} = 1, $FWHM_{STED}$ = 144nm and $FWHM_{SPLIT}$ = 104nm; for τ_{exc} = ∞, $FWHM_{STED}$ = 142nm and $FWHM_{SPLIT}$ = 97nm; and for τ_{exc} = -1, $FWHM_{STED}$ = 139nm and $FWHM_{SPLIT}$ = 113nm.

4.4.2 Evaluation of Photobleaching for the different excitation patterns

I apply all the three SPLIT-STED configurations with different excitation patterns, corresponding to τ_{exc}=1, τ_{exc}=∞ and τ_{exc}=−1 (Fig.4.6), to test the photobleaching effect during a time-lapse acquisition, on fixed HeLa cell. In particular, I visualized the α-tubulin labeled with Alexa Fluor 488 (Materials and Methods). I measured the photobleaching kinetics occurring under an acquisition with tunable power of a 592-nm CW-STED beam. Both the STED power and the excitation power (488-nm) were tuned simultaneously by setting a line-sequential acquisition.

As expected, all the excitation patterns showed a general decrease of the fluorescence signal, but the configuration with negative constant τ produced less photobleaching on the specimen compared with the configuration with τ_{exc} =1 and τ_{exc} =∞, probably thanks to the lower excitation of the sample in the time window in which the power of STED is at maximum (F_3 image). This suggests that this SPLIT-STED configuration could be useful to minimize the effects of photobleaching and phototoxicity in live samples.

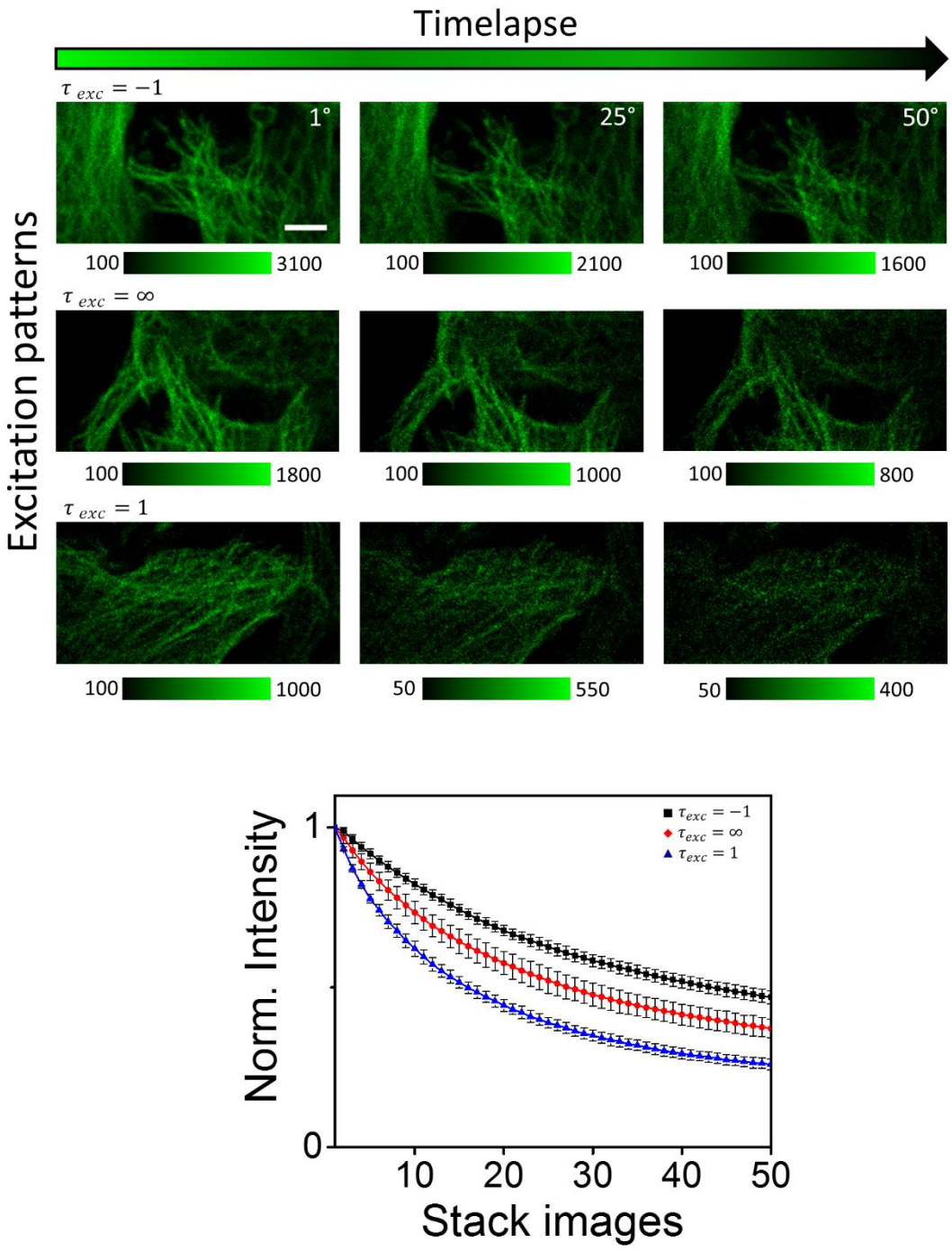

Figure 4.6. Photobleaching evaluation for the different SPLIT-STED configurations. Shown are the decrease of fluorescence signal of α-tubulin labeled with Alexa Fluor 488, in fixed HeLa cells, during a timelapse SPLIT-STED acquisition of 50 frames for each excitation pattern. Scale bar: 3μm.

4.4.3 Modified SPLIT-STED method on fixed cells

I tested the first SPLIT-STED configuration, namely excitation modulation with positive constant τ, for the imaging of fixed cells. In particular, we visualized nuclear lamin-B and the nuclear pore complex (NPC) protein Nup153, labeled with Alexa Fluor 488 (Materials and Methods). In this configuration, the last frame (F_3) of the stacks, should contain the best resolved structures, due to the maximum depletion power by 592-nm STED beam, and also the highest SNR, due to the maximum level of the excitation power (Fig.4.7a,g,m).

For each acquisition, we show the phasor plot and the map of the parameter m, which describes the variation along the main axis of symmetry of the phasor. Both the phasor plot and the "m" map reveal the encoded spatial information used to produce the SPLIT image. To estimate the improvement of spatial resolution, we show line profiles and the FRC analysis.

By fitting the line profile with single- and multi-peak Gaussian function, we estimate the FWHM of these biological structures. The line profile of the Nuclear pore complex (NPC) image shows $FWHM_{F3}$ ~ 127 nm and $FWHM_{Fin}$ ~ 87 nm. Nuclear B-lamin was analyzed in median and apical focal planes showing its structure from different point of view. We estimate the FWHM of the median plane to be ~ 192nm in F_3 and ~ 61nm in F_{in}, whereas ~ 88nm and ~ 72nm in F_3 and ~64nm and ~31nm in F_{in} of the apical plane. The improvement of spatial resolution is also confirmed by FRC analysis performed on the same data (Fig.4.7f,l,r).

These values represent a strong improvement in resolution of tens of nanometers, reinforcing the usefulness of the modulation of excitation for the SPLIT algorithm. However, this configuration has significant higher level of photobleaching compared to the configurations with $\tau_{exc} = \infty$ and $\tau_{exc} = -1$, due to the detrimental impact of simultaneous high excitation and STED powers (Fig. 4.6).

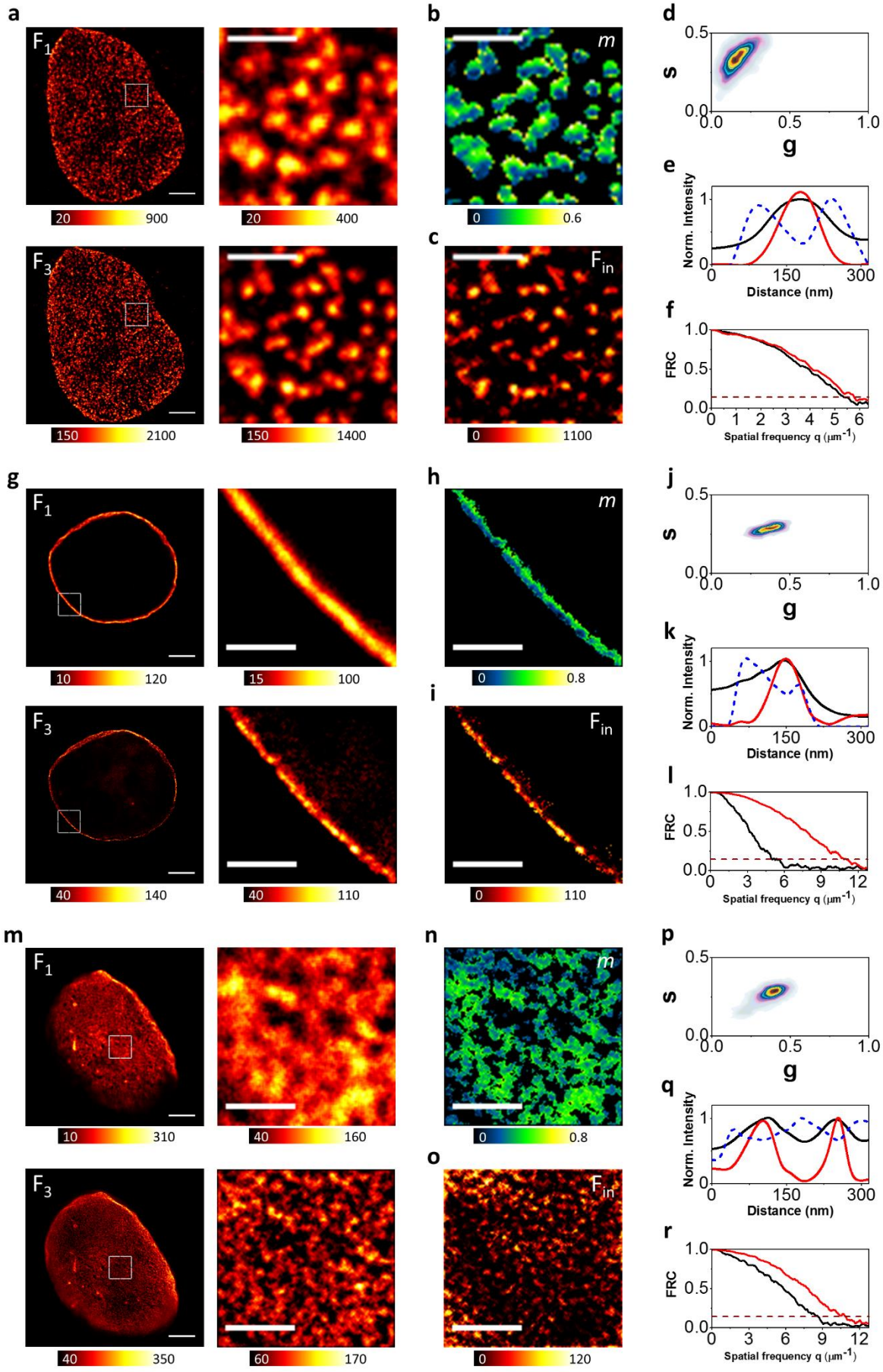
a
F1
20
900
20
400
F3
150
2100
150
1400
b
m
0
0.6
c
Fin
0
1100
d
s
g
e
Norm. Intensity
Distance (nm)
f
FRC
Spatial frequency q (μm-1)
g
F1
10
120
15
100
F3
40
140
40
110
h
m
0
0.8
i
Fin
0
110
j
s
g
k
Norm. Intensity
Distance (nm)
l
FRC
Spatial frequency q (μm-1)
m
F1
10
310
40
160
F3
40
350
60
170
n
m
0
0.8
o
Fin
0
120
p
s
g
q
Norm. Intensity
Distance (nm)
r
FRC
Spatial frequency q (μm-1)

Figure 4.7. SPLIT-STED of nuclear structures within intact nuclei of fixed cells. **(a,g,m)** Acquired stack images of Nup153 (**a**), median **(g)** and apical **(m)** Lamin-B, from the confocal (F_1) to maximum STED power (F_3) (Pmax = 25 mW), with exponential increase of excitation power (τ_{exc} = 1). Scale bar: 3µm (Scale bar ROI: 1µm). **(b,h,n)** Modulation image. Color scale: *m* (0–0.6/0.8). **(c,i,o)** Corresponding phasor plots obtained from the data. Scale bar: 1µm. **(d,j,p)** SPLIT image F_{in} obtained by application of SPLIT to F_3. Scale bar: 1µm. **(e,k,q)** Line profiles show the improvement of spatial resolution of nuclear structures from F_3 (black line) to F_{in} (red line), and the relation with the information encoded in the modulation image (dash blue line). **(f,l,r)** FRC analysis confirms the corresponding effective resolution of the STED image (black curve) and the SPLIT image (red curve). The FRC curves showed the following resolution values: for Nup153, 184nm (F_3) and 172nm (F_{in}); for median Lamin-B, 199nm (F_3) and 90nm (F_{in}); for apical Lamin-B, 115nm (F_3) and 91nm (F_{in}).

4.4.4 Modified SPLIT-STED method on live cells

Afterwards, I tested the second SPLIT-STED configuration, in which the excitation was modulated exponentially with negative constant τ. We tested this configuration on live HeLa cells transfected with SNAP-tag Lamin A and labeled with the SNAP-cell 505-star dye. Here we acquired the images of the stacks modulating the excitation laser with an exponential decay from the frame F_1 to F_3 (Fig.4.8). As shown in Fig.4.8, the confocal image F_1 (I_{exc}=max, I_{sted}=0) contained the highest fluorescence intensity signal, in opposite to F_3 image (I_{exc}=low, I_{sted}=max), where the intensity signal is very low, due to the synchronized effect of a weak excitation power with maximum depletion power. Also in this case, we were able to produce a SPLIT image with better spatial resolution than the STED image (Fig.4.9a-c). However, as we can observe from the F_3 image and, consequently, from its line profile, the signal-to-noise ratio was too low to determine a value of FWHM. Therefore, we compare the SPLIT image ($FWHM_{Fin}$ ~140nm) with the integrated image $F_{1\text{-}3}$ ($FWHM_{Fsum}$ ~305nm) (Fig.4.9b).

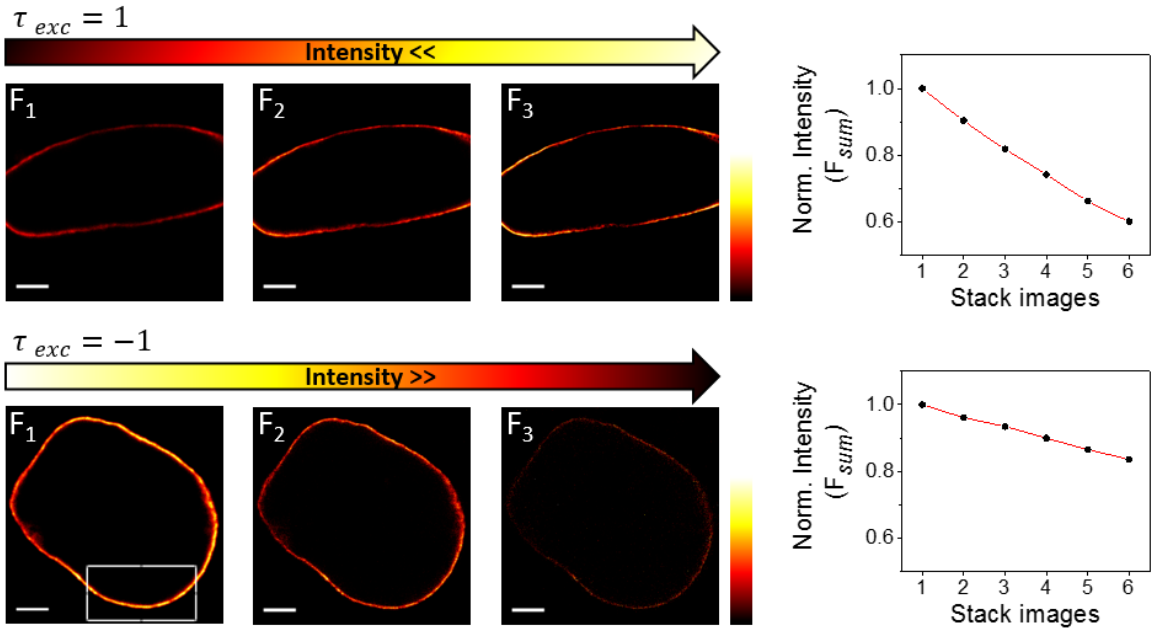

Figure 4.8. Photobleaching measured in live cells labeled with Lamin-A SNAP 505*. Shown are the sequential image acquisition with positive (τ_{exc} = 1) and negative (τ_{exc} = -1) excitation patterns. The intensity curves show the intensity signal decrease for each excitation pattern, during a timelape acquisition (6 frames).

A time-lapse SPLIT-STED acquisition is reported in Fig.4.9c. Thanks to the reduced level of photobleaching, the number of photons collected per time-frame remains high enough to perform the SPLIT analysis, as demonstrated also by the phasor plot and the “m” map (Fig.4.9c,d).

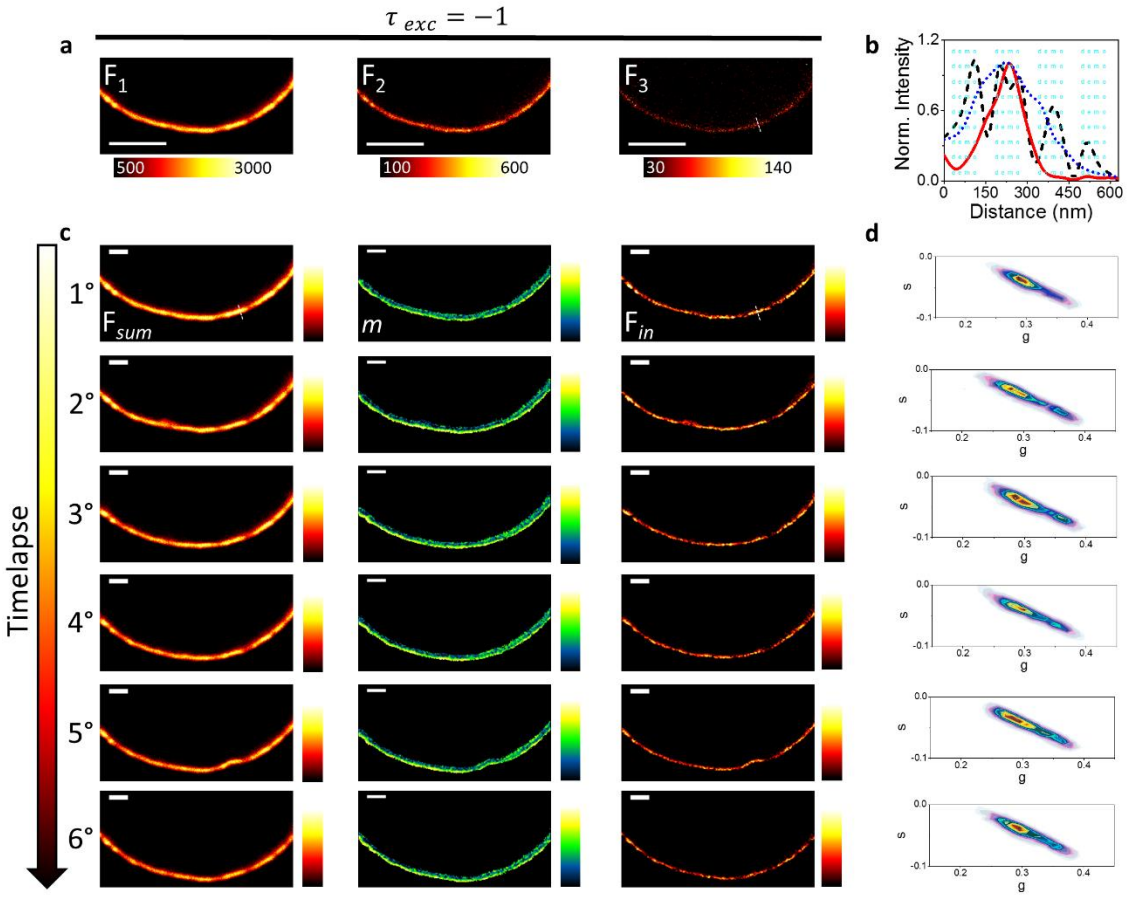

Figure 4.9. SPLIT-STED of nuclear Lamin-A in intact nuclei of live cells. (a). Acquired stack images of Lamin-A, from the confocal (F_1) to maximum STED power (F_3) (Pmax = 25 mW), with exponential decay of excitation power (τ_{exc} = -1)**.** Scale bar: 3µm. **(b)** Line profiles show the effective spatial resolution of Lamin-A in F_{sum} image (dash green line), F_{in} image (red line) and F_3 image (dash black line). **(c)** Shown are, for each frame (1-6) of the timelapse (from left to right): the integrated image $F_{sum} = F_1 + F_2 + F_3$, the modulation image with the corresponding phasor plots **(d)** and the SPLIT image F_{in} obtained by application of SPLIT to F_{sum}. Scale bar: 1µm.

4.5 Conclusion

The SPLIT approach is a simple and efficient way which exploits the additional spatial information *k* potentially encoded in the g(x,y) and s(x,y) images describing the evolution of the fluorescence signal in a pixel-by-pixel manner and improving the spatial resolution of a fluorescence multi-dimensional image F(x,k),

Sarmento et al. exploit the tunability of the STED microscope to generate STED images at different depletion power, resulting in an improvement of spatial resolution. We decode the spatial information derived from the modulation of STED power (M-STED) by using the phasor plot.

However, for SPLIT analysis, a stack of n = 8 images was generated to increasing STED power, from the confocal image (F1, P_{STED} = 0) to the one with the highest STED power (F8, P_{STED} = Pmax), keeping a constant laser excitation power. In many experimental cases, the acquisition of a series of n = 8 images at constant excitation power may present some practical limitations. The optimization of the acquisition parameters for the stack is not always straightforward.

In this work, we have exploited the associated advantage tuning both the STED and excitation power, to improve the versatility of the SPLIT-STED approach. The tuning of the depletion power is used to produce STED images at different resolution and to generate the non-linearity required by the SPLIT method. The tuning of the excitation power is used to modulate the number of photons collected for each STED image. We have shown that the SPLIT-STED method produces an improvement of spatial resolution for very different tuning patterns of the excitation intensity. An interesting aspect emerging from our study is that the extent of photobleaching can be modulated by the excitation pattern, as it depends on the simultaneous impact of high STED and excitation powers.

In summary, the tuning of the excitation power improves the resolution power of the SPLIT method, acting on the SNR and extends the applicability of the method to live cell imaging, decreasing the photobleaching of the fluorophores and the phototoxicity of the biological samples.

References

1. Richmond, T.J., and Davey, C.A. (2003) The structure of DNA in the nucleosome core. *Nature*, **423** (6936), 145–150.

2. Luger, K., Mäder, A.W., Richmond, R.K., Sargent, D.F., and Richmond, T.J. (1997) Crystal structure of the nucleosome core particle at 2.8 Å resolution. *Nature*, **389** (6648), 251–260.

3. Luger, K., Dechassa, M.L., and Tremethick, D.J. (2012) New insights into nucleosome and chromatin structure: an ordered state or a disordered affair? *Nat. Rev. Mol. Cell Biol.*, **13** (7), 436–447.

4. Fussner, E., Ching, R.W., and Bazett-Jones, D.P. (2011) Living without 30nm chromatin fibers. *Trends Biochem. Sci.*, **36** (1), 1–6.

5. Cremer, T., and Cremer, C. (2001) Chromosome territories, nuclear architecture and gene regulation in mammalian cells. *Nat. Rev. Genet.*, **2** (4), 292–301.

6. Misteli, T., et al. (2007) Beyond the Sequence: Cellular Organization of Genome Function. *Cell*, **128** (4), 787–800.

7. Fedorova, E., and Zink, D. (2008) Biochimica et Biophysica Acta Nuclear architecture and gene regulation. *Biochim. Biophys. Acta*, **1783**, 2174–2184.

8. Poleshko, A., Mansfield, K.M., Burlingame, C.C., Andrake, M.D., Shah, N.R., and Katz, R.A. (2013) The Human Protein PRR14 Tethers Heterochromatin to the Nuclear Lamina during Interphase and Mitotic Exit. *Cell Rep.*, **5** (2), 292–301.

9. Huisinga, K.L., Brower-Toland, B., and Elgin, S.C.R. (2006) The contradictory definitions of heterochromatin: transcription and silencing. *Chromosoma*, **115** (2), 110–122.

10. Sexton, T., Schober, H., Fraser, P., and Gasser, S.M. (2007) Gene regulation through nuclear organization. *Nat. Struct. Mol. Biol.*, **14**, 1049.

11. Trojer, P., and Reinberg, D. (2007) Facultative Heterochromatin: Is There a Distinctive Molecular Signature? *Mol. Cell*, **28** (1), 1–13.

12. Rae, P.M.M., and Franke, W.W. (1972) The interphase distribution of satellite DNA-containing heterochromatin in mouse nuclei. *Chromosoma*, **39** (4), 443–456.

13. Shopland, L.S., Lynch, C.R., Peterson, K.A., Thornton, K., Kepper, N., Hase, J. von, Stein, S., Vincent, S., Molloy, K.R., Kreth, G., Cremer, C., Bult, C.J., and O'Brien, T.P. (2006) Folding and organization of a contiguous chromosome region according to the gene distribution pattern in primary genomic sequence . *J. Cell Biol.*, **174** (1), 27–38.

14. Mattout, A., Cabianca, D.S., and Gasser, S.M. (2015) Chromatin states and nuclear organization in development — a view from the nuclear lamina. *Genome Biol.*, **16** (1), 174.

15. Li, B., Carey, M., and Workman, J.L. (2007) The Role of Chromatin during Transcription. *Cell*, **128** (4), 707–719.

16. Fournier, L.-A., Kumar, A., and Stirling, C.P. (2018) Chromatin as a Platform for Modulating the Replication Stress Response. *Genes* , **9** (12).

17. MacAlpine, D.M., and Almouzni, G. (2013) Chromatin and DNA Replication. *Cold Spring Harb. Perspect. Biol.* .

18. Chaudhuri, A.R., and Nussenzweig, A. (2017) The multifaceted roles of PARP1 in DNA repair and chromatin remodelling. *Nat. Rev.*, **18** (10), 610–621.

19. Price, B.D., and Andrea, A.D.D. (2014) Chromatin Remodeling at DNA Double Strand Breaks. *Cell*, **152** (6), 1344–1354.

20. Misteli, T. (2010) Higher-order genome organization in human disease. *Cold Spring Harb. Perspect. Biol.*, **2** (8), a000794–a000794.

21. Robinson, P.J.J., Fairall, L., Huynh, V.A.T., and Rhodes, D. (2006) EM measurements define the dimensions of the "30-nm" chromatin fiber: Evidence for a compact, interdigitated structure. *Proc. Natl. Acad. Sci.*, **103** (17), 6506 LP – 6511.

22. Song, F., Chen, P., Sun, D., Wang, M., Dong, L., Liang, D., Xu, R.-M., Zhu, P., and Li, G. (2014) Cryo-EM Study of the Chromatin Fiber Reveals a Double Helix Twisted by Tetranucleosomal Units. *Science (80-.).*, **344** (6182), 376 LP – 380.

23. Ou, H.D., Phan, S., Deerinck, T.J., Thor, A., Ellisman, M.H., and Shea, C.C.O. (2017) ChromEMT: Visualizing 3D chromatin structure and compaction in interphase and mitotic cells. *Science (80-.).*, **357** (6349), 1–13.

24. Woodcock, C.L., and Horowitz, R.A. (1997) Electron Microscopy of Chromatin. *Methods*, **12** (1), 84–95.

25. Passmore, L.A., and Russo, C.J. (2016) Chapter Three - Specimen Preparation for High-Resolution Cryo-EM, in *The Resolution Revolution: Recent Advances In cryoEM*, vol. 579, Academic Press, pp. 51–86.

26. Lakadamyali, M., and Cosma, M.P. (2015) Advanced microscopy methods for visualizing chromatin structure. *FEBS Lett.*, **589** (20, Part A), 3023–3030.

27. Birk, J.U. (2019) Super-Resolution Microscopy of Chromatin. *Genes* , **10** (7).

28. W Hell, S., and Wichmann, J. (1994) Breaking the Diffraction Resolution Limit by Stimulated-Emission-Depletion Fluorescence Microscopy. *Opt. Lett.* **19**

29. Gustafsson, M.G.L. (2000) Surpassing the lateral resolution limit by a factor of two using structured illumination microscopy. *J. Microsc.*, **198**, 82–87.

30. Betzig, E., Patterson, G.H., Sougrat, R., Lindwasser, O.W., Olenych, S., Bonifacino, J.S., Davidson, M.W., Lippincott-schwartz, J., and Hess, H.F. (2006) Imaging Intracellular Fluorescent Proteins at Nanometer Resolution. *Science (80-.).*, **313**, 1642–1646.

31. Rust, M.J., Bates, M., and Zhuang, X. (2006) Sub-diffraction-limit imaging by stochastic optical reconstruction microscopy (STORM). *Nat. Methods*, **3**, 793.

32. Van de Linde, S., Löschberger, A., Klein, T., Heidbreder, M., Wolter, S., Heilemann, M., and Sauer, M. (2011) Direct stochastic optical reconstruction microscopy with standard fluorescent probes. *Nat. Protoc.*, **6**, 991.

33. Baum, M., Erdel, F., Wachsmuth, M., and Rippe, K. (2014) Retrieving the intracellular topology from multi-scale protein mobility mapping in living cells. *Nat. Commun.*, **5** (4494), 1–12.

34. Dross, N., Spriet, C., Zwerger, M., Müller, G., Waldeck, W., and Langowski, J. (2009) Mapping eGFP Oligomer Mobility in Living Cell Nuclei. *PLoS One*, **4** (4), e5041.

35. Bancaud, A., Huet, S., Daigle, N., Mozziconacci, J., Beaudouin, J., and Ellenberg, J. (2009) Molecular crowding affects diffusion and binding of nuclear proteins in heterochromatin and reveals the fractal organization of chromatin. *EMBO J.*, **28** (24), 3785–3798.

36. Di Bona, M., Mancini, M., Mazza, D., Vicidominii, G., Diaspro, A., and Lanzanò, L. (2019) Measuring mobility in chromatin by intensity sorted FCS. *Biophys. J.*, **116**, 1–13.

37. Priest, D.G., Solano, A., Lou, J., and Hinde, E. (2019) Fluorescence fluctuation spectroscopy: an invaluable microscopy tool for uncovering the biophysical rules for navigating the nuclear landscape. *Biochem. Soc. Trans.*, **47** (4), 1117–1129.

38. Tian, Y., Martinez, M.M., and Pappas, D. (2011) Fluorescence Correlation Spectroscopy: A Review of Biochemical and Microfluidic Applications. *Appl. Spectrosc.*, **65** (4), 115A-124A.

39. Singh, A.P., Galland, R., Finch-Edmondson, M.L., Grenci, G., Sibarita, J.-B., Studer, V., Viasnoff, V., and Saunders, T.E. (2017) 3D Protein Dynamics in the Cell Nucleus. *Biophys. J.*, **112** (1), 133–142.

40. Digman, M.A., and Gratton, E. (2011) Lessons in Fluctuation Correlation Spectroscopy. *Annu. Rev. Phys. Chem.*, **62** (1), 645–668.

41. Kaur, G., Costa, M.W., Nefzger, C.M., Silva, J., Fierro-González, J.C., Polo, J.M., Bell, T.D.M., and Plachta, N. (2013) Probing transcription factor diffusion dynamics in the living mammalian embryo with photoactivatable fluorescence correlation spectroscopy. *Nat. Commun.*, **4** (1), 1637.

42. Hinde, E., Pandžić, E., Yang, Z., Ng, I.H.W., Jans, D.A., Bogoyevitch, M.A., Gratton, E., and Gaus, K. (2016) Quantifying the dynamics of the oligomeric transcription factor STAT3 by pair correlation of molecular brightness. *Nat. Commun.*, **7** (1), 11047.

43. Kubitscheck, U., Kückmann, O., Kues, T., and Peters, R. (2000) Imaging and Tracking of Single GFP Molecules in Solution. *Biophys. J.*, **78** (4), 2170–2179.

44. Cui, Y., Yu, M., Yao, X., Xing, J., Lin, J., and Li, X. (2018) Single-Particle Tracking for the Quantification of Membrane Protein Dynamics in Living Plant Cells. *Mol. Plant*, **11** (11), 1315–1327.

45. Manzo, C., and Garcia-Parajo, M.F. (2015) A review of progress in single

particle tracking: from methods to biophysical insights. *Reports Prog. Phys.*, **78** (12), 124601.

46. Chenouard, N., Smal, I., de Chaumont, F., Maška, M., Sbalzarini, I.F., Gong, Y., Cardinale, J., Carthel, C., Coraluppi, S., Winter, M., Cohen, A.R., Godinez, W.J., Rohr, K., Kalaidzidis, Y., Liang, L., Duncan, J., Shen, H., Xu, Y., Magnusson, K.E.G., Jaldén, J., Blau, H.M., Paul-Gilloteaux, P., Roudot, P., Kervrann, C., Waharte, F., Tinevez, J.-Y., Shorte, S.L., Willemse, J., Celler, K., van Wezel, G.P., Dan, H.-W., Tsai, Y.-S., de Solórzano, C.O., Olivo-Marin, J.-C., and Meijering, E. (2014) Objective comparison of particle tracking methods. *Nat. Methods*, **11** (3), 281–289.

47. Levi, V., and Gratton, E. (2008) Chromatin dynamics during interphase explored by single-particle tracking. *Chromosom. Res.*, **16** (3), 439.

48. Levi, V., and Gratton, E. (2007) Exploring dynamics in living cells by tracking single particles. *Cell Biochem. Biophys.*, **48** (1), 1–15.

49. Marshall, W.F., Straight, A., Marko, J.F., Swedlow, J., Dernburg, A., Belmont, A., Murray, A.W., Agard, D.A., and Sedat, J.W. (1997) Interphase chromosomes undergo constrained diffusional motion in living cells. *Curr. Biol.*, **7** (12), 930–939.

50. Chubb, J.R., Boyle, S., Perry, P., and Bickmore, W.A. (2002) Chromatin Motion Is Constrained by Association with Nuclear Compartments in Human Cells. *Curr. Biol.*, **12** (6), 439–445.

51. Ishikawa-Ankerhold, H.C., Ankerhold, R., and Drummen, G.P.C. (2012) Advanced Fluorescence Microscopy Techniques—FRAP, FLIP, FLAP, FRET and FLIM. *Mol.* , **17** (4).

52. Rayan, G., Guet, J.-E., Taulier, N., Pincet, F., and Urbach, W. (2010) Recent Applications of Fluorescence Recovery after Photobleaching (FRAP) to Membrane Bio-Macromolecules. *Sensors* , **10** (6).

53. Reits, E.A.J., and Neefjes, J.J. (2001) From fixed to FRAP: measuring protein mobility and activity in living cells. *Nat. Cell Biol.*, **3** (6), E145–E147.

54. Stasevich, T.J., Mueller, F., Brown, D.T., and McNally, J.G. (2010) Dissecting the binding mechanism of the linker histone in live cells: an integrated FRAP analysis. *EMBO J.*, **29** (7), 1225–1234.

55. Dundr, M., Hoffmann-Rohrer, U., Hu, Q., Grummt, I., Rothblum, L.I., Phair, R.D., and Misteli, T. (2002) A Kinetic Framework for a Mammalian RNA Polymerase in Vivo. *Science (80-.).*, **298** (5598), 1623 LP – 1626.

56. Forster, T. (1949) Experimental and theoretical investigation of intermolecular transfer of electron activation energy. *Z. Naturforsch.*, **4a**, 321–327.

57. Periasamy, A. (2001) Fluorescence resonance energy transfer microscopy: a mini review. *J. Biomed. Opt.*, **6** (3), 287–291.

58. Sekar, R.B., and Periasamy, A. (2003) Fluorescence resonance energy transfer (FRET) microscopy imaging of live cell protein localizations . *J. Cell Biol.*, **160**

(5), 629–633.

59. Ma, L., Yang, F., and Zheng, J. (2014) Application of fluorescence resonance energy transfer in protein studies. *J. Mol. Struct.*, **1077**, 87–100.

60. Piston, D.W., and Kremers, G.-J. (2007) Fluorescent protein FRET: the good, the bad and the ugly. *Trends Biochem. Sci.*, **32** (9), 407–414.

61. Pietraszewska-Bogiel, A., and Gadella, T.W.J. (2011) FRET microscopy: from principle to routine technology in cell biology. *J. Microsc.*, **241** (2), 111–118.

62. Sun, Y., Rombola, C., Jyothikumar, V., and Periasamy, A. (2013) Forster Resonance Energy Transfer Microscopy and Spectroscopy for Localizing Protein – Protein Interactions in Living Cells. *Cytom. Part A*, **83A** (2), 780–793.

63. Sun, Y., Wallrabe, H., Seo, S.-A., and Periasamy, A. (2011) FRET microscopy in 2010: the legacy of Theodor Förster on the 100th anniversary of his birth. *ChemPhysChem*, **12** (3), 462–474.

64. Lakowicz, J.R. (2006) *Principles of fluorescence spectroscopy*.

65. Becker, W. (2012) Fluorescence lifetime imaging - techniques and applications. *J. Microsc.*, **247** (2), 119–136.

66. Borst, J.W., and Visser, A.J.W.G. (2010) Fluorescence lifetime imaging microscopy in life sciences. *Meas. Sci. Technol.*, **21** (10), 102002.

67. Dong, B., Almassalha, L.M., Stypula-cyrus, Y., Urban, B.E., and Chandler, J.E. (2016) Superresolution intrinsic fluorescence imaging of chromatin utilizing native , unmodified nucleic acids for contrast. *PNAS*, **113** (35), 9716–9721.

68. Gratton, E., Breusegem, S., Sutin, J.D.B., Ruan, Q., and Barry, N.P. (2003) Fluorescence lifetime imaging for the two-photon microscope: time-domain and frequency-domain methods. *J. Biomed. Opt.*, **8** (3), 381–390.

69. Pawley, J.B. (2006) Handbook Of Biological Confocal Microscopy. *Springerscience+bus. Media*, **third edit**.

70. Agard, D.A., and Sedat, J.W. (1983) Three-dimensional architecture of a polytene nucleus. *Nature*, **302** (5910), 676–681.

71. Diaspro, A., Faretta, M., and Sapuppo, P. (2008) *Confocal Microscopy*, Leica Microsystems.

72. Vicidomini, G., Coto Hernández, I., D'Amora, M., Cella Zanacchi, F., Bianchini, P., and Diaspro, A. (2014) Gated CW-STED microscopy: A versatile tool for biological nanometer scale investigation. *Methods*, **66** (2), 124–130.

73. Vicidomini, G., Moneron, G., Han, K.Y., Westphal, V., Ta, H., Reuss, M., Engelhardt, J., Eggeling, C., and Hell, S.W. (2011) Sharper low-power STED nanoscopy by time gating. *Nat. Methods*, **8**, 571.

74. Vicidomini, G., Bianchini, P., and Diaspro, A. (2018) STED super-resolved microscopy. *Nat. Methods*, **15** (3), 173–182.

75. Ma, Y., and Ha, T. (2019) Fight against background noise in stimulated

emission depletion nanoscopy. *Phys. Biol.*, **16** (5), 51002.

76. Lanzanò, L., Coto Hernández, I., Castello, M., Gratton, E., Diaspro, A., and Vicidomini, G. (2015) Encoding and decoding spatio-temporal information for super-resolution microscopy. *Nat. Commun.*, **6**, 6701.

77. Kostiuk, G., Bucevičius, J., Gerasimaitė, R., and Lukinavičius, G. (2019) Application of STED imaging for chromatin studies. *J. Phys. D. Appl. Phys.*, **52** (50), 504003.

78. Lukinavičius, G., Blaukopf, C., Pershagen, E., Schena, A., Reymond, L., Derivery, E., Gonzalez-Gaitan, M., D'Este, E., Hell, S.W., Wolfram Gerlich, D., and Johnsson, K. (2015) SiR–Hoechst is a far-red DNA stain for live-cell nanoscopy. *Nat. Commun.*, **6** (1), 8497.

79. Cseresnyes, Z., Schwarz, U., and Green, C.M. (2009) Analysis of replication factories in human cells by super-resolution light microscopy. *BMC Cell Biol*, **12**, 1–12.

80. Reindl, J., Girst, S., Walsh, D.W.M., Greubel, C., Schwarz, B., Siebenwirth, C., Drexler, G.A., Friedl, A.A., and Dollinger, G. (2017) Chromatin organization revealed by nanostructure of irradiation induced γH2AX, 53BP1 and Rad51 foci. *Sci. Rep.*, **7** (1), 40616.

81. Schermelleh, L., Carlton, P.M., Haase, S., Shao, L., Winoto, L., Kner, P., Burke, B., Cardoso, M.C., Agard, D.A., Gustafsson, M.G.L., Leonhardt, H., and Sedat, J.W. (2008) Subdiffraction multicolor imaging of the nuclear periphery with 3D structured illumination microscopy. *Science*, **320** (5881), 1332–1336.

82. Markaki, Y., Smeets, D., Fiedler, S., Schmid, V.J., Schermelleh, L., Cremer, T., and Cremer, M. (2012) The potential of 3D-FISH and super-resolution structured illumination microscopy for studies of 3D nuclear architecture. *BioEssays*, **34** (5), 412–426.

83. Wanner, G., Schroeder-Reiter, E., Ma, W., Houben, A., and Schubert, V. (2015) The ultrastructure of mono- and holocentric plant centromeres: an immunological investigation by structured illumination microscopy and scanning electron microscopy. *Chromosoma*, **124** (4), 503–517.

84. Ricci, M.A., Manzo, C., Garcìa-Parajo, M.F., Lakadamyali, M., and Cosma, M.P. (2015) Chromatin Fibers Are Formed by Heterogeneous Groups of Nucleosomes In Vivo. *Cell*, **160**, 1145–1158.

85. Prakash, K., Fournier, D., Redl, S., Best, G., Borsos, M., Tiwari, V.K., Tachibana-Konwalski, K., Ketting, R.F., Parekh, S.H., Cremer, C., and Birk, U.J. (2015) Superresolution imaging reveals structurally distinct periodic patterns of chromatin along pachytene chromosomes. *Proc. Natl. Acad. Sci. U. S. A.*, **112** (47), 14635–14640.

86. Nozaki, T., Imai, R., Tanbo, M., Nagashima, R., Tamura, S., and Tani, T. (2017) Dynamic Organization of Chromatin Domains Revealed by Super-Resolution Live-Cell Imaging Article Dynamic Organization of Chromatin Domains Revealed by Super-Resolution Live-Cell Imaging. *Mol. Cell*, **67** (2), 282-293.e7.

87. Nollmann, M., and Georgieva, M. (2015) Superresolution microscopy for bioimaging at the nanoscale: from concepts to applications in the nucleus. *Res. Rep. Biol.*, 157.

88. Valeur, B. (2002) *Molecular Fluorescence Principles and Applications*.

89. Alcala, J.R., Gratton, E., and Jameson, D.M. (1985) A Multifrequency Phase Fluorometer Using the Harmonic Content of a Mode-Locked Laser. *Instrum. Sci. Technol.*, **14** (3–4), 225–250.

90. Ross, J.A., and Jameson, D.M. (2008) Time-resolved methods in biophysics. 8. Frequency domain fluorometry: applications to intrinsic protein fluorescence. *Photochem. Photobiol. Sci.*, **7** (11), 1301–1312.

91. Digman, M., and Gratton, E. (2012) Complex fluorescence decay profiles: discrete models, stretched exponential, analytical models. *Fluoresc. Lifetime Spectrosc. Imaging Princ. Appl. Biomed. Diagnostics. UC Irvine.*

92. Redford, G.I., and Clegg, R.M. (2005) Polar Plot Representation for Frequency-Domain Analysis of Fluorescence Lifetimes. *J. Fluoresc.*, **15** (5), 805.

93. Clayton, A.H.A., Hanley, Q.S., and Verveer, P.J. (2004) Graphical representation and multicomponent analysis of single-frequency fluorescence lifetime imaging microscopy data. *J. Microsc.*, **213** (1), 1–5.

94. Sanchez, S., Bakás, L., Gratton, E., and Herlax, V. (2011) Alpha Hemolysin Induces an Increase of Erythrocytes Calcium: A FLIM 2-Photon Phasor Analysis Approach. *PLoS One*, **6** (6), e21127.

95. Digman, M.A., Caiolfa, V.R., Zamai, M., and Gratton, E. (2008) The phasor approach to fluorescence lifetime imaging analysis. *Biophys. J.*, **94** (2), L14–L16.

96. Hodgson, L., Shen, F., and Hahn, K. (2010) Biosensors for characterizing the dynamics of rho family GTPases in living cells. *Curr. Protoc. cell Biol.*, **Chapter 14**, Unit-14.11.26.

97. Hinde, E., Cardarelli, F., Digman, M.A., and Gratton, E. (2012) Changes in chromatin compaction during the cell cycle revealed by micrometer-scale measurement of molecular flow in the nucleus. *Biophys. J.*, **102** (3), 691–697.

98. Hinde, E., Digman, M.A., Hahn, K.M., and Gratton, E. (2013) Millisecond spatiotemporal dynamics of FRET biosensors by the pair correlation function and the phasor approach to FLIM. *Proc. Natl. Acad. Sci.*, **110** (1), 135 LP – 140.

99. Giral, H., Lanzano, L., Caldas, Y., Blaine, J., Verlander, J.W., Lei, T., Gratton, E., and Levi, M. (2011) Role of PDZK1 protein in apical membrane expression of renal sodium-coupled phosphate transporters. *J. Biol. Chem.*, **286** (17), 15032–15042.

100. Giral, H., Cranston, D.A., Lanzano, L., Caldas, Y., Sutherland, E., Rachelson, J., Dobrinskikh, E., Weinman, E.J., Doctor, R.B., Gratton, E., and Levi, M. (2012) NHE3 Regulatory Factor 1 (NHERF1) modulates intestinal sodium-dependent phosphate transporter (NaPi-2b) expression in apical microvilli. *J.*

Biol. Chem., **287** (42), 35047–35056.

101. Stringari, C., Cinquin, A., Cinquin, O., Digman, M.A., Donovan, P.J., and Gratton, E. (2011) Phasor approach to fluorescence lifetime microscopy distinguishes different metabolic states of germ cells in a live tissue. *Proc. Natl. Acad. Sci.*, **108** (33), 13582 LP – 13587.

102. Datta, R., Alfonso-García, A., Cinco, R., and Gratton, E. (2015) Fluorescence lifetime imaging of endogenous biomarker of oxidative stress. *Sci. Rep.*, **5**, 9848.

103. Wright, B.K., Andrews, L.M., Jones, M.R., Stringari, C., Digman, M.A., and Gratton, E. (2012) Phasor-FLIM analysis of NADH distribution and localization in the nucleus of live progenitor myoblast cells. *Microsc. Res. Tech.*, **75** (12), 1717–1722.

104. Parasassi, T., and Gratton, E. (1995) Membrane lipid domains and dynamics as detected by Laurdan fluorescence. *J. Fluoresc.*, **5** (1), 59–69.

105. Parasassi, T., Krasnowska, E.K., Bagatolli, L., and Gratton, E. (1998) Laurdan and Prodan as Polarity-Sensitive Fluorescent Membrane Probes. *J. Fluoresc.*, **8** (4), 365–373.

106. Golfetto, O., Hinde, E., and Gratton, E. (2013) Laurdan Fluorescence Lifetime Discriminates Cholesterol Content from Changes in Fluidity in Living Cell Membranes. *Biophys. J.*, **104** (6), 1238–1247.

107. Owen, D.M., Rentero, C., Magenau, A., Abu-Siniyeh, A., and Gaus, K. (2012) Quantitative imaging of membrane lipid order in cells and organisms. *Nat. Protoc.*, **7** (1), 24–35.

108. Golfetto, O., Hinde, E., and Gratton, E. (2015) The Laurdan Spectral Phasor Method to Explore Membrane Micro-heterogeneity and Lipid Domains in Live Cells BT - Methods in Membrane Lipids (eds.Owen, D.M.), Springer New York, New York, NY, pp. 273–290.

109. Fereidouni, F., Bader, A.N., and Gerritsen, H.C. (2012) Spectral phasor analysis allows rapid and reliable unmixing of fluorescence microscopy spectral images. *Opt. Express*, **20** (12), 12729–12741.

110. Malacrida, L., Jameson, D.M., and Gratton, E. (2017) A multidimensional phasor approach reveals LAURDAN photophysics in NIH-3T3 cell membranes. *Sci. Rep.*, **7** (1), 9215.

111. Malacrida, L., Astrada, S., Briva, A., Bollati-Fogolín, M., Gratton, E., and Bagatolli, L.A. (2016) Spectral phasor analysis of LAURDAN fluorescence in live A549 lung cells to study the hydration and time evolution of intracellular lamellar body-like structures. *Biochim. Biophys. Acta*, **1858** (11), 2625–2635.

112. Radaelli, F., D'Alfonso, L., Collini, M., Mingozzi, F., Marongiu, L., Granucci, F., Zanoni, I., Chirico, G., and Sironi, L. (2017) μMAPPS: a novel phasor approach to second harmonic analysis for in vitro-in vivo investigation of collagen microstructure. *Sci. Rep.*, **7** (1), 17468.

113. Peres, C., D'Autilia, F., Lanzanò, L., Bianchini, P., and Diaspro, A. (2014)

Polarization-Resolved SHG towards Collagen Imaging. *Biophys. J.*, **106** (2), 204a.

114. Annibale, P., and Gratton, E. (2014) Advanced fluorescence microscopy methods for the real-time study of transcription and chromatin dynamics. *Transcription*, **5** (2), e28425.

115. Ranjit, S., Lanzano, L., and Gratton, E. (2014) Mapping diffusion in a living cell via the phasor approach. *Biophys. J.*, **107** (12), 2775–2785.

116. Scipioni, L., Gratton, E., Diaspro, A., and Lanzanò, L. (2016) Phasor Analysis of Local ICS Detects Heterogeneity in Size and Number of Intracellular Vesicles. *Biophys. J.*, **111** (3), 619–629.

117. Scipioni, L., Bona, M. Di, Vicidomini, G., and Lanzanò, L. (2018) Local raster image correlation spectroscopy generates high-resolution intracellular diffusion maps. *Commun. Biol.*, **1**, 1–10.

118. Diaspro, A. (2019) Nanoscopy and Multidimensional Optical Fluorescence Microscopy. *Chapman and Hall/CRC*.

119. Tortarolo, G., Sun, Y., Teng, K.W., Ishitsuka, Y., Lanzanó, L., Selvin, P.R., Barbieri, B., Diaspro, A., and Vicidomini, G. (2019) Photon-separation to enhance the spatial resolution of pulsed STED microscopy. *Nanoscale*, **11** (4), 1754–1761.

120. Sarmento, M.J., Oneto, M., Pelicci, S., Pesce, L., Scipioni, L., Faretta, M., Furia, L., Dellino, G.I., Pelicci, P.G., Bianchini, P., Diaspro, A., and Lanzanò, L. (2018) Exploiting the tunability of stimulated emission depletion microscopy for super-resolution imaging of nuclear structures. *Nat. Commun.*, **9** (1), 3415.

121. Bunt, G., and Wouters, F.S. (2017) FRET from single to multiplexed signaling events. *Biophys Rev*, **9**, 119–129.

122. Spagnol, S.T., and Dahl, K.N. (2016) Spatially resolved quantification of chromatin condensation through differential local rheology in cell nuclei fluorescence lifetime imaging. *PLoS One*, **11** (1), 1–19.

123. Banerjee, B., Bhattacharya, D., and Shivashankar, G. V (2006) Chromatin Structure Exhibits Spatio-Temporal Heterogeneity within the Cell Nucleus. *Biophys. J.*, **91** (6), 2297–2303.

124. Abdollahi, E., Taucher-Scholz, G., and Jakob, B. (2018) Application of Fluorescence Lifetime Imaging Microscopy of DNA Binding Dyes to Assess Radiation-Induced Chromatin Compaction Changes. *Int. J. Mol. Sci.* , **19** (8).

125. Estandarte, A.K., Botchway, S., Lynch, C., Yusuf, M., and Robinson, I. (2016) The use of DAPI fluorescence lifetime imaging for investigating chromatin condensation in human chromosomes. *Sci. Rep.*, **6**, 31417.

126. Llères, D., James, J., Swift, S., Norman, D.G., and Lamond, A.I. (2009) Quantitative analysis of chromatin compaction in living cells using FLIM-FRET. *J. Cell Biol.*, **187** (4), 481–96.

127. Llères, D., Bailly, A.P., Perrin, A., Norman, D.G., Xirodimas, D.P., and Feil, R.

(2017) Quantitative FLIM-FRET Microscopy to Monitor Nanoscale Chromatin Compaction In Vivo Reveals Structural Roles of Condensin Complexes. *Cell Rep.*, **18** (7), 1791–1803.

128. Lou, J., Scipioni, L., Wright, B.K., Bartolec, T.K., Zhang, J., Masamsetti, V.P., Gaus, K., Gratton, E., Cesare, A.J., and Hinde, E. (2019) Phasor histone FLIM-FRET microscopy quantifies spatiotemporal rearrangement of chromatin architecture during the DNA damage response. *Proc. Natl. Acad. Sci.*, **116** (15), 7323 LP – 7332.

129. Fábián, Á.I., Rente, T., SzölloSi, J., Matyus, L., and Jenei, A. (2010) Strength in Numbers: Effects of Acceptor Abundance on FRET Efficiency. *ChemPhysChem*, **11** (17), 3713–3721.

130. Nazarov, P. V, Koehorst, R.B.M., Vos, W.L., Apanasovich, V. V, and Hemminga, M.A. (2006) FRET Study of Membrane Proteins : Simulation-Based Fitting for Analysis of Membrane Protein Embedment and Association. *Biophys. J.*, **91** (2), 454–466.

131. Koushik, S. V, Blank, P.S., and Vogel, S.S. (2009) Anomalous Surplus Energy Transfer Observed with Multiple FRET Acceptors. *PLoS One*, **4** (11), 1–12.

132. Berney, C., and Danuser, G. (2003) FRET or No FRET : A Quantitative Comparison. *Biophys. J.*, **84** (6), 3992–4010.

133. Zeug, A., Woehler, A., Neher, E., and Ponimaskin, E.G. (2012) Quantitative Intensity-Based FRET Approaches — A Comparative Snapshot. *Biophys. J.*, **103** (9), 1821–1827.

134. Van Zandvoort, M.A.M.J., De Grauw, C.J., Gerritsen, H.C., Broers, J.L.V., Oude Egbrink, M.G.A., Ramaekers, F.C.S., and Slaaf, D.W. (2002) Discrimination of DNA and RNA in cells by a vital fluorescent probe: Lifetime imaging of SYTO13 in healthy and apoptotic cells. *Cytometry*, **47** (4), 226–235.

135. Broussard, J.A., Rappaz, B., Webb, D.J., and Brown, C.M. (2013) Fluorescence resonance energy transfer microscopy as demonstrated by measuring the activation of the serine/threonine kinase Akt. *Nat. Protoc.*, **8** (2), 265–281.

136. Albiez, H., Cremer, M., Tiberi, C., Vecchio, L., Schermelleh, L., Dittrich, S., Küpper, K., Joffe, B., Thormeyer, T., Von Hase, J., Yang, S., Rohr, K., Leonhardt, H., Solovei, I., Cremer, C., Fakan, S., and Cremer, T. (2006) Chromatin domains and the interchromatin compartment form structurally defined and functionally interacting nuclear networks. *Chromosom. Res.*, **14** (7), 707–733.

137. Esposito, A., Gerritsen, H.C., and Wouters, F.S. (2005) Fluorescence Lifetime Heterogeneity Resolution in the Frequency Domain by Lifetime Moments Analysis. *Biophys. J.*, **89** (6), 4286–4299.

138. Schindelin, J., Arganda-Carreras, I., Frise, E., Kaynig, V., Longair, M., Pietzsch, T., Preibisch, S., Rueden, C., Saalfeld, S., Schmid, B., Tinevez, J.-Y., White, D.J., Hartenstein, V., Eliceiri, K., Tomancak, P., and Cardona, A. (2012) Fiji: an open-source platform for biological-image analysis. *Nat.*

Methods, **9**, 676.

139. Vámosi, G., Baudendistel, N., von der Lieth, C.-W., Szalóki, N., Mocsár, G., Müller, G., Brázda, P., Waldeck, W., Damjanovich, S., Langowski, J., and Tóth, K. (2008) Conformation of the c-Fos/c-Jun complex in vivo: a combined FRET, FCCS, and MD-modeling study. *Biophys. J.*, **94** (7), 2859–2868.

140. Mascetti, G., Vergani, L., Diaspro, A., Carrara, S., Radicchi, G., and Nicolini, C. (1996) Effect of fixatives on calf thymocytes chromatin as analyzed by 3D high-resolution fluorescence microscopy. *Cytometry*, **23** (2), 110–119.

141. Kruhlak, M.J., Celeste, A., Dellaire, G., Fernandez-capetillo, O., Müller, W.G., Mcnally, J.G., Bazett-jones, D.P., and Nussenzweig, A. (2006) Changes in chromatin structure and mobility in living cells at sites of DNA double-strand breaks. *J. Cell Biol.*, **172** (6), 823–834.

142. Burgess, R.C., Burman, B., Kruhlak, M.J., Misteli, T., Burgess, R.C., Burman, B., Kruhlak, M.J., and Misteli, T. (2014) Activation of DNA Damage Response Signaling by Condensed Chromatin Article Activation of DNA Damage Response Signaling by Condensed Chromatin. *CellReports*, **9** (5), 1703–1717.

143. Dinant, C., Jager, M. De, Essers, J., Cappellen, W.A. Van, Kanaar, R., Houtsmuller, A.B., and Vermeulen, W. (2007) Activation of multiple DNA repair pathways by sub- nuclear damage induction methods. *J. Cell Sci.*, **120**, 2731–2740.

144. Schermelleh, L., Carlton, P.M., Haase, S., Shao, L., Kner, P., Burke, B., Cardoso, M.C., Agard, D.A., Mats, G.L., Leonhardt, H., and Sedat, J.W. (2010) Subdiffraction Multicolor Imaging of the Nuclear Periphery with 3D Structured Illumination Microscopy. *Science (80-.).*, **320** (5881), 1332–1336.

145. Barboro, P., Ferrari, N., Capaia, M., Petretto, A., Salvi, S., Boccardo, S., and Balbi, C. (2015) Expression of nuclear matrix proteins binding matrix attachment regions in prostate cancer. PARP-1: New player in tumor progression. *Int. J. Cancer*, **137** (7), 1574–1586.

146. Martin, R.M., Leonhardt, H., and Cardoso, M.C. (2005) DNA Labeling in Living Cells. *Cytometry*, **67A** (1), 45–52.

147. Diaspro, A., Chirico, G., and Collini, M. (2005) Two-photon fluorescence excitation and related techniques in biological microscopy. *Q. Rev. Biophys.*, **38** (2), 97–166.

148. Fang, K., Chen, X., Li, X., Shen, Y., Sun, J., Czajkowsky, D.M., and Shao, Z. (2018) Super-resolution Imaging of Individual Human Subchromosomal Regions in Situ Reveals Nanoscopic Building Blocks of Higher-Order Structure. *ACS Nano*, **12** (5), 4909–4918.

149. Renz, M., Daniels, B.R., Vámosi, G., Arias, I.M., and Lippincott-schwartz, J. (2012) Plasticity of the asialoglycoprotein receptor deciphered by ensemble FRET imaging and single-molecule counting PALM imaging. *Proc. Natl. Acad. Sci.*, 1–9.

150. Dechat, T., Adam, S.A., Taimen, P., Shimi, T., and Goldman, R.D. (2010)

Nuclear lamins. *Cold Spring Harb. Perspect. Biol.*, **2** (11), a000547–a000547.

151. Shevelyov, Y.Y., and Ulianov, S. V (2019) The Nuclear Lamina as an Organizer of Chromosome Architecture. *Cells*, **8** (2), 136.

152. Bronshtein, I., Kepten, E., Kanter, I., Berezin, S., Lindner, M., Redwood, A.B., Mai, S., Gonzalo, S., Foisner, R., Shav-Tal, Y., and Garini, Y. (2015) Loss of lamin A function increases chromatin dynamics in the nuclear interior. *Nat. Commun.*, **6**, 8044.

153. Pelicci, S., Diaspro, A., and Lanzanò, L. Chromatin nanoscale compaction in live cells visualized by acceptor-to-donor ratio corrected Förster resonance energy transfer between DNA dyes. *J. Biophotonics*, **0** (0), e201900164.

154. Tortarolo, G., Sun, Y., Teng, W., Ishitsuka, Y., and Vicidomini, G. (2019) Nanoscale Photon-separation to enhance the spatial resolution of pulsed STED microscopy. *Nanoscale*, **11**, 1754–1761.

155. Vicidomini, G., Schönle, A., Ta, H., Han, K.Y., Moneron, G., Eggeling, C., and Hell, S.W. (2013) STED Nanoscopy with Time-Gated Detection: Theoretical and Experimental Aspects. *PLoS One*, **8** (1), e54421.

156. Sarmento, M.J., Oneto, M., Pelicci, S., Pesce, L., Scipioni, L., Faretta, M., Furia, L., Dellino, G.I., Pelicci, P.G., Bianchini, P., Diaspro, A., and Lanzanò, L. (2018) Exploiting the tunability of stimulated emission depletion microscopy for super-resolution imaging of nuclear structures. *Nat. Commun.*, **9** (3415), 1–11.

157. Harke, B., Keller, J., Ullal, C.K., Westphal, V., Schönle, A., and Hell, S.W. (2008) Resolution scaling in STED microscopy. *Opt. Express*, **16** (6), 4154–4162.

158. Tortarolo, G., Castello, M., Diaspro, A., Koho, S., and Vicidomini, G. (2018) Evaluating image resolution in stimulated emission depletion microscopy. *Optica*, **5** (1), 32–35.

159. Oneto, M., Scipioni, L., Sarmento, M.J., Cainero, I., Pelicci, S., Furia, L., Pelicci, P.G., Dellino, G.I., Bianchini, P., Faretta, M., Gratton, E., Diaspro, A., and Lanzanò, L. (2019) Nanoscale Distribution of Nuclear Sites by Super-Resolved Image Cross-Correlation Spectroscopy. *Biophys. J,* **117** (11), 2054-2065.

Publications

- Pelicci, S., Tortarolo, G., Vicidomini, G., Diaspro, A., Lanzanò, L. (2020). "Improving SPLIT-STED super-resolution imaging with tunable depletion and excitation power". *Accepted on Journal of Physics D: Applied Physics.*

- Pelicci, S., Diaspro, A., & Lanzanò, L. (2019). "Chromatin nanoscale compaction in live cells visualized by acceptor-to-donor ratio corrected Förster resonance energy transfer between DNA dyes". *Journal of Biophotonics*, (July), 1–13.

- Oneto, M., Scipioni, L., Sarmento, M. J., Cainero, I., Pelicci, S., Furia, L., Pelicci, P.G., Dellino, G.I., Bianchini, P., Faretta, M., Gratton, E., Diaspro, A., Lanzanò, L. (2019). "Nanoscale Distribution of Nuclear Sites by Super-Resolved Image Cross-Correlation Spectroscopy". *Biophysical Journal,* 117, 1-12.

- Castello, M., Tortarolo, G., Buttafava, M., Deguchi, T., Villa, F., Koho, S., Pesce, L., Oneto, M., Pelicci, S., Lanzanò, L., Bianchini, P., Sheppard, C.J.R., Diaspro, A., Tosi, A., Vicidomini, G. (2019). "A robust and versatile platform for image scanning microscopy enabling super-resolution FLIM". *Nature Methods*, 16(2), 175–178.

- Sarmento, M. J., Oneto, M., Pelicci, S., Pesce, L., Scipioni, L., Faretta, M., Furia, L., Dellino, G.I., Pelicci P.G., Bianchini, P., Diaspro, A., Lanzanò, L. (2018). "Exploiting the tunability of stimulated emission depletion microscopy for super-resolution imaging of nuclear structures". *Nature Communications*, 9(3415), 1–11.

ORAL PRESENTATIONS

- Pelicci, S., Oneto, M., Di Bona, M., Cainero, I., Barboro, P., Diaspro, A., & Lanzano′, L. (2019). "Chromatin Nanoscale Organization Investigated by FLIM-FRET and STED Superresolution Microscopy". Biophysical Society 63th Annual Meeting, Baltimore, Maryland, March 02-06, 2019

POSTER

- Pelicci, S., Oneto, M., Di Bona, M., Diaspro, A., & Lanzanò, L. (2018). "FLIM-FRET of Chromatin in Live Cells using Two DNA-Binding Dyes". Biophysical Society 62th Annual Meeting, San Francisco, California, February 17-21, 2018.